The statistics of travelling eddy variability in the South China Sea and its external forcing

Dissertation with the aim of achieving a doctoral degree

at the Faculty of Mathematics, Informatics and Natural Sciences

Department of Earth Sciences at Universität Hamburg

Submitted by Meng Zhang

from Hubei China

Hamburg, 2019

Accepted as Dissertation at the Department of Earth Sciences

Day of oral defense: 07.05.2019

Reviewers: Prof. Dr. Hans von Storch

Prof. Dr. Corinna Schrum

Chair of the Subject Doctoral Committee: Prof. Dr. Dirk Gajewski

Dean of Faculty of MIN: Prof. Dr. Heinrich Graener

Abstract

Ocean eddy plays a vital role in the ocean mixing and the ocean transport of energy, momentum and materials, which changes local water properties of temperature, salinity and productivity. They affect the ocean circulation and marine ecosystem deeply. Ocean eddies are very active in the South China Sea (SCS). However, the variability across decades of years of migrating eddy activities in the SCS have not yet been documented. No research is found to work on the projection of the future eddy activities in the SCS either. From the perspective of doing projection with statistical downscaling methodology, which will be needed for building models for projecting climate change scenarios, this thesis provides statistics of travelling eddies in the SCS in the past decades, and investigates the effects of the external forcing on the variability of eddy activities.

In order to overcome the problem about a lack of observations with decadal time period and high resolution which could describe eddy activities, I employ an eddy-resolving ocean simulation, named “STORM”, which was forced by the NCEP1 reanalysis data and covers 1950-2010. Firstly, I examine the performance of the STORM simulation in reproducing the hydrodynamics in the SCS, by taking the AVISO altimeter observation and the C-GLORS ocean reanalysis data set as reference data. The STORM simulation shows great similarity to the reference data, in terms of the distribution and the variability at seasonal and inter-annual time scales of sea surface height anomaly (SSHA) and sea surface current. For sea surface temperature (SST), STORM could even show more details of the upwelling off the Vietnam coast. The validation proves the ability of the STORM simulation in describing the hydrodynamics in the SCS.

Given that the popular eddy detection and tracking algorithms “winding angle method” and “W-based method” have error problem related to the differential or integral computation, I develop one new algorithm which only relies on the discrete SSHA fields. As observed,

anticyclonic eddies are mostly warm, and cyclonic eddies are mostly cold. The further comparison with AVISO in the detected eddy distribution demonstrates that STORM well reproduces the eddy activities. In addition, AVISO produces too many extremum related to noise before filtering potential eddies. And after the filtering, AVISO underestimates eddy activities, which Amores et al. (2018) suggested is caused by its limited resolution.

Based on this algorithm, I derive 1709 anti-cyclonic eddy (AE) tracks (28.0 per year) and 3331 cyclonic eddy (CE) tracks (54.6 per year) with travel length over 100 km from the STORM simulation from 1950-2010. The climatological features and the spatial and temporal variability of eddy number (EN), eddy diameter (ED) and eddy intensity (EI) are investigated. The eddy properties reveal significant inter-annual variability and seasonal difference, but weak decadal variability. The long-term variability is hardly correlated with El Niño. ED correlates well with EI at both seasonal scale and inter-annual scale. Eddies most frequently occur in the Luzon Strait and along the western boundary currents. The annual spatial distributions of the eddy properties do not reveal a dominant EOF pattern in the 0.1-degree resolution, just white eigenvalue spectra. Only when binning the distribution into 1-degree or 2-degree grids, some meaningful structure shows up.

Because of the failure to detect leading patterns in the spatial distribution of eddy properties, I take the vector consisting of six area-mean eddy parameters - : the EI of the peak points (I), the ED of the peak points (D), the EN of the peak points (N), the travel distance of the eddy track (L), the eddy lifetime (T) and the percentage of intense eddy points (%I). Most external drivers affect the eddy activities indirectly and pass its effect on the eddy activities through the background flow, like wind stress and Kuroshio. Furthermore, the instability of the background flow provides the primary energy source for eddy formation and eddy growth, by inducing the energy conversion from available potential energy to kinetic energy. This thesis uses the canonical correlation analysis (CCA) to investigate the effect of the external forcing on the eddy parameters in summer. In the CCA, three components of the instability are considered as large-scale drivers, i.e. barotropic instability, current shear and temperature stratification. The CCA results exhibit up to 39% variability of eddy activities in the SCS could be traced by the background flow.

The limited impact of the large-scale background flows, the white noise in the spatial distribution of eddy properties, and weak correlation with El Niño, point to a massive presence of internal variability (which is opposed to variability provoked by large-scale drivers). I suggest that to a large extent, the variability of eddy activity may be governed by its internal variability.

Zusammenfassung

Ozeanwirbel sind wesentlich für Mischung und Transport von Energie, Impuls und Substanzen im Ozean, mit Auswirkungen auf die Temperatur, die Salinität und Produktivität. Als solche haben sie eine erhebliche Wirkung für die Ozeanzirkulation und für das marine Ökosystem.

Solche Wirbel sind sehr aktiv im Südchinesischen Meer (SCS). Allerdings ist über die dekadische Variabilität von wandernden Wirbeln im SCS wenig bekannt. Dies gilt auch für Erwartungen für zukünftige Zustände. In meiner Arbeit werden Statistiken von wandernden Wirbeln im SCS in den letzten sechs Dekaden abgeleitet, und deren Konditionierung durch externe Antriebe. Solche Daten werden auch benötigt zur Konstruktion von empirischen Downscaling-Modellen, für Projektionen zukünftig möglicher Änderungen.

Für den Zeitraum der letzten Jahrzehnte gibt es nicht ausreichend Beobachtungen, um Wirbelstatistiken abzuleiten. Daher wird die Simulation „STORM“ mit einem Eddy-auflösenden Ozeanmodell ausgewertet. Das Modell wurde mit zeitlich variablen atmosphärischen Analysen von NCEP angetrieben, und über den Zeitraum 1950-2010 integriert.

Im ersten Abschnitt wird diese STORM Simulation verglichen mit den AVISO-Altimeter-Daten und mit den ozeanischen Reanalysen C-GLORS. Dieser Vergleich ist für STORM positiv, was die Verteilung und Variabilität auf saisonalen und interannualen Zeitskalen von Anomalien der Meeresoberflächenhöhe (SSHA) und Oberflächenströmungen angeht. Für die Meeresoberflächentemperatur (SST) zeigt STORM zusätzliche Strukturen längs der Vietnamesischen Küste. Offenbar beschreibt STORM die Hydrodynamik im SCS realistisch.

Die häufig verwendeten Algorithmen zur Identifikation und zum Verfolgen von Wirbeln namens „winding angle“ und „W-based“ Methode haben manchmal Probleme wegen der erforderlichen Integral- bzw. Differentialoperationen. Daher wurde ein neuer Algorithmus entwickelt, der nur das diskrete SSHA-Feld verwendet. Wie beobachtet, zeigen antizyklonale Wirbel meist warme Kerne, und zyklonale überwiegend kalte Kerne. Ein Vergleich mit AVISO zeigt eine gute Übereinstimmung mit den in STORM gefundenen Verteilungen von Wirbeln. Es wurde auch gefunden, dass in AVISO zu viele extreme SSHA Werte gefunden werden, wenn keine geeignete Filterung zur Unterdrückung des Noise implementiert wird. Mit so einer Filterung finden sich weniger in AVISO, was Amores et al. (2018) auf die begrenzte räumliche Auflösung der AVISO Felder zurückführen.

Mit dem neuen Algorithmus wurden in der 1950-2019 STORM Simulation 1709 antizyklonale (AE) Wirbel-Zugbahnen (mit Längen von mehr als 100 km) gefunden (28,0 pro Jahr) und 3331 zyklonale Wirbel (CE; 54.6 pro Jahr). Klimatologische Maßzahlen sowie die räumliche und zeitliche Variabilität der Anzahl der Wirbel (EN), der Durchmesser (ED) und der Intensitäten (EI) wurden bestimmt. Auf der saisonalen und den interannualen Zeitskalen gibt es erhebliche Variabilität, aber die dekadische Variabilität ist schwach. Die niederfrequente Variabilität ist kaum korreliert mit dem El Nino-Phänomen. ED ist mit EI korreliert, sowohl auf der saisonalen als auch auf der interannualen Zeitskala. Räumlich gibt es die meisten Wirbel in der Luzon-Straße und in der Strömung längs des westlichen Randes des SCS. Die jährlichen Statistiken der Wirbeleigenschaften zeigen nur entartete Empirische Orthogonalfunktionen, wenn die Analyse of dem Grad-Gitter von STORM durchgeführt wird. Erste wenn die Daten zusammengefasst werden auf Gittern mit 2 Grad Auflösung, zeigen sich sinnvolle Strukturen.

Wegen dieser fehlenden dominanten räumlichen Muster, wird im Folgenden nur mit Gebietsmitteln von Wirbeleigenschaften gearbeitet, nämlich EI von maximalen Wirbelzentren (längs einer Zugbahn; I), ebenso ED von maximalen Wirbelzentren (D), Anzahl maximaler Wirbelzentren (N), Zugbahnlängen (L), zeitlicher Länge einer Zugbahn (T) und der Anzahl „intensiver“ Wirbelpunkte (%I). Externe Antriebe, wie das Windsystem oder der Kuroshio-Strom, wirken auf die Wirbelbildung und Ausbreitung nur indirekt durch eine Einwirkung auf das Strömungssystem. Die Instabilität dieser Strömungssysteme macht die erforderliche Energie für die Bildung von Wirbeln verfügbar, indem verfügbare potentielle Energie in kinetische Energie umgewandelt wird.

In dieser Arbeit wird die Kanonische Korrelationsanalyse (CCA) benutzt, um die Wirkung veränderlicher Strömungssysteme auf die oben angegebenen Wirbelparameter zu beschreiben. Dabei wird nur der Sommer analysiert, also die Jahreszeit mit dem Südwestmonsoon. Drei mögliche Instabilitätsmechanismen werden untersucht, die barotrope Instabilität, die Strömungsscherung, sowie die thermische Schichtung. Den Ergebnissen der CCA zufolge, können bis zu fast 40% der Variabilität auf diese Instabilitäten zurückgeführt werden.

Der begrenzte Einfluss der Variationen der Strömungssysteme, das „weiße Rauschen“ in der räumlichen Verteilung der Wirbeleigenschaften und die schwache Korrelation mit dem El Nino Phänomen weisen auf eine starke Präsenz interner Variabilität hin (also Variabilität, die nicht auf großskalige Antriebe zurückgeführt werden kann). Wir vermuten, dass die Variabilität der Wirbelaktivität auf diese interne Variabilität zurückzuführen ist.

Contents

1. Introduction

Ocean eddies with swirling water that travel long distances are common in the global oceans (Figure 1.1) and have diameters ranging from tens to hundreds kilometers. Currently, the instability of the background flows is supposed to be the major generation mechanism of ocean eddies (Ferrari and Wunsch, 2009) because of its impact on energy conversion, which provides energy for the formation and growth of ocean eddies. The velocities within eddies are up to several meters per second, and their propagation speeds are comparable to the phase speed of long baroclinic Rossby waves (Faghmous et al., 2015).

Analogous to synoptic storm phenomena, ocean eddies can be classified into anticyclonic eddies (AEs) and cyclonic eddies (CEs) based on the water rotation direction. In most cases, AEs (CEs) have warm (cold) cores, with lowered (uplifted) thermoclines and downwelling (upwelling) flows, which transport heat and ocean material vertically. The rich nutrients lifted by eddy-induced upwelling contribute extensively to marine productivity (Lee et al., 1991; Mahadevan, 2014). Along with the propagation of ocean eddies, water parcels trapped within eddy cores can travel long horizontal distances (Figure 1.2); this causes an exchange of the water properties with those of the local water, so ocean eddies contribute greatly to the transport of ocean matter, momentum and energy, and they play important roles in ocean circulation and the ocean ecosystem. Strong eddies can even damage oil platforms, so they can pose large risks to human activities.

Projecting the future intensity, frequency, sizes and spatial distributions of eddy activity is important to both oceanographic science and human safety. However, current climate models are too coarse to project eddies in the future. The “statistical downscaling” methodology can help to achieve this goal. Following the procedures shown in Figure 1.3 (von Storch, 1995), a statistical downscaling model relating the regional climate parameters (i.e., the regional eddy activity) to large-scale drivers is constructed. The large-scale drivers can be described well by the coarse output from the climate model, so the future eddy activity is projected by applying the constructed downscaling model in the future. This technique has been successful in meteorology (Benestad et al., 2008; H. von Storch et al., 1993) and has also been applied to the local sea level (Cui et al., 1995; H. von Storch and Reichardt, 1997).

The characteristics of eddies have been studied by combining many kinds of observations, including altimeter observations, Argo floats (Chen et al., 2011), and a multi-month field campaign (Z. W. Zhang et al., 2016). To build a statistical model, knowledge of the long-term features of the eddy activity, including not only the eddies but also the climatology and the variability in eddy activity, is necessary.

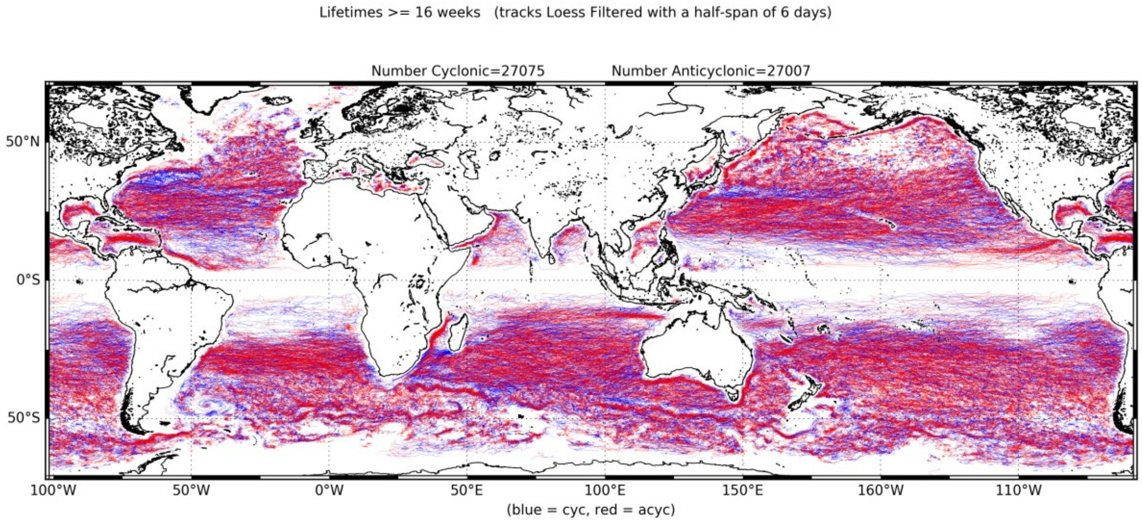

Figure 1. 1 Tracks of eddies with lifetimes greater than 16 weeks from 1993 to 2018 based on AVISO observations. (Figure source https://www.aviso.altimetry.fr/fileadmin/documents/data/products/value-added/aviso_validation_report_eddy_tracking_2.0exp.pdf)

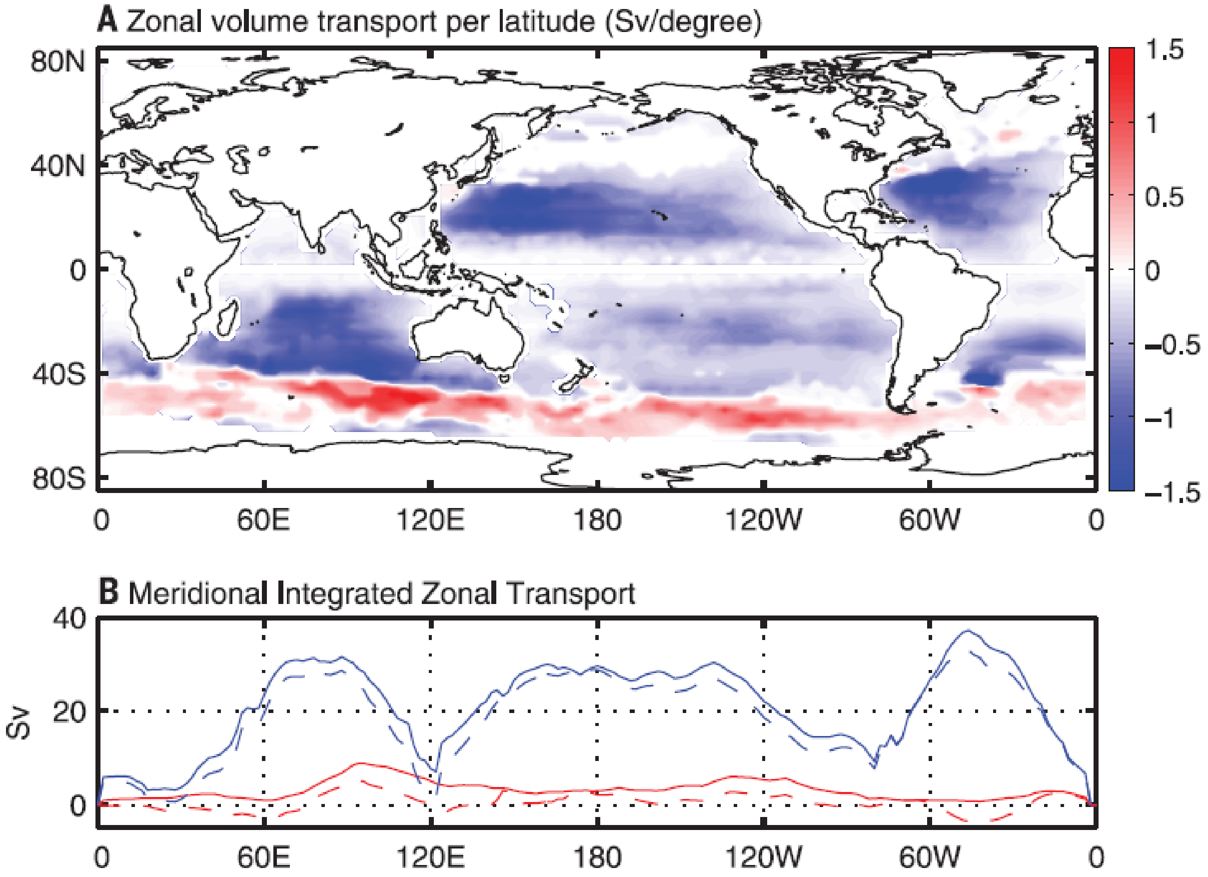

Figure 1. 2 The global spatial distribution (a) and the meridionally integrated distribution (b) of the zonal eddy-induced fluid transport. (Z. G. Zhang et al., 2014).

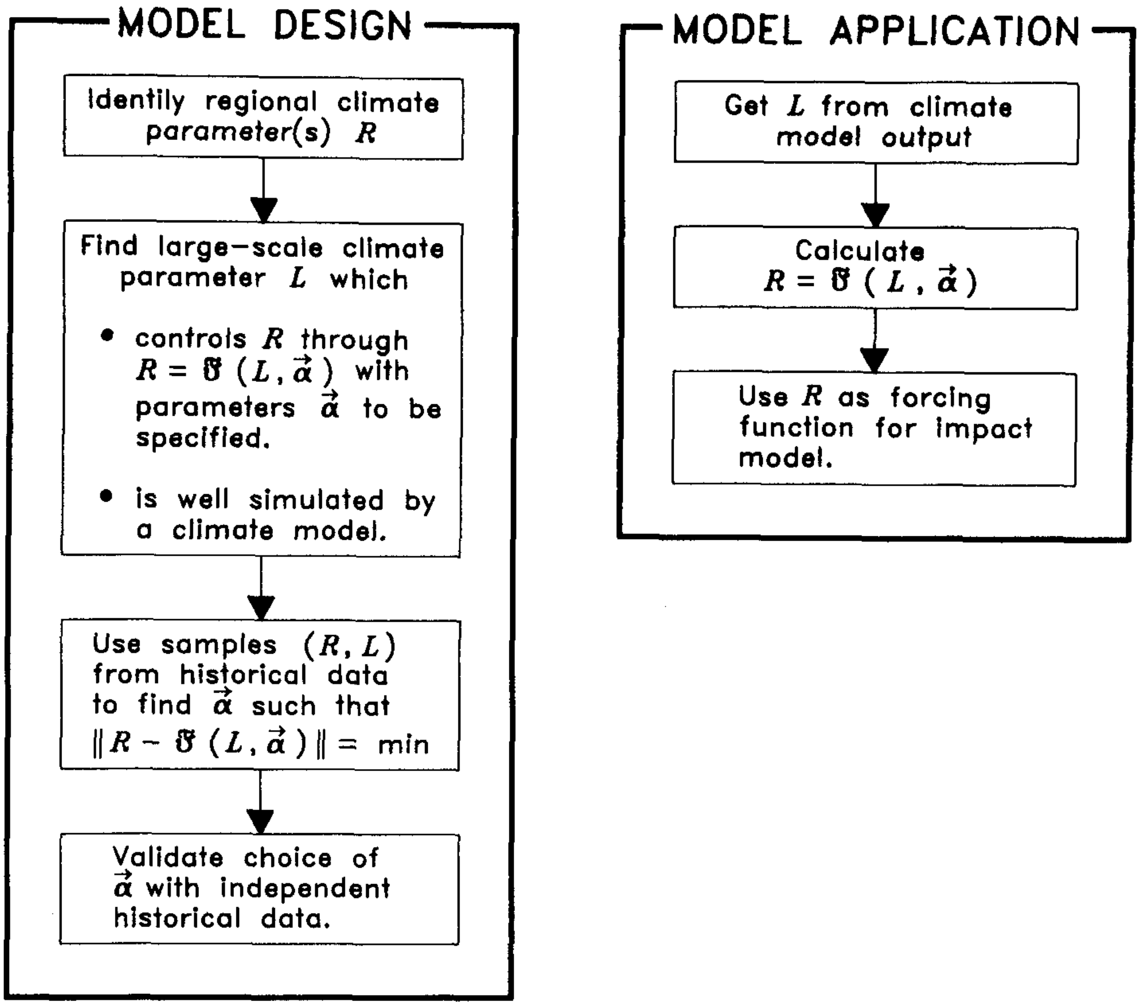

Figure 1. 3. Concept of statistical downscaling. (von Storch, 1995)

1.1 The eddies in the South China Sea

The South China Sea (SCS) is the largest marginal sea in the northwest Pacific and has an average depth of more than 2000 m. Every year, a large number of oceanic eddies occur in the SCS. Because of their vital roles in ocean circulation and in the marine ecosystem, oceanic eddies in the SCS have drawn a large amount of attention from oceanographers and ecologists.

The upper layer ocean circulation in the SCS is mainly dominated by the monsoon and has a strong western boundary current and a large gyre. The boundary current, along with the gyre, reverses its direction during the summer monsoon and winter monsoon. In the northern SCS, one branch of the Kuroshio intrudes into the SCS through the Luzon Strait and results in exchanges of heat, salt and moment (Nan et al., 2015). A three-dimensional baroclinic circulation model of the SCS developed by Pohlmann (1987) first pointed out the possible existence of upwelling at the Vietnam coast.

G. Wang et al. (2003) summarized several generation mechanisms of eddies in different regions of the SCS by analyzing 86 mesoscale eddies derived from altimeter data from 1993-2001. To the southwest of Taiwan, frontal instability due to the Kuroshio is thought to be a factor in shedding eddies. In addition, the strong eastward current during the southwesterly monsoon has been found to generate eddies offshore of Vietnam, particularly a stationary pair of an anticyclonic eddy (AE) and a cyclonic eddy (CE). The vorticity from the Kuroshio front, the wind stress curl and the interaction of strong currents with the topography also influence the eddy generation mechanisms.

Many *case studies* of eddies in the SCS have demonstrated and revealed the details of these generation mechanisms. Most of the case studies focused on the entire lifetime of the eddies, including their formation, evolution, propagation, dissipation, and three-dimensional (3D) structure (Chu et al., 2014, 2017; Yuan et al., 2007; Q. Wang et al., 2015; Zu et al. 2013; Geng et al., 2016, 2017; Li et al., 2015). D. Wang et al. (2008) found that the relaxation of Ekman transport anomalies may have contributed to eddy shedding in two AEs in the northeastern SCS. Z. W. Zhang et al. (2016) captured the full-depth 3D structure of an AE and CE eddy pair near the Luzon Strait in 2013/2014 based on a multi-month field campaign called S-EEE (the SCS Mesoscale Eddy Experiment) and suggested that the dominant dissipation mechanism of the eddy pair may have been the generation of submesoscale motions. In the summer, an eddy dipole with one strong AE and one weak CE is always located near 11° N. The formation of this eddy pair is related to vorticity transport from the western boundary current, which is driven by the wind stress curl (Chu et al., 2017).

The detailed generation and dissipation mechanisms of eddies that form in different regions or at different times vary depending on the external forcing, including the wind curl, Kuroshio front, and current jet. However, all of these factors impact the eddy activity by changing the background flows. The kinetic energy converted from the available potential energy is essential for the formation and growth of eddies, and the conversion is induced by the instability of the background flows. Therefore, the instability of the background flow is the key large-scale driver.

1.2 The climatology of the eddies in the SCS

Recently, several statistical analyses of the variability in SCS eddies have been performed (G. Wang et al., 2003; Sun et al., 2016, Chen et al., 2011, 2012; Xiu et al., 2010; Li et al., 2011; Nan et al., 2011; Feng et al., 2017). Xiu et al. (2010) investigated the eddy activity in water deeper than 1000 m from 1993-2007 using both 7-day interval AVISO altimeter data and the output from a regional ocean model system (ROMS). The authors identified approximately 32.8 eddies each year from the AVISO data (of which 52% were cyclonic eddies) and found that the interannual variabilities in the number of eddies and the area covered by eddies are not correlated with El Niño events. Chen et al. (2011) focused on mesoscale eddies and identified 827 mesoscale eddies (approximately 48.6 per year) in the SCS during 1993-2009 from 7-day interval AVISO satellite data with different detection parameters. Their study found that more AEs occurred than CEs. However, using the same data set, Nan et al. (2011) detected many more CEs (41) than AEs (27) southwest of Taiwan.

Feng et al. (2017) used daily AVISO data to identify mesoscale eddies in the SCS from 1993 to 2007 and found more CEs than AEs. The number of detected eddies is sensitive to the region and the identification parameters. In the analysis of Chen et al. (2017), the eddy intensities over 17 years exhibited a weak negative correlation with the sea surface temperature anomalies in the central Pacific (given by the Nino3 index), but no correlation was found between the number of eddies and El Niño activity. However, Chu et al. (2017) found in a composite analysis that the El Nino–Southern Oscillation (ENSO) influences the stationary eddy pair off the Vietnam coast. This eddy pair is one of the most important phenomena off the Vietnam coast during the summer monsoon periods, but it was absent during the ENSO transition years. They suggested that the ENSO transition events led to changes in the southwesterly monsoon and then resulted in the eastward current jet turning northward and the eddy pair disappearing. Based on the output of an eddy-resolving ocean simulation for the Earth Simulator (OFES), Sun et al. (2016) investigated the interannual variability in the eddy kinetic energy (1980-2014) in the northeastern SCS and determined that the Luzon Strait transport exhibited a modulating effect, but their study did not consider the eddy activity.

Although several investigations of eddy activity in the SCS have been performed, such as the occurrence frequency distribution of eddies and its seasonal and interannual variabilities in the SCS, the statistics have been limited to relatively short time spans of no more than 20 years, beginning in 1993. In addition, most of the statistical analyses focused only on high-intensity mesoscale eddies due to the coarse data set.

An issue that has not been completely resolved is the extent to which the statistics of the formation and lifecycle of eddies may be affected by large-scale conditions, such as the seasonal mean barotropic or baroclinic state (or the atmospheric conditions, though they likely would not act directly but rather indirectly by changing the currents). The experiment by Tang et al. (2019) demonstrated that some if not most of the eddy activity reflects internal dynamic processes that are not caused by external factors.

The previous analyses of eddy activity, such as the number of eddies and the seasonal and interannual variabilities in the SCS, have suffered from several limitations. The limited accuracy of the satellite data used for the analyses has made it necessary to limit the analysis to high-intensity mesoscale eddies. In addition, only time scales of a few years could be considered because of the relatively short time span of the data (less than 20 years, beginning in 1993).

To assess the roles and impacts of eddies and project their future activity, the statistical characteristics and spatiotemporal variabilities of long-term oceanic eddy activity are needed. Decadal high-resolution outputs from global ocean simulations are candidates to solve this problem.

1.3 Research plan

Due to the scientific and social importance of eddy activity, I want to project the eddy activity in the SCS using the empirical statistical downscaling methodology. Because of the lack of such observations over long time periods with high spatial resolution, I use an eddy-resolving global ocean simulation called “STORM” that covers six decades. The data used in our work have several advantages, such as no observational errors and uninterrupted, homogeneous coverage over six decades. However, the data are the output of a model and may be affected by unknown shortcomings related to the limited spatial and temporal resolutions, the incompleteness of the physical processes, and the absence of exchanges of properties between the ocean and atmosphere. However, I have no indications that the STORM simulation is inconsistent with the limited observational data in the South China Sea; a systematic comparison of several large-scale features derived from satellite data and the simulation revealed no such inconsistencies (M. Zhang and von Storch, 2017), which is addressed in Chapter 3 of this thesis. The STORM simulation comes from the German consortium project STORM (J. von Storch et al., 2012), and its abilities have been demonstrated in climate research (Tim et al., 2015; Yi et al., 2017; Evadzi, 2017).

We note that our goal in this thesis is not to perform the downscaling or the projection but to develop a tool for doing so. The added value of our work is also to provide statistics of travelling eddies, which may be useful in other contexts. In general, this thesis attempts to address the following questions:

- The STORM simulation has been used to examine sea level variability along the Ghana coast and upwelling in the Arabian Sea. I would like to investigate whether the STORM simulation can reproduce the currents in the SCS and capture the statistics of ocean eddies in the SCS.
- Climatological research about the activity of travelling eddies in the SCS covers no more than 30 years. To develop empirical statistical downscaling models and then project future eddy activity, the climate features over much longer time periods are essential. Based on the validated STORM simulation, I would like to derive the climatology and variabilities at different time scales for the travelling eddy activity in the SCS over six decades (1950-2010) from the STORM simulation.
- To construct the empirical downscaling model, the large-scale external drivers that could control the eddy activity need to be identified. I attempt to search for such external drivers and determine the extent to which the eddy activity can be controlled by the external forcing and how much is due to its internal variability.

The thesis consists of six chapters, including this introductory chapter and a summary and outlook chapter at the end. Chapter 2 describes the data sets and the statistical method used in our work as well as our newly developed eddy detection and tracking algorithm. The popular eddy detection and tracking methods “winding angle method” and “W-based method” use differential or integral computations, which lead to inaccuracy in the discrete fields. I develop an algorithm that can directly derive eddies from the discrete sea surface height anomaly fields without any such computations. The detailed description and validation of the new algorithm are presented in Chapter 2 as well.

Chapters 3 through 5 are the three main parts of the thesis. Chapter 3 is our published paper about the assessment of the STORM simulation for reproducing the SCS dynamics. Satellite observations and ocean reanalysis data are employed to estimate the performance of STORM. The STORM simulation shows good similarity with the reference data in terms of the spatial distribution and the seasonal and interannual variabilities of the sea surface height and sea surface currents. STORM reveals more details about the upwelling along the Vietnam coast in the sea surface temperature fields due to its higher resolution. A case of the regional ocean downscaling model is used for further verification. The downscaling model specifies the statistics of the throughflow in the SCS by means of coarse wind fields.

Based on the STORM simulation and our new eddy detection and tracking algorithm, the 61-year statistics of the eddy activity in the SCS are investigated. First, I compare the spatial distributions of eddies from the STORM simulation and AVISO observations. The STORM results have a similar distribution to the AVISO data; however, the AVISO data contain large amounts of noise before filtering, so many more potential eddy points appear. These points disappear after filtering; subsequently, fewer eddy points remain compared to the STORM results. Therefore, I analyze the climatology of the travelling eddy activity over 1950-2010, including the spatial distribution of the number of eddies and the probability distribution functions of the eddy diameter and eddy intensity. An empirical orthogonal function analysis of the annual distribution of eddy properties shows no dominant patterns in a 0.1-degree grid. When binned into larger grid boxes, the annual distribution has some structure. The time series of the number of eddies, eddy diameter and eddy intensity reveal large seasonal differences and significant interannual variabilities but weak decadal variability and no trend. The variability weakly correlates with El Niño. The eddy intensity covaries at both seasonal and interannual scales.

Because the background flow in the SCS is the link between the large-scale external drivers and the eddy activity, its relationship with the local eddy activity is analyzed. Barotropic instability and baroclinic instability provide the primary kinetic energy for eddy formation and growth by causing the conversion of energy from the available potential energy. I use the barotropic mass stream function, current shear and potential stratification as measurements of these instabilities in the SCS flows. A canonical correlation analysis shows that up to 38.6% of the variance in the eddy activity can be determined by these measurements.

2. Data and methods

This thesis uses four data sets, including an ocean simulation (STORM), an ocean reanalysis data set (C-GLORS), a satellite observation data set (AVISO) and a topographic data set (ETOPO1). A new eddy detection and tracking algorithm is developed to investigate the long-term eddy characteristics in the SCS. In addition, several statistical methods are employed to validate the ocean simulation and derive the major eddy features as well as their linkages with the ocean barotropic states. The data sets and the methods are described in detail in this chapter.

2.1 Data introduction

This study is based on a global eddy-resolving simulation from the German consortium project STORM. I refer to this simulation as “STORM” in the following reanalysis and in the description in Section 2.1.1. A satellite observation data set and an ocean reanalysis data set are employed to assess the quality of the STORM simulation, and they are introduced in sections 2.1.2 and 2.1.3, respectively. The ETOPO1 data provide topographic and bathymetric information for the eddy detection.

2.1.1 STORM simulation

STORM data set is the output of one simulation in the German consortium project STORM (J. von Storch et al., 2012; more information about this project is available in https://www.dkrz.de/redmine/projects/storm/wiki/STORM_list_of_experiments). It employed a state-of-the-art ocean model - the Max Planck Institute Ocean Model (MPI-OM). For ensuring an isotropic horizontal resolution, the bipolar grid of the model has been replaced by a tripolar grid in the model. The model was forced by the 6-hourly National

Centers for Environmental Prediction (NCEP)/National Center for Atmospheric Research (NCAR) reanalysis dataset (Kalnay et al. 1996), after 25-year spin-up phase using the German Ocean Model Intercomparison Project (OMIP) forcing. The kinetic energy reached a quasi-steady state in the deep ocean after the spin-up. In total, this simulation has 3600 × 2392 horizontal grid points and 80 uneven vertical levels, with covering a period of 1948 – 2014 and a 2.3-km resolution at the finest grid. The grid-resolution in the SCS domain is approximately 0.1° so that eddies are resolved (Hallberg, 2013). Both the daily and monthly versions have been archived in the German Climate Computing Center (DKRZ; https://www.dkrz.de/redmine/projects/storm). As the limitation of storage, daily STORM data only at several layers have been saved, but monthly data can provide variables at all 80 layers. Tidal forcing was not activated in this simulation. More detailed configurations and the parameterization schemes can be found in the papers of J. von Storch et al. (2012) and Jungclaus et al. (2006).

STORM performs well in the research on meso- or small-scale oceanic phenomena, including eddy-related heat and salt fluxes (J. von Storch et al., 2016), upwelling systems (Tim et al., 2015, Yi et al., 2017), and sea level along the Ghana coast (Evadzi, 2017).

STORM proves reliable in representing oceanic dynamics in the SCS by the author's paper (M. Zhang and von Storch, 2017). STORM agrees well with AVISO and C-GLORS (Storto et al., 2016) in the seasonal means and inter-annual variabilities of sea surface height anomaly (SSHA) in the SCS. The finer resolved STORM generates stronger currents and presents more details of the strong upwelling offshore the Vietnam coast during summertime. The assessment demonstrated the skill of STORM to capture the main features of the SCS oceanic hydrodynamics. The published paper will be shown in chapter 3. And further assessment about reproducing eddies in the SCS is presented in chapter 4.2.

After the validation, eddy activities in the SCS will be derived from STORM daily SSHA variable. And monthly barotropic mass stream function and monthly currents at different layers will be used to explore the large-scale factors that affect the eddy activity.

2.1.2 Satellite observation

The gridded daily SSALTO (SSALTO multi-mission ground segment)/Duacs (Data Unification and Altimeter Combination System) data set from the Archiving, Validation and Interpretation of Satellite Data in Oceanography (AVISO) (AVISO, 1996, 2015; https://www.aviso.altimetry.fr/en/home.html) is used for validating STORM simulation. I refer to this satellite product as AVSIO in the thesis. This product is derived from several satellite altimeter data, including ERS and ENVISAT (AVISO, 1996). This research uses the gridded SSHA from 'Delayed Time' and 'All-Sat merged' AVISO, which merged data from all altimeter missions available (up to four at a given time) (Faghmous et al., 2015). The data set provides SSHA fields with a grid resolution of 0.25 degree and time resolution of 1 day since 1993.

AVISO altimeter observation has been widely used in the study related to ocean circulation. And it is also the most common data set to characterize the ocean eddy statistics by means of an automatic eddy detection and tracking methodology (Amores et al., 2018; Chen et al., 2011; Xiu et al., 2010) This study takes AVISO data set as reference data to estimate the skill of STORM in reproducing the ocean dynamics and ocean eddy characteristics in the SCS.

It is worth noting the issue about the accuracy of the data set. The information provided by the AVISO handbook (Taburet et al., 2018) is not really conclusive, but I may expect the root mean square error to be above 1 cm, if not much larger. While the grid resolution is about 25 km, the effective resolution in describing phenomena is also expected to be larger, namely 65 km and possibly much more. The detailed discussion about the accuracy of AVISO altimeters is presented in section 4.2.

2.1.3 C-GLORS reanalysis

The Euro-Mediterranean Center for Climate Change (CMCC) produced a global ocean reanalysis data set, named the CMCC Global Ocean Research System (C-GLORS; Storto and Masina, 2014; Storto et al., 2016, Zhang and H. von Storch, 2017). Together with the AVISO observations, the version 4 of C-GLORS ocean reanalysis is used to assess STORM data set with regard to sea surface current (SSC) and sea surface temperature (SST) in the SCS. I first compare STORM with AVISO and C-GLORS. When sufficient similarity is shown, I may continue the verification of STORM by comparing with the derived C-GLORS data, which cover more variables than AVISO.

C-GLORS has employed the NEMO ocean general circulation model (Madec et al., 1998), with one polar on the South pole and two on the Asian and North-American continents (Madec and Imbard, 1996), forced by ERA-Interim atmospheric reanalysis data (Dee et al., 2011) from the European Centre for Medium-Range Weather Forecast (ECMWF). This model has 50 levels in vertical direction and a horizontal resolution of 0.25 degree. C-GLORS has assimilated observations of temperature and salinity from Argo floats, moorings, Conductivity-Temperature-Depth (CTDs) and Expandable Bathy Termographs (XBTs), as well as the AVISO SSHA data by implementing a three-dimensional variational analysis system (3DVAR). The monthly C-GLORS from 1982 to 2013 are available in http://www.cmcc.it/c-glors/. Storto et al. (2016) stated the detailed configuration of the reanalysis system and carried out an extensive validation. Their results indicate C-GLORS simulates the reliable states of mean surface circulation and transport, and seal level variability.

2.1.4 ETOPO1 topography and bathymetry data

The ETOPO1 Global Relief Model (Amante and Eakins, 2009; available in https://www.ngdc.noaa.gov/mgg/global/global.html) is an improved version to the ETOPO2 Global Relief Model, which was developed by the National Geophysical Data Center (NGDC) in the National Oceanic and Atmospheric Administration (NOAA). It was produced after evaluating, editing and merging diverse digital data sets. ETOPO1 can provide global topography, bathymetry and coastline in 1 arc-minute cell size. Its bathymetry information comes from four centers, i.e. NGDC, the Japan Oceanographic Data Center (JODC), the Mediterranean Science Commission (CIESM) and the Caspian Environment Programme (CEP). This work used the bathymetry of ETOPO1 in the SCS to filter oceanic eddies in the shallow water (depths <= 200m). The 200-m isobath in the SCS is plotted in figure 2.1.

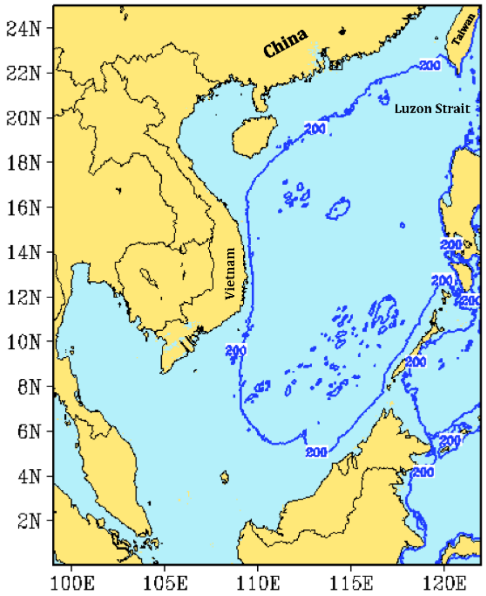

Figure 2. 1 The domain in this work. The contour shows the 200-m isobath in the SCS

2.2 Eddy detection and tracking algorithm

To properly describe eddies in the South China Sea, an eddy detection and tracking method is needed. Most eddy-detection methods are based on a physical feature, a geometric feature, or a hybrid of them (Nencioli et al., 2010). Two typical methodologies are widely used, the W-based method and the winding angle (WA) method (Chen et al., 2011; Xiu et al., 2010; Zhan et al., 2014).

The W-based method is based on a physical parameter W, which describes the relative importance of rotation compared to deformation in the flow (Chelton et al., 2011).

$$W = \left(v_x + u_y\right)^2 + \left(u_x - v_y\right)^2 - \left(v_x - u_y\right)^2$$

u and v represent the eastward and northward velocity components, respectively, and the subscripts x and y indicate partial differentiation. W is used to divide the SSHA field into two parts that are dominated by strain flow (W>0) or vorticity flow (W<0; suspected eddy area). Then, a threshold value of W (W0) is specified to identify an eddy core (Xiu et al., 2010). The eddy size is determined by the closed contour where W=W0. It is slightly problematic to obtain W through differentiation. In addition, if only SSHA data are available, as is the case for some satellite data, only geostrophic velocity can be derived from the SSHA field. Additionally, Chelton et al. (2011) found that the eddy area identified by the closed contour of W does not closely match the closed contour of the SSHA data.

Another popular method is the winding–angle method (WA method), which is based on the geometric assumption that the streamline around the eddy core is close to a circle or a spiral. The accumulated angle of each consecutive segment of the streamline is computed. The streamlines with absolute accumulated angles larger than 2π are defined as closed streamlines (circular or spiral curve). An SSHA extremum in the center that is surrounded by a series of closed streamlines constitutes the eddy structure in the WA method (Zhan et al., 2014). The eddy margin is characterized by the outer closed streamline. The WA method works better than the W-based method in the eastern South Pacific (Chaigneau et al., 2008). However, the WA method also has limitations. The need to approximate the geostrophic velocity field from the SSHA field results in a problem similar to that in the W-based method.

To avoid problems from the calculation of differential and integral operators on discrete fields (Chelton et al., 2011), this research developed an eddy detection and tracking method that was exclusively based on the discrete SSHA fields. In this section, the geometry-based method to detect and to track eddy is presented.

2.2.1 Eddy detection and tracking

The eddy-detection scheme begins with searching for extrema (minima and maxima) in the SSHA field. A center point in a box will be defined as an extremum if the corresponding SSHA is greater (or smaller) than all other points in the box. The difference between the extremum and the mean SSHA value of the neighbors defines the relative intensity (RI) of an eddy.

This algorithm employs boxes of 5 x 5 grid cells, as suggested by Faghmous et al. (2015), who showed that a box of this size is suitable for detecting extrema, while a box with 7 × 7 cells fails with small eddies, and a box with a 3 × 3 neighborhood leads to too many extrema.

The next choice is that of a minimum RI. Too strict thresholds may break an eddy track into several pieces. An automated tracking program cannot adequately address such a situation, as it will terminate a track in the middle and derive more than one track. To avoid this problem, a mild threshold is set for the moment. According to sensitivity tests (M. Zhang et al., 2017), only extrema with |RI|≥ 3 mm will be considered. In addition, an “eddy core” with at least 5 pixels, with one extremum in the center and one pixel in each of the four directions (north, south, east and west), is requested.

The tracking procedure is used to connect the local extrema at consecutive time steps (days). For each extreme at time T, another extreme at time T+1 will be considered as a member of the same track if it fulfills the following criteria:

1. It is the closest extreme to the extreme at time T when all extrema at time T+1 are considered.

2. Taking eddy travel speed and the spatial resolution of STROM simulation into consideration, the distance between the extrema should be less than 25 km.

3. The RI properties of the extrema differ by no more than a factor of 1.5.

As this work focus on eddies with long travel lengths and high intensities, the following filters are applied:

1. The accumulated travel length is required to be at least 100 km.

2. In case some eddies move back-and-forth, a restriction on the distance from the initial position to the final position is implemented (at least 50 km).

3. In the eddy detection part, all eddy centers with a $|RI| \geq 3$ mm are considered. However, tracks are kept only if the strongest extreme RI surpasses the threshold RI_{max}=6 mm.

4. Many small disturbances occur near the shore (especially in shallow water). Since eddies need vertical space to form and develop, a depth criterion is implemented; namely, a track must travel for over 90% of its lifetime in water deeper than 200 m.

Then, for each eddy track that satisfies the criteria listed above, the travel length, lifetime and maximum strength along the track are derived.

2.2.2 Eddy core determination

The outermost closed contour of the SSHA around the eddy core is defined as the eddy edge. According to the geostrophic balance theory, water tends to flow along the SSHA contour. Therefore, the flow along the outermost closed contour can also be considered closed. The SSHA distribution within an eddy is characterized by an extremum (minimum or maximum) in the center and a number of closed SSHA contours around the eddy center, whose SSHA displays a monotonic increase (or decrease) towards the center. Because of this monotonicity, I refer to this method as “M-based”.

An iterative detection procedure aims to identify the largest (if the center is a minimum; otherwise smallest) closed contour that fulfills the monotonicity condition. The eddy size estimation procedure extends the neighborhoods surrounding the eddy core iteratively until the monotonous condition is violated. The condition is fulfilled unless all neighbors around the eddy core are greater (or less) than one threshold. The initial threshold is set to the center value of one eddy. In the following steps, the threshold is always updated by the value of the most recently detected closed contour. As the detected eddy size grows in this way, the threshold increases (or decreases) step by step. Every time the monotonicity is maintained, another larger (smaller) closed contour exists in these neighborhoods, and the contour corresponds to the minimum (or maximum) from these neighborhoods. Then, the eddy size will grow by including one or more points in this new contour, and the value of this contour will be used to update the threshold to check the monotonous condition in next step.

The eddy size is defined as $\mathrm{d} = 2\sqrt{\mathrm{A} / \pi}$, where A indicates the area of the eddy core, and d is the diameter of the eddy if it is a circle.

This M-based method is similar to the method of Faghmous et al. (2015). However, a key criterion is different. In their method, the condition for an eddy size to stop growing is another extremum included in its interior, which differs from our monotonous condition. Their condition could result in an overestimation of the size. On the other hand, the increment of the threshold in their method is defined by users in advance. Too coarse threshold step may fail to obtain an accurate eddy core, but a step that is too fine will require extensive computational time. The appropriate step varies for different eddies, and it is difficult to select one step that is appropriate for all eddies. Overall, our M-based algorithm overcomes the two problems in the method of Faghmous et al. (2015), and is able to derive more precise eddy size from SSHA fields.

2.2.3 Validation of the algorithm

Figure 2.2 shows the detected and filtered eddy points on 2010-01-01 from the STORM daily data based on our M-based method. The sizes and shapes of the masked eddies are consistent with the contour lines of the SSHA fields, which demonstrates the ability of the M-based method to capture the eddy sizes. In some cases, the eddy size may be underestimated due to the interruption of the eddy structure by islands or land. This algorithm also addresses the situation in which SSHA contours cannot be closed due to islands. The M-based method can detect the smallest eddies with structures containing only five points. In this study, I keep all of the small eddies.

In general, cyclonic eddies pump deep water into the upper layers, which causes a cold core. In contrast, anticyclonic eddies lead to the convergence of upper ocean water, resulting in a warm core. To validate our algorithm, I investigate the aggregate features of the temperature gradients in the eddy cores to determine if the eddies identified by the algorithm agree with the observations. I choose the peak eddy points of 2010. A peak eddy point is defined as the eddy point with the maximum intensity along an eddy track. In 2010, there are 30 anticyclonic peak eddy points and 40 cyclonic peak points. Figure 2.3 shows a scatter diagram of the SSHA gradient between the outermost grid point and the eddy center of these peak eddy points and the corresponding seawater temperature gradients (at the surface and a depth of 100 m). It is not surprising that positive (negative) SSHA gradients occur in all cyclonic (anticyclonic) eddies because cyclonic (anticyclonic) eddies are characterized by the minimum (maximum) SSHA in the eddy center point. Most cyclonic eddies have positive SST gradients and positive temperature gradients at a depth of 100 m (T100), and the cold cores within cyclonic eddies are more visible at the surface. Most anticyclonic eddies have positive T100 gradients; however, the warm cores at the surface within anticyclonic eddies are not as obvious as those at a depth of 100 m. Itoh and Yasuda (2010) investigated the structure of anticyclonic eddies in the Subarctic North Pacific and found that most anticyclonic eddies in that region have saline and warm cores, but 15% of anticyclonic eddies have fresh and cold cores. Therefore, the temperature structure in anticyclonic or cyclonic eddies is not completely fixed. The results indicate that the structure of the eddies identified by our algorithm is consistent with current knowledge.

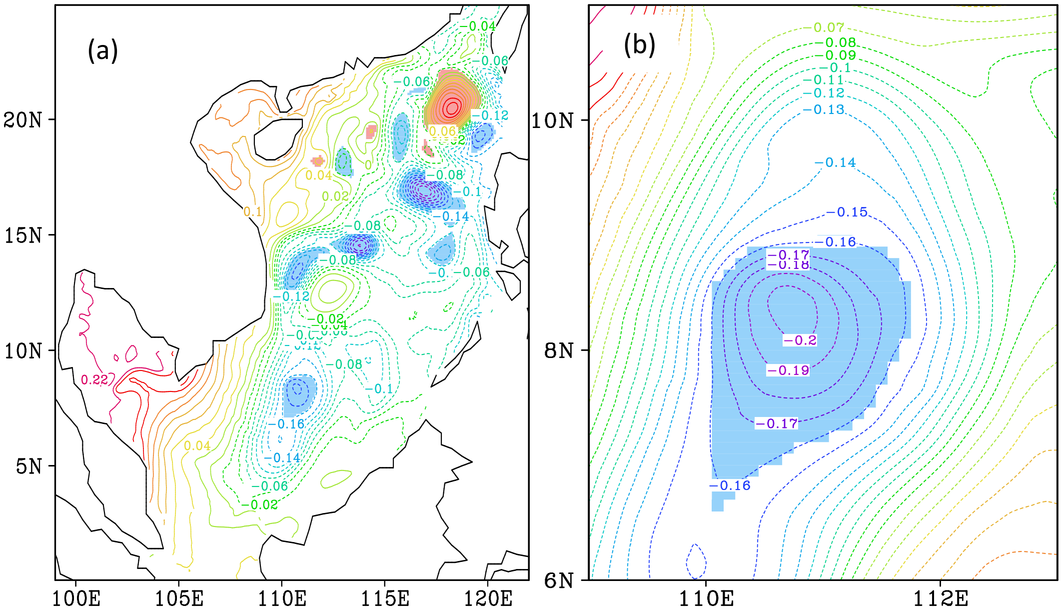

Figure 2. 2 (a) The SSHA distribution (contours) and the eddies detected by the M-based method (blue: CE; red: AE) on 2010-01-01 and (b) the single cyclonic eddies derived from (a).

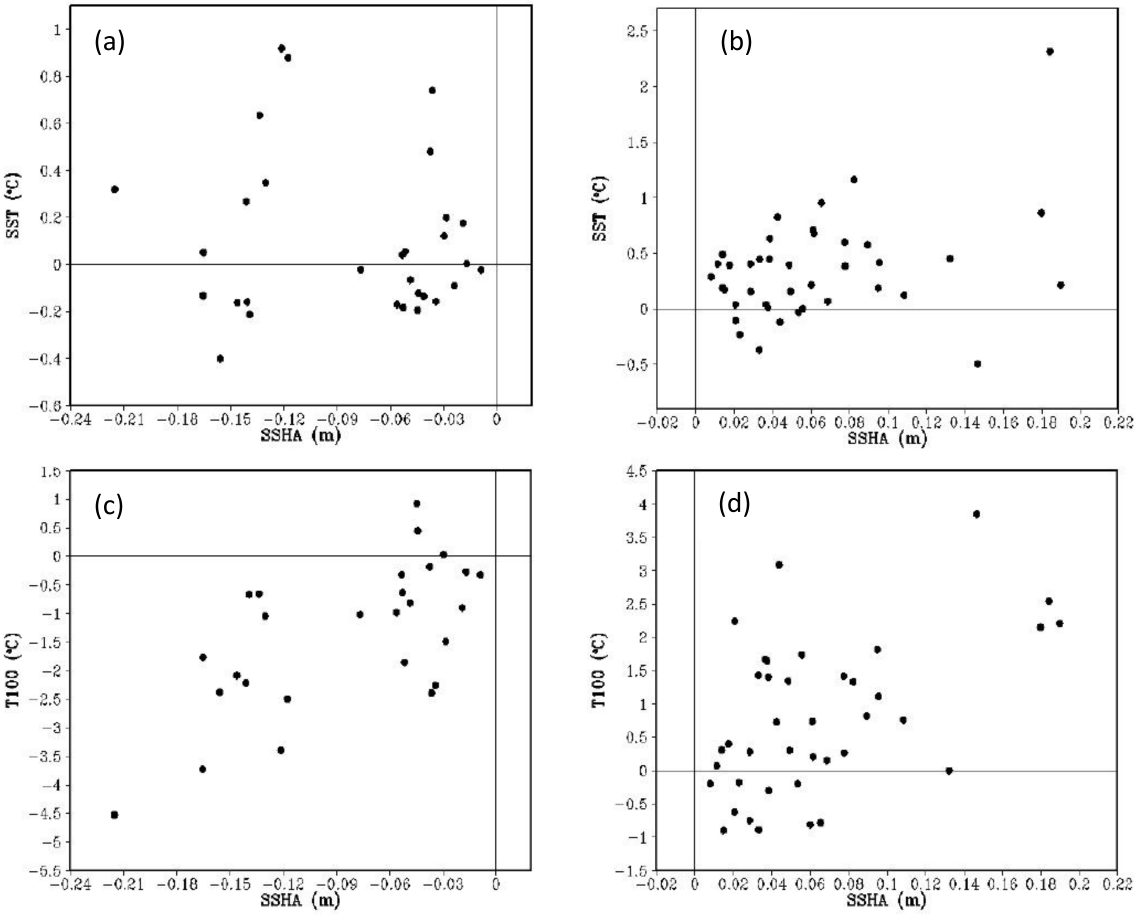

Figure 2. 3 Scatter diagram of the SSHA gradients of the peak eddy points in 2010 and the corresponding seawater temperature gradients ((a) and (b) are SST gradients; (c) and (d) are the temperature gradients at a depth of 100 m). (a) and (c) are for anticyclonic eddies, and (b) and (d) are for cyclonic eddies.

2.3 EOF

The Empirical Orthogonal Function analysis (EOF) is a statistical method to decompose a random vector into its Empirical Orthogonal Functions (EOFs) and the corresponding Principal Coefficients (PCs). In the earth science, the random vector usually is a statistical field indexed by locations. The EOFs are the orthogonal spatial patterns of simultaneous variation, and the PCs are the time series gotten by projecting the vector onto the EOFs. In one pair of EOF and PC, PC indicates the simultaneous variability of the EOF patterns. EOF was proposed by Pearson (1902) and introduced into the Earth Sciences by Lorenz (1956). I refer to the description and the explanation of this method in the book of "Statistical Analysis in Climate Research" by von Storch and Zwiers (1999).

To describe the mathematics of EOF briefly, I introduce a random vector $\vec{\mathrm{X}}$, which is a spatial field with **m** locations. $\vec{\mathrm{X}}$ varies with time and have **t** time steps. For the sake of simplicity, I assume $\vec{\mathrm{X}}$ with the expectation of zero. Then expand $\vec{\mathrm{X}}$ by a finite series as the following equation (2.1):

$$\vec{\mathrm{X}}_t = \sum_{i=1}^{k} \hat{\alpha}_{i,t} \hat{\vec{e}}^{i}$$

In the formula, $\hat{\alpha}_{i,t}$ indicate time coefficients and $\hat{\vec{e}}^{i}$ are fixed patterns. The fixed patterns are required to be orthogonal to make sure that the optimal coefficients can be generated by simply projecting the anomalies onto the patterns. The patterns can be determined when the error

$$\sum_{t}\left(\vec{\mathrm{X}}_t-\sum_{i=1}^{k}\hat{\alpha}_{i,t}\hat{\vec{e}}^{i}\right)^{2}$$

is minimized. In order to find the first EOF pattern $\hat{\vec{e}}^{i}$, I set k=1 and minimize the error:

$$\epsilon_1=\varepsilon\left(\left\|\vec{\mathrm{X}}-\langle\vec{\mathrm{X}},\vec{e}^{1}\rangle\vec{e}^{1}\right\|^{2}\right) \tag{2.2}$$

Then the $\vec{e}^{1}$ can be identified, which is an eigenvector of the covariance matrix of $\vec{\mathrm{X}}$, associated with its largest eigenvalue. The next pattern can be obtained by set k=2 and minimize the error as well. More detailed computation could be found in the book of von Storch and Zwiers (1999).

For the various purposes, EOF analysis has been widely applied in climate research of meteorology and oceanography for various sakes. The application involves deriving dominant modes from a complex vector, investigating the variability of phenomena, removing small-scale related noise and simplifying a large matrix.

In this thesis, EOF analysis has two major applications. In order to estimate the quality of STORM simulation in chapter 3, I derive the dominant modes of sea surface height anomaly and sea surface current from STORM simulation and the reference data sets, by means of EOF analysis. Then I comparing the consistency of STORM simulation with the reference data sets, in terms of the dominant patterns and its variability. In chapter 5, before use canonical correlation analysis to search the linkage between predictands and predictors, EOF analysis is applied for eliminating climate noise of the data and simplify the calculation.

2.4 CCA

The canonical correlation analysis (CCA) is designed for one pair of random vectors $\vec{X}$ and $\vec{Y}$ to search for their strongest joint patterns of variations. Its objective is to find out one pair of patterns $\vec{f}_X$ and $\vec{f}_Y$ to make the correlation ρ between the linear combinations $\beta^X = \langle\vec{X}, \vec{f}_X\rangle$ and $\beta^Y = \langle\vec{Y}, \vec{f}_Y\rangle$ maximum. A second pair of patterns need not only fulfill the same criteria, but also the second combinations is uncorrelated with the first combinations, and so on. It means for every β_i^X and every β_j^Y , their correlation is maximum if i=j, otherwise zero.

This method was first proposed by Hotelling (1936). The related mathematics and the potential application in climate research are described by von Storch and Zwiers (1999). Here I only introduce the CCA briefly according to their book.

For determining the patterns $\vec{f}_X$ and $\vec{f}_Y$, I maximize the correlation of β^X and β^Y:

$$\rho = \frac{\mathrm{Cov}(\beta^X, \beta^Y)}{\sqrt{\mathrm{Var}(\beta^X)\mathrm{Var}(\beta^Y)}} = \frac{\vec{f}_X^{\mathrm{T}}\,\mathrm{Cov}(\vec{X}, \vec{Y})\,\vec{f}_Y}{\sqrt{\mathrm{Var}(\langle\vec{X}, \vec{f}_X\rangle)\mathrm{Var}(\langle\vec{Y}, \vec{f}_Y\rangle)}} \tag{2.3}$$

We choose the particular patterns fulfilling the following conditions:

$$\mathrm{Var}(\langle\vec{X}, \vec{f}_X\rangle) = \vec{f}_X^{\mathrm{T}} \textstyle\sum_{XX} \vec{f}_X = 1 \tag{2.4.1}$$

$$\mathrm{Var}(\langle\vec{Y}, \vec{f}_Y\rangle) = \vec{f}_Y^{\mathrm{T}} \textstyle\sum_{YY} \vec{f}_Y = 1 \tag{2.4.2}$$

Then the correlation can be simplified as:

$$\rho = \vec{f}_X^{\mathrm{T}} \sum_{XY} \vec{f}_Y \tag{2.5}$$

$\sum_{XX}$ and $\sum_{YY}$ are the covariance matrices of $\vec{X}$ and $\vec{Y}$. And $\sum_{XY}$ is the cross-covariance matrix, i.e.

$$\sum_{XY} = \varepsilon\left(\left(\vec{\mathrm{X}} - \vec{\mu}_X\right)\left(\vec{\mathrm{Y}} - \vec{\mu}_Y\right)^{\mathrm{T}}\right) \qquad (2.6)$$

After computation, ρ turns out to be the square root of the eigenvalue corresponding to eigenvectors $\vec{f}_X$ and $\vec{f}_Y$. Then$\sum_{XX} \vec{f}_X$ and $\sum_{YY} \vec{f}_Y$ are the canonical correlation patterns.

Vector $\vec{\mathrm{Y}}$ can be reconstructed as $\hat{R}$ by the following equation according to the canonical patterns $\overrightarrow{F_i^Y}$ and the corresponding time series β_i^Y. Based on the relationship between β_i^Y and β_i^X, vector $\vec{\mathrm{Y}}$ can be constructed by the canonical correlation patterns of itself and the corresponding time series of $\vec{\mathrm{X}}$.

$$\hat{R} = \sum_{i=1}^{K} \beta_i^Y(t)\,\overrightarrow{F_i^Y} = \sum_{i=1}^{k} \rho_i \beta_i^X(t)\,\overrightarrow{F_i^Y} \qquad (2.7)$$

The CCA are often applied to analyze the correlation between two climate factors. Li et al. (2018) used CCA to describe the relationship between low-level jet occurrence over the Bohai Sea and the Yellow Sea and regional large-scale atmospheric circulation. Chen and von Stoch (2013) investigated the seasonal mean flow conditions of the generation of Pola Low, by means of the CCA. Furthermore, Based on the CCA technique, many researchers found the link between regional climate variability and large-scale climate, and then built statistical downscaling models to generate regional climate, like the temperature over Greece (Skourkeas et al., 2013) and extreme precipitation events over the Emilia-Romagna (Busuioc et al., 2008). In chapter 5, I search for the large-scale conditions of eddy activities in the SCS based on the CCA method.

3. Validation of STORM simulation

The validation of STORM simulation has been published as a paper titled “Toward downscaling oceanic hydrodynamics — suitability of a high-resolution OGCM for describing regional ocean variability in the South China Sea” in *Oceanologia*. Now I present the manuscript version of this paper in this chapter.

3.1. Introduction

As the largest semi-enclosed marginal sea located in the southeast Asian waters, the South China Sea (SCS) covers an area of about 3.5 million km^2 in total, with an average depth more than 2000 m and a maximum depth of about 5000m. It is surrounded by China, Vietnam, Philippine Islands, Malaysia and other countries. Via the Luzon Strait, Taiwan Strait and the Strait of Malacca, it connects the Pacific Ocean, East China Sea and Indian Ocean (Fang et al. 2006a; Fang et al. 2012; Fang et al. 2006c; Ho et al. 2000; Hu et al. 2000; Li et al. 2003).

Due to the influence of the East Asian monsoon system, the SCS circulation represents significant seasonal characteristics. Previous studies have been carried out to analyze the features of the SCS circulation. Dale (1956) determined the SCS surface circulation in winter and summer for the first time from the ship drift data, which clearly revealed the seasonal differences. Wyrtki (1961) pointed out that the monsoon is the main driver of the SCS circulation.

The advent of satellite remote sensing technology allowed the analysis of the details of the SCS circulation. Ho et al. (2000) has described the seasonal variability of sea surface height (SSH) based on the TOPEX/Poseidon altimeter data during 1992 to 1997. W. Fang et al. (2006c) used the gridded 11-year AVISO SSH data, which merged data from TOPEX/Poseidon, ERS and Jason, for characterizing the low frequency variability of the SCS surface circulation and to discuss its relationship with El Niño-Southern Oscillation. The conclusion of the annual variability responding to the change of monsoon was confirmed by their study.

Recently, several numerical simulations of the SCS circulation were done. Such simulations help extend our knowledge about past variations beyond the short time period of satellite observations and beyond the sparse sampling of in-situ observation and ship observation. Wei et al. (2003) embedded a fine-grid ocean model of the China Sea into a global model so that open boundary conditions were no longer needed. Their modelled monthly SSH anomalies (SSHA) were similar to the TOPEX/Poseidon data, and the model could seasonably reproduce the SCS Southern Anticyclonic Gyre in summer and the SCS Southern Cyclonic Gyre in winter. Using this model, the seasonal features of the water intruding into the SCS through the Luzon Strait in different ocean layers were investigated. Wang et al. (2006b) modelled the interannual variability of the SCS circulation and its relation to wind stress and El Niño through on an irregular grid. Such numerical simulations allowed the detailed study of processes and physical mechanisms of some mesoscale phenomena, for example, the topographical effect on the coastal upwelling in the north SCS (Wang et al. 2012; Wang et al. 2014).

In spite of those signs of progress, a systematic, detailed, homogeneous and comprehensive description of the SCS circulation on regional and local scales across several decades is hardly available. The “empirical downscaling” methodology may help to generate such descriptions, which will also allow for detection externally driven change as well as projecting possible future change on such regional scales. Most downscaling efforts were directed at atmospheric phenomena (Benestad et al. 2008; von Storch et al. 1993), but a few oceanic applications dealing with local sea level were presented in the 1990s (Cui et al. 1995; von Storch; Reichardt 1997).

An alternative to empirical downscaling is dynamical downscaling using regional dynamical models (e.g., Kauker; von Storch 2000; Schrum et al. 2003); however, this approach is more challenging and cost-intensive than the empirical approach; also the empirical approach may deal with local phenomena, which are possibly less well resolved by dynamical models. Therefore, we explore the potential of the empirical downscaling of oceanic dynamics.

For doing so for the South China Sea (SCS), we need a consistent and homogeneous description of the regional space-time variability in that region. As a first preparational step, we examine the suitability of a multidecadal global simulation “STORM” with the MPI-OM, the high-resolution global ocean model of the Max Planck Institute of Meteorology (MPI; Li; von Storch 2013; von Storch et al. 2012), which was forced by NCEP atmospheric re-analyses.

The high resolution of about $1/10^{o}$ makes STORM capable to describe the small-scale features, while the temporal coverage over 60 years enables STORM to analyze the long-term variability of the SCS circulation. In addition, STORM provides the large-scale states. Therefore, STORM is a good choice for constructing the statistical relationship between large and small scales. Also all relevant second-moment statistics have been archived by accumulating two-variable-products at every time step (J. von Storch et al. 2012).

In this paper, we first assess the performance of STORM in describing the SCS circulation, by comparing with AVISO altimeter measurements and ocean re-analysis dataset C-GLORS. In section 2, these three data sets are described in detail. Section 3 presents the comparisons, in terms of sea surface height anomalies (SSHA), surface current and sea surface temperature (SST). Eventually, for demonstration, an empirical downscaling model has been constructed (section 4), which allows deriving the monthly seasonal near-surface regional throughflow in the South China Sea from the regional wind fields.

3.2. Dataset description

Detailed descriptions about all the data sets are already presented in chapter 2, so we remove this part in the paper to avoid a repeat.

3.3. Assessing the realism of the STORM data

The three data sets, STORM, C-GLORS and AVISO cover different variables, and descriptions for different time windows. The satellite AVISO contains only sea surface height for 1993-2014, while the re-analysis C-GLORS provide the full range of dynamical variables for 1982-2013 and STORM for 1950-2010.

We consider AVISO as the data set closest to reality; thus we examine first, how well the derived products C-GLORS and STORM compare with AVISO. The realism of C-GLORS in terms of SSHA, leads us to assessing the quality of STORM with respect to other variables by comparing it with C-GLORS. The first step demonstrates the suitability of using all C-GLORS variables; the second step suggests that STORM provides a realistic description across the 60 year time window 1950-2012.

3.3.1 SSHA in AVISO, C-GLORS and STORM

SSHA is often used to analyze the ocean dynamics and the upper layer circulation (Fang et al. 2006c; Li et al. 2003; Wei et al. 2003). This data is available from AVISO in 1993-2014. For the comparisons with C-GLORS and STORM, the joint period from 1993 to 2010 has been chosen.

The observed AVISO-SSHA is the actual state subject to the influences of dynamical, eustatic and steric effects, whereas the modelled SSHA from STORM and C-GLORS only describe the dynamical effects and not eustatic and steric effects. According to the fifth report of IPCC (Stocker 2014), the growth of the global mean sea level since the 1970s is mostly caused by the thermal expansion of global warming and glacier loss. For removing the difference influenced by eustatic and steric effect, we subtract the trend of AVISO. In case that the trend related to dynamical effect is removed as well, for fair comparison, SSHA from C-GLORS and STORM are also detrended.

The climatological seasonal mean states of detrended SSHAs of STORM and C-GLORS (Fig. 1) show good agreement with AVISO. In winter (DJF), basin-wide low SSHAs control the east part of the SCS, which presents the cyclonic currents in the upper layer in the whole SCS. Furthermore, in these three datasets, two low SSH centers located in the north and southern SCS respectively. In summer (JJA), the situation is just opposite. Anti-cyclonic currents dominate the SCS region in all the three datasets, however a maximum SSHA over 0.1 m appears near the Luzon Strait in AVISO and C-GLORS, which is a little lower in STORM.

The (temporal) standard deviation of the seasonal means represents interannual variability. The patterns of detrended SSHA standard deviation distributions (Fig. 2) for the four seasons of three datasets are similar. As December in 1992 is not available, there are only 17 months in winter (DJF), but 18 months in other three seasons. All of them show that, in winter and spring, the deviation near Luzon Strait is always higher than adjacent seas, and in summer and autumn, strong variability centers in the Vietnam’s coast water. Compared with AVISO and C-GLORS, the STORM simulates stronger variability in Luzon Strait in summer and autumn, yet weaker variability in the Vietnam coast in winter and spring. In summer and autumn, the area of the center with strong variability near Vietnam is closer to AVISO, compared with C-GLORS.

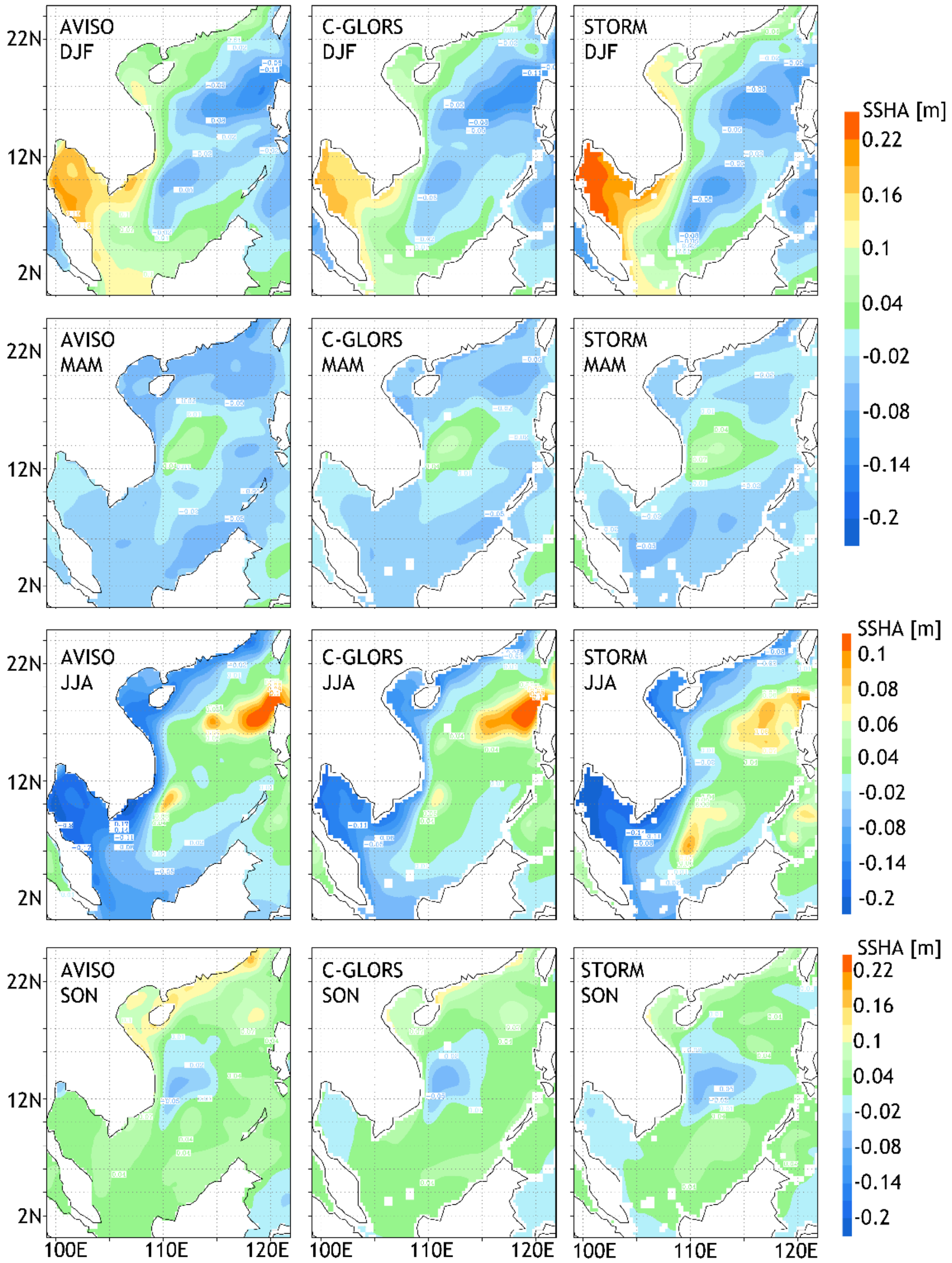

Figure 1 1993-2010 Seasonal means of detrended sea surface height anomalies (SSHA) [m] according to AVISO, C-GLORS and STORM. From top to bottom: DJF, MAM, JJA and SON.

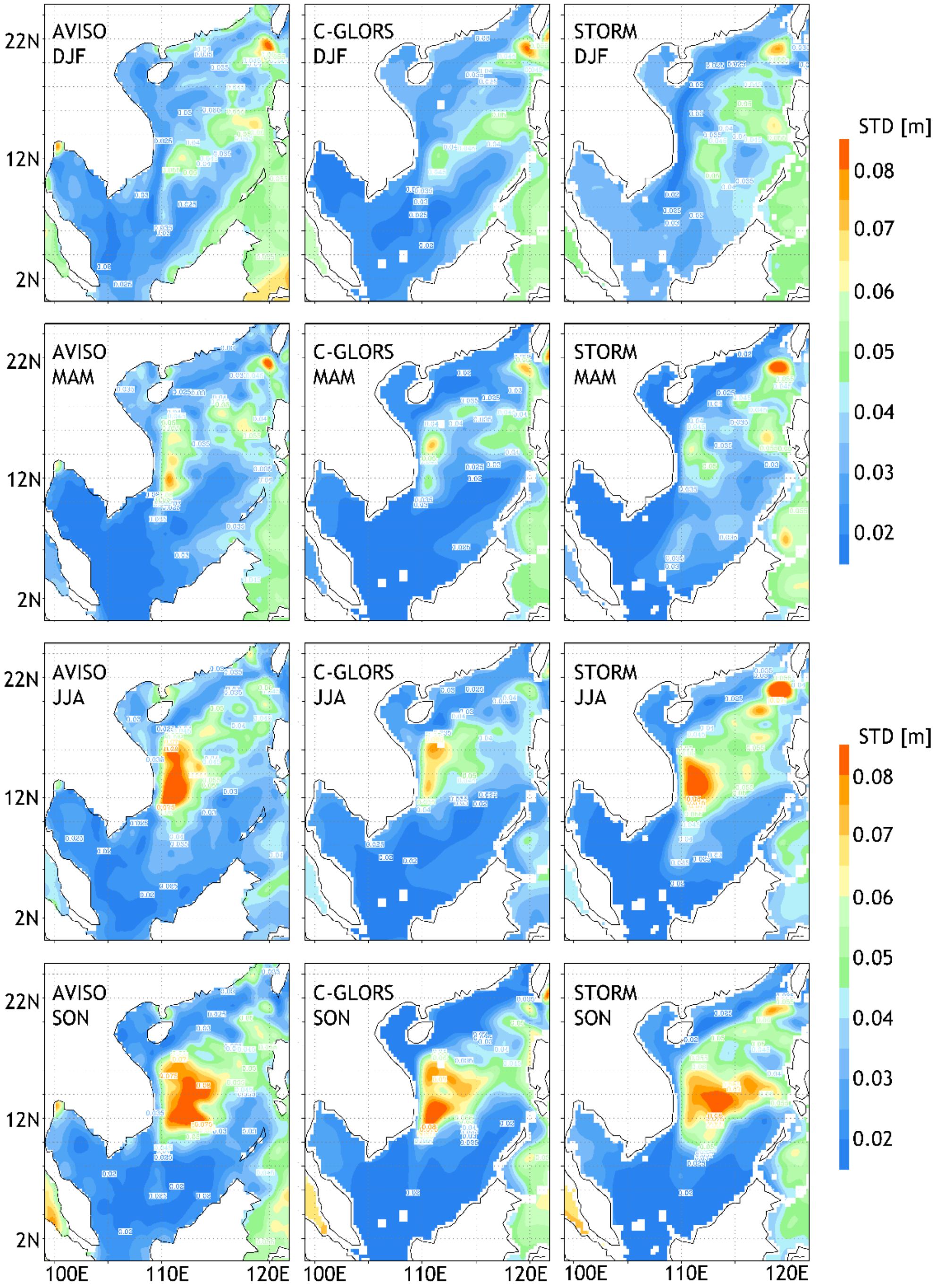

Figure 2 1993-2010 Standard deviations (STD) [m] of seasonal detrended SSHA according to AVISO, C-GLORS and STORM. From top to bottom: DJF, MAM, JJA and SON.

Empirical Orthogonal Functions (EOF) decompose the time series of SSHA fields, several orthogonal modes capture the main variability (von Storch; Zwiers 1999a; Wang et al. 2006b). We apply the EOF decomposition to the three detrended datasets, after removing the mean annual cycle (by subtracting a multi-year monthly average). The EOFs have been normalized so that the standard deviation of the time coefficients (principal component, PC) is 1 – so that the different intensity of the EOFs is given by the patterns.

The main feature of the first EOF pattern (EOF1; Fig. 3) describes an overall simultaneous in- or decrease in the SCS. The amplitude in the east is greater than it in other regions. The EOF1s of C-GLORS and STORM are generally consistent with AVISO. However, a small negative center with small area and weak intensity appears in C-GLORS and three similar centers occur in STORM. Seen from the figures, also the EOF time series for three datasets vary similarly. The time series in C-GLORS and STORM closely correlate with AVISO, with the correlation coefficients of 0.94 and 0.91, respectively. In 1997, SSHAs in all three datasets dropped suddenly and then rebounded quickly in 1998. With respect to the represented percentage of the variance, 25.1% in STORM is closer to 27.0% in AVISO, than 36.6% in C-GLORS.

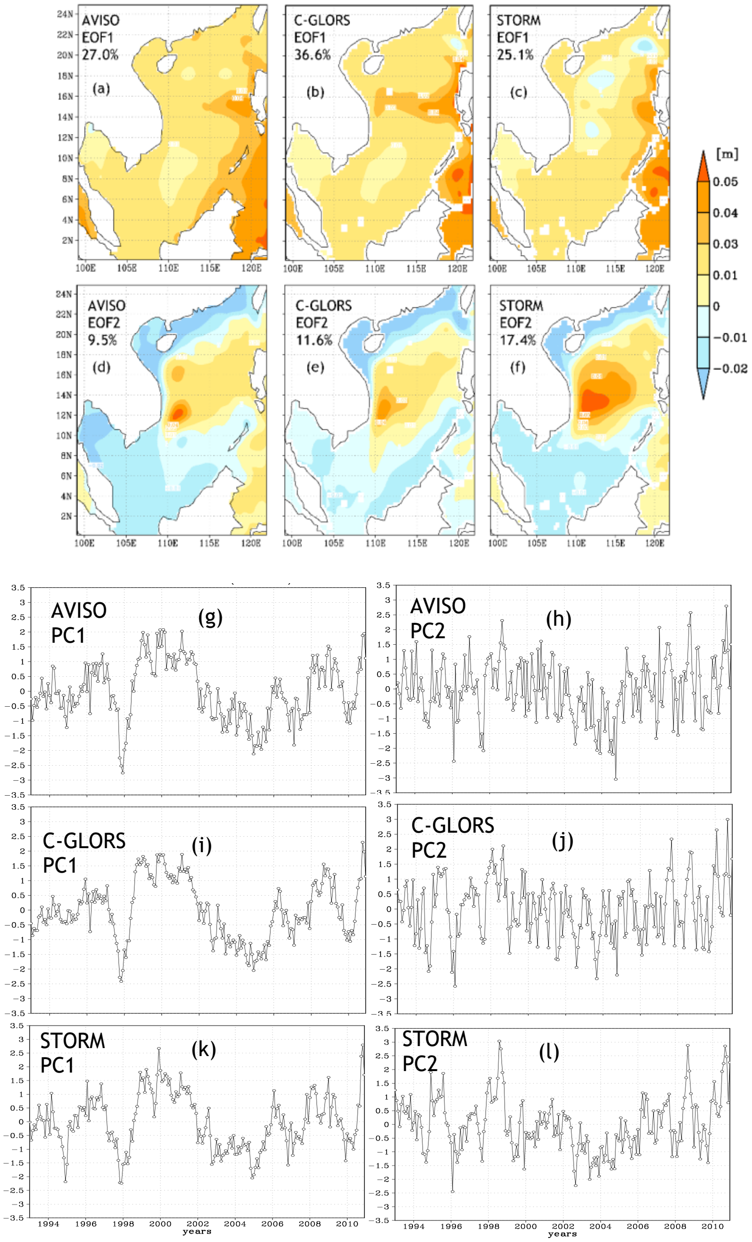

Figure 3 (a-f) The first two EOFs [m] of 1993-2010 monthly detrended SSHA (removing mean annual cycle) according to AVISO, C-GLORS and STORM. From top to bottom: EOF1 and EOF2. (g-l) The time coefficients for the first two EOFs of AVISO (top), C-GLORS (middle) and STORM (bottom), after detrending and subtraction of the mean annual cycle. From left to right: EOF1 and EOF2.

The second EOF(EOF2) patterns in three datasets all show a strong anti-cyclonic gyre located off the Vietnam coast and extending northeastward to reach Philippine Islands, covering most part of the north SCS. The remaining areas are associated with negative value. The coverage of intensity over 0.05 m in STORM is larger than that in AVISO, while the positive values in C-GLORS are all under 0.05 m. The percentages of variance described by both STORM and C-GLORS are greater than AVISO. Their EOF2 coefficient time series of C-GLORS and STORM show correlations with AVISO 0.80 and 0.77, respectively.

Our analysis demonstrates that C-GLORS and STORM have the ability to capture the main variability features of the SCS dynamics in terms of seasonal variance and interannual variability of SSHA. C-GLORS shows greater similarity, which is not surprising as it has assimilated AVISO satellite data. We think the similarity of SSHA in AVISO and C-GLORS points to the plausibility that also other parameters of C-GLORS may be considered mostly realistic. Therefore, we will continue assessing STORM, with C-GLORS as a reference, in the following chapter. In the following, we assess the description of surface currents and SST in the joint period 1982-2010 shared by C-GLORS and STORM.

3.3.2 Surface current fields in C-GLORS and STORM

The first level for ocean horizontal current fields in STORM is at 6m depth, so we choose this level as surface to perform comparison and get the C-GLORS currents at 6m depth through vertical interpolation.

The seasonal mean surface current fields of STORM and C-GLORS (Fig. 4) show similar variability.

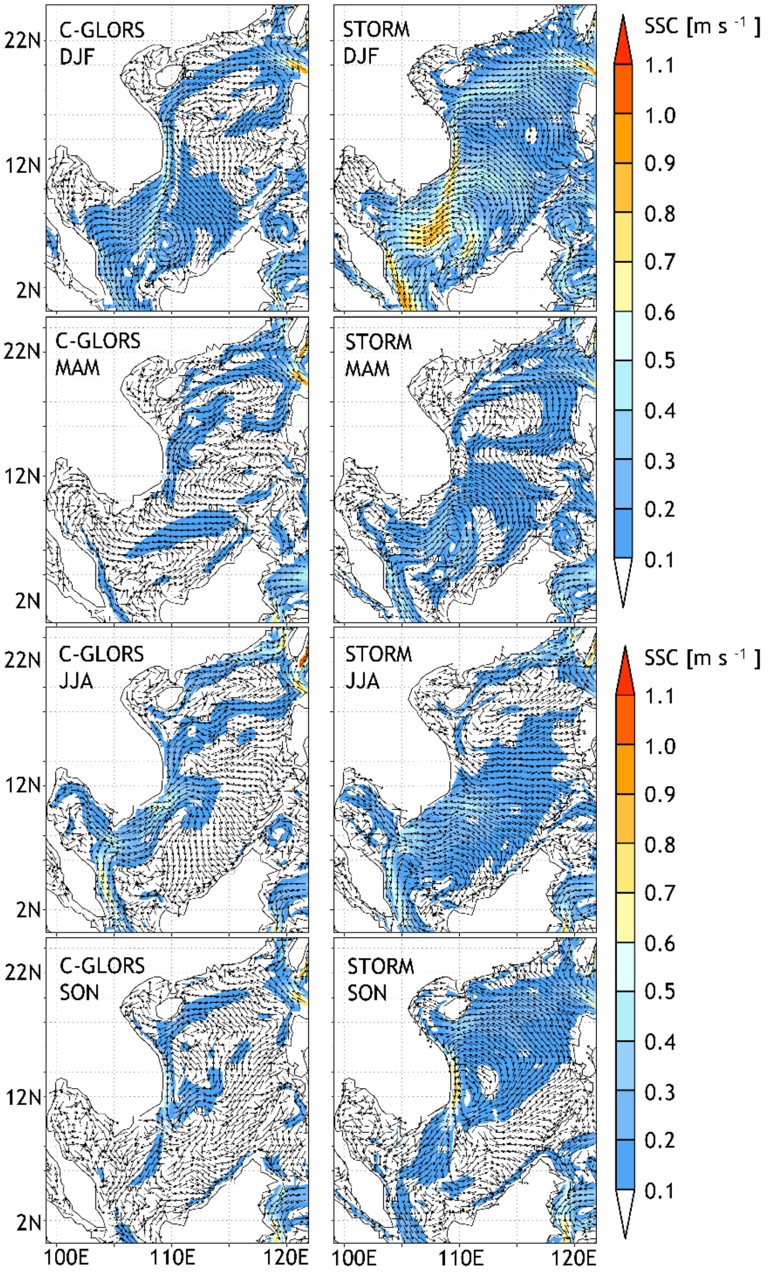

Figure 4 1982-2010 Seasonal mean of sea surface currents (at 6m depth) [m s-1] according to C-GLORS and STORM. From top to bottom: DJF, MAM, JJA and SON.

In winter, strong counterclockwise currents dominate the southern SCS. The Kuroshio intrudes through the Luzon Strait from east to west and then divides into two branches, with the smaller one moving northward into the Taiwan Strait, the bigger one moving westward and then turning southward as a strong western boundary current along the coast. High-speed currents take place in the Luzon Strait, along the western boundary of the SCS (especially along the east coast of Malay Peninsula), and in the large cyclonic eddy of the southern SCS.

In summer, the strong currents along western boundary turn northward, which is consistent with the SCS monsoon, and clockwise currents occupy the southern SCS. At the same time, a strong flow offshore the Vietnam meanders to the central SCS and another flows northward along the southeast coast of China. In spring and autumn, two cyclonic eddies locate in the northern and southern SCS respectively. The seasonal patterns presented in STORM and C-GLORS are alike. But, the speeds in STORM are generally higher than those in C-GLORS, which may be due to the higher spatial resolution of STORM which may allow the simulation of more small-scale phenomena.

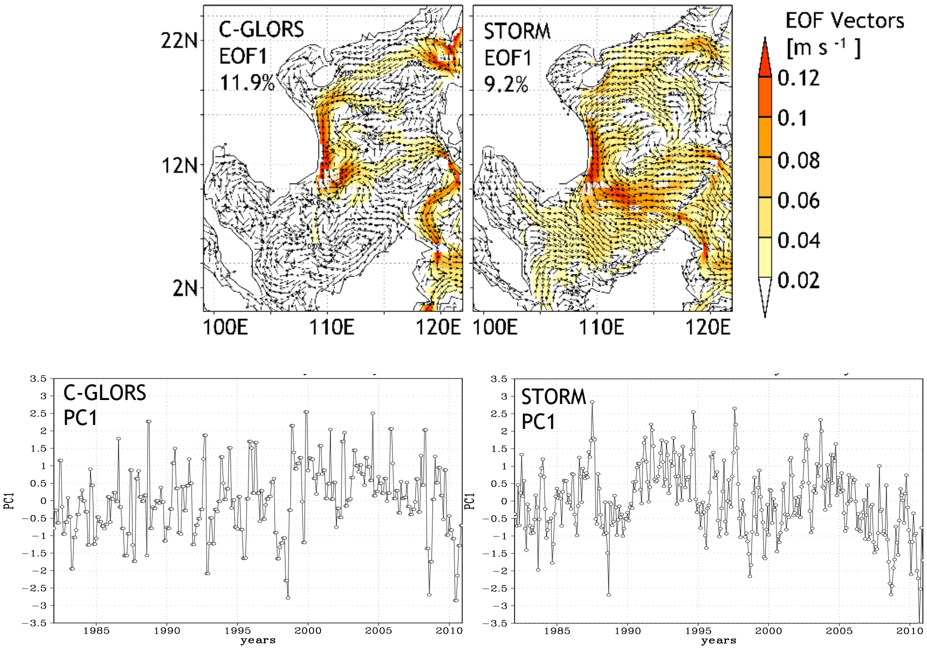

Figure 5 The first vector EOF [m s^{-1}] and the corresponding coefficient of 1982-2010 monthly sea surface currents (SSC; at 6m depth) according to C-GLORS and STORM

The EOFs of sea surface current (after subtracting the annual cycle; Fig. 5) from the two data sets show similar inter-annual variability and explain the similar variance (11.9% in C-GLORS and 9.2% in STORM). The main features of the EOF1 patterns from both two data are the strong alongshore southward currents and a gyre located in the middle SCS. The currents intrude into the SCS from the Pacific through the Luzon Strait and flow into the Pacific through the passage at the south of Philippines. The current speeds in STORM are a little higher than in C-GLORS for the region with slow (less than 0.02 m s-1) currents.

3.3.3 SST in C-GLORS and STORM datasets

The distribution of SST can be deeply influenced by the ocean currents and its variance can be regarded as an important indicator of current variability, including vertical currents. In this section, SST is considered for evaluating the ability of the STORM dataset to reproduce the SCS dynamics.

The distributions of SST in the SCS (Fig. 6) show obvious seasonal differences. In winter, spring and autumn, most isotherms show northeast-southwest direction. The closer the area is to the Equator, the hotter the sea surface is. The SST in the SCS in summer is almost uniform but, with marked small upwelling regions in the southeast of China and near Vietnam. Previous studies (Fang et al. 2012; Wang et al. 2012; Wang et al. 2014; Xie et al. 2003) have demonstrated the presence of regional upwelling, which brings much colder water from deeper layer to the surface. STORM generates higher temperatures in summer in most regions, and it presents a stronger upwelling with larger temperature gradient than C-GLORS. The area with coldest seawater and largest gradient off the Southeast Vietnam coast is very close to the land, then, with the limitation of horizontal resolution, C-GLORS may not be able to resolve these very small-scale phenomena. So STORM has an advantage in this case. The study of Tim et al. (2015a) has found similarly colder SST in STORM compared with coarser observations in the South Atlantic.

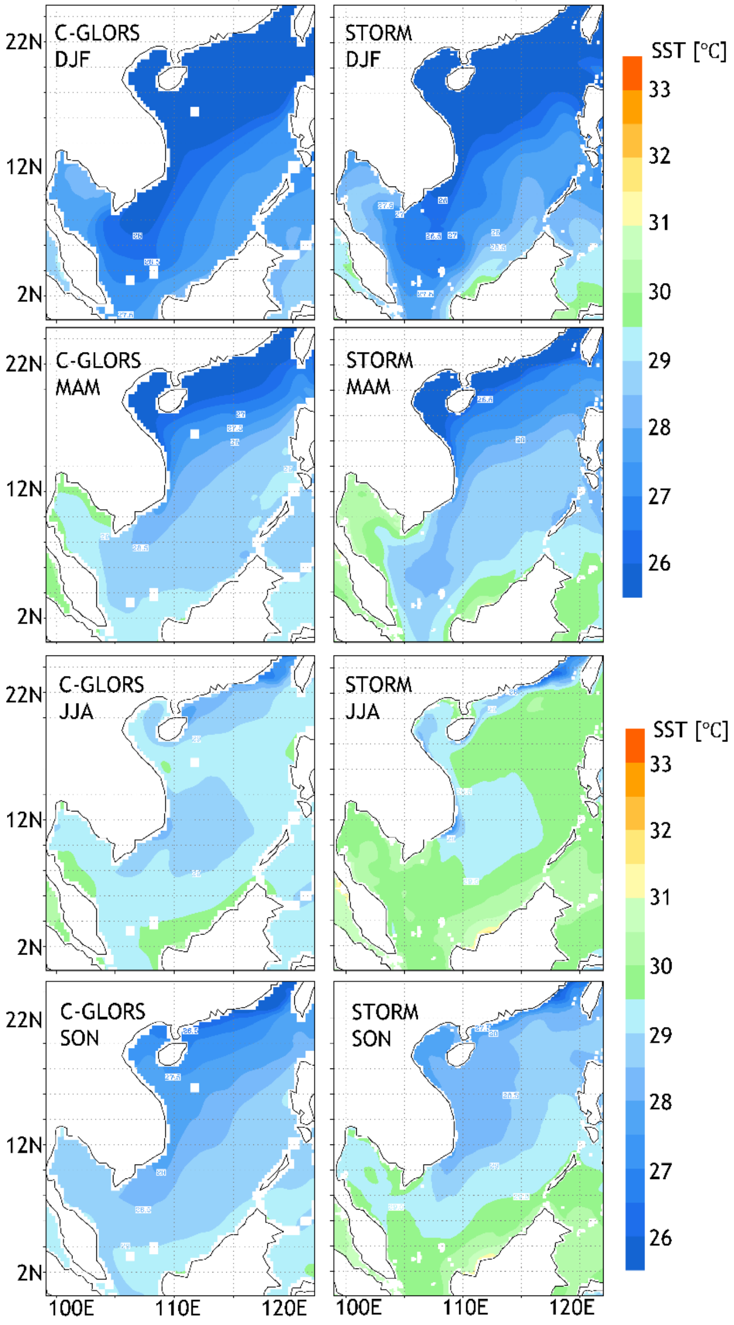

Figure 6 1982-2010 seasonal means of sea surface temperature (SST) [℃] according to C-GLORS and STORM. From top to bottom: DJF, MAM, JJA and SON.

3.4 A case of regional ocean downscaling

According to the assessment above, the capability of STORM to describe the large-scale state and small-scale variability has been verified. STORM is forced with atmospheric states given by NCEP, which is believed to be mostly homogenous since 1958 in describing "large-scale" (regional) variability. Thus, the STORM data set should be suitable for building empirical downscaling models for specifying regional and local phenomena and their statistics in the ocean.

For demonstrating this option, we have built one empirical downscaling model, as an example. As predictand we use the surface throughflow in the South China Sea and its neighboring seas (0-25°N, 99°-122°E), as given by the time series of the 1st EOF of deseasonalized monthly currents on the 0.25° grid (Fig. 5); as predictors the monthly wind speed at 10 m height (0-25°N, 99°-122°E, including the land) as given by the 2.5° gridded NCEP re-analysis. The empirical model linking the predictors and the predictand is multiple linear regression (MLR)

As the instability of the quality of the NCEP1 before the year 1958, this experiment is performed during the period of 1958-2010. We choose the first 33 years (with 396 months) as the training period to construct the model and the last 20 years (with 240 months) as validation period.

There are several preparational steps to pre-process the data:

First, the annual cycle in both the predictors and the predictands are removed for both two periods.

Second, for the training period 1958-1990, after detrending the data, we get PC1_C of the detrended and de-seasonalized currents C, and the PCs_W of the detrended and deseasonalized winds W. The pattern EOF1_C (not shown) presents almost the same pattern as that one given in Figure 5. Using these PCs, we build the MLR models.

Third, for the validation period, the currents (and winds) are projected on EOF1_C (EOFs_W) to generate the predictand PC1_C and the predictors PCs_W. The skill of the MLR model can be assessed by "predicting" PC1_C in the validation period by feeding the MLR model with the predictors PCs_W.

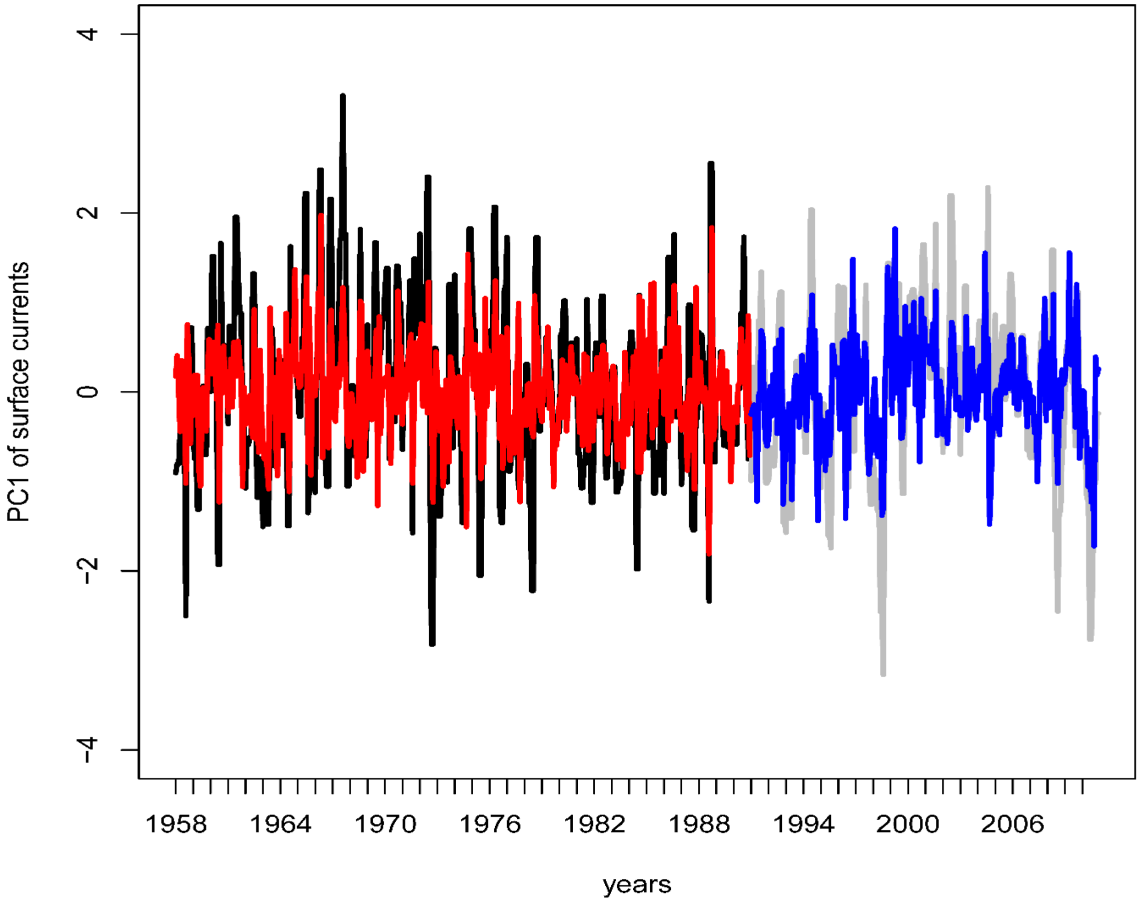

Figure 7 The original PC1 (the black line and the gray line) and the fitted PC1 (the red line and the blue line) of the surface currents for the training period and the validation period.

The number of PCs of predictors to be used for the construction of the downscaling model has an effect on the model skill. Too many PCs involved in the construction may result in the overfitted problem (Titus et al, 2013). After some tests, we find that the first 3 PCs of wind as predictors for the model construction performs well. The original PC1 and the fitted PC1 for both the training period and the validation period are shown in figure 7. The correlation coefficients between the predictand and the predicted PC1_C amounts to 0.55 in the training period 1958-1990, and 0.66 in the validation period (1991-2010).

The regressed predictand exhibits a similar, albeit smaller, variability to that one during the training period. We conclude that the multiple linear regression based on the principal component is good enough to build the statistical model to predict the non-seasonal variability of surface currents in the SCS.

3.5. Conclusions

Often, studies on the statistics of meso-scale SCS dynamics and scale-interactions suffers from insufficient observations in terms of spatial resolution and temporal coverage. One way of overcoming this limitation is to build empirical downscaling models for regional and local oceanic phenomena. A major problem for doing so is the availability of suitable data sets for constructing such empirical models.

One approach for solving this problem is to use multi-decadal simulations with high-resolution ocean models forced by atmospheric reanalyses. For instance, the German consortium STORM project has produced a global high-resolution ocean dataset STORM, integrated with atmospheric forcing for the time period 1950 to 2010 and a one-tenth degree horizontal resolution. This dataset is found to generate realistically the variability on large and small scales in the SCS and statistics of small-scale features of the SCS dynamics. Using this data set, we built a statistical models of the links between large and small scales in the SCS, i.e. an empirical downscaling model.

For determining the STORM data as suitable, we introduce the global gridded AVISO satellite observations and the ocean re-analysis dataset C-GLORS in this study to evaluate the ability of STORM to reproduce the SCS dynamical structure. As C-GLORS have much more parameters than AVISO, for the joint period and the shared variable SSHA, we first verified the quality of C-GLORS and STORM. After that, we regard C-GLORS as “observations” to carry out the assessment of other variables (surface currents and SST) generated by STORM.

Overall, STORM and C-GLORS show good agreement with AVISO in reconstructing the SCS dynamical characteristics. The seasonal variability of SSHA resolved from STORM is very close to AVISO with the maximum center in the same locations, even though C-GLORS assimilating the AVISO altimeter data is closer. The distributions of maximum SSHA standard deviation for four seasons from the three datasets are alike, but C-GLORS and STORM differ from the observed distribution, with respect to the intensity in winter and spring, the area of strong inter-annual variability in summer and autumn off the southeast Vietnam. The EOF decomposition of SSHA identifies similar patterns of interannual variability. A difference is that emergence of several small opposite centers far away from the coastline presented in EOF1 patterns of C-GLORS and STORM. The reason is not clear.

STORM hindcasts the same seasonal upper circulation and inter-annual variability as C-GLORS, however, it generates stronger current intensity, which may be caused by the increase in resolution. As for SST, even though STORM still overestimates the SST for most areas, the temperature distribution of STORM shows great similarity with C-GLORS, with colder temperature off the Vietnam coast (the strong upwelling area) in summer. The STORM description of the SCS circulation and some small-scale phenomena near coastline, for instance upwelling, is quite satisfactory.

A major albeit technical advantage of STORM is not only the availability of more dynamical variables, but also the longer time period, namely 1950, or 1958, until 2010.

Taking advantage of STORM, one statistical downscaling model has been built successfully to estimate the non-seasonal variability of the SCS surface currents for the past 60 years. The multiple linear regression based on the principal component shows skill.

While this downscaling model is merely an example demonstrating the potential, further downscaling models will be built in this spirit on the regional and local phenomena in the South China Sea, related to the formation of eddies, to coastal upwelling and other phenomena. These models may then also be used to derive scenarios of possible future change but also to change prior to 1950.

Acknowledgments:

We thank the Helmholtz–Zentrum Geesthacht (HZG) for supporting the authors' research and the Chinese Scholarship Council (No.201406330048) for funding the first author's studying abroad at the HZG. The authors are grateful to the Max Planck Institute of Meteorology (MPI) for providing the STORM simulations.

References

AVISO, 1996. AVISO User Handbook Merged Topex/Poseidon Products (GDR-Ms), AVI-NT-02-101-CN Edition 3.0, Romonville St-Agne, France.

AVISO, 2009. SSALTO/DUACS user handbook: (M) SLA and (M) ADT near-real time and delayed time products, Reference: CLS-DOS-NT-06-034.

Benestad R.E., Hanssen-Bauer I., Chen D., 2008. Empirical-statistical downscaling. World Scientific Publishing Company Incorporated, Singapore.

Cheng X.H., Xie S.P., Du Y., Wang J. Chen X. Wang J., 2016. Interannual-to-decadal variability and trends of sea level in the South China Sea. Clim. Dyn. 46, 3113–3126, DOI: 10.1007/s00382-015-2756-1.

Cui M.C., von Storch H., Zorita E., 1995. Coastal Sea-Level and the Large-Scale Climate State - a Downscaling Exercise for the Japanese Islands. Tellus Ser. A 47(1), 132-144, DOI: 10.1034/j.1600-0870.1995.00008.x.

Dale W.L., 1956. Wind and Drift Currents in the South China Sea. Malays. J. Trop. Geogr. 8, 1-31.

Fang G.H., Chen H.Y., Wei Z.X., Wang Y.G., Wang X.Y., Li C.Y., 2006. Trends and interannual variability of the South China Sea surface winds, surface height, and surface temperature in the recent decade. J. Geophys. Res 111(C11S16), DOI: 10.1029/2005JC003276.

Fang G.H., Wang G., Fang Y., Fang W.D., 2012. A review on the South China Sea western boundary current. Acta Oceanolog. Sin. 31(5), 1-10, DOI: 10.1007/s13131-012-0231-y.

Fang W.D., Guo J.J., Shi P., Mao Q.W., 2006. Low frequency variability of South China Sea surface circulation from 11 years of satellite altimeter data. Geophys. Res. Lett. 33(L22612), DOI: 10.1029/2006GL027431.

Ho C.R., Zheng Q.N., Soong Y.S., Kuo N.J., Hu J.H., 2000. Seasonal variability of sea surface height in the South China Sea observed with TOPEX/Poseidon altimeter data. J. Geophys. Res. Oceans 105(C6), 13981-13990, DOI: 10.1029/2000JC900001.

Hu J., Kawamura H., Hong H., Qi Y., 2000. A review on the currents in the South China Sea: seasonal circulation, South China Sea warm current and Kuroshio intrusion. J. Oceanogr. 56(6), 607-624, DOI: 10.1023/A:1011117531252.

Kauker F., von Storch H., 2000. Statistics of "synoptic circulation weather" in the North Sea as derived from a multiannual OGCM simulation. J. Phys. Oceanogr. 30(12), 3039-3049, DOI: 10.1175/1520-0485(2000)030<3039:SOSCWI>2.0.CO;2.

Li H.M., von Storch J.S., 2013. On the Fluctuating Buoyancy Fluxes Simulated in a 1/10 degrees OGCM. J. Phys. Oceanogr. 43(7), 1270-1287, DOI: 10.1175/JPO-D-12-080.1.

Li L., Xu J.D., Jing C.S., Wu R.S., Guo X.G., 2003. Annual variation of sea surface height, dynamic topography and circulation in the South China Sea - A TOPEX/Poseidon satellite altimetry study. Sci. China Ser. D. 46(2), 127-138, DOI: 10.3969/j.issn.1674-7313.2003.02.004.

Schrum C., Siegismund F., JOHN M., 2003. Decadal variations in the stratification and circulation patterns of the North Sea. Are the 1990s unusual?, ICES Mar. Sci. Symp. pp. 121-131.

IPCC, 2013, Summary for Policymakers. In: Climate Change 2013: The Physical Science Basis. Contribution of Working Group I to the Fifth Assessment Report of the Intergovernmental Panel on Climate Change. Cambridge University Press, Cambridge, United Kingdom and New York, NY, USA,pp 10-11.

Storto A., Masina S., 2014. Validation of the CMCC Global Ocean Eddy-Permitting Reanalysis (C-GLORS), Centro Euro-Mediterraneo sui Cambiamenti Climatici, Bologna, Italy.

Storto A., Masina S., Navarra A., 2016. Evaluation of the CMCC eddy-permitting global ocean physical reanalysis system (C-GLORS, 1982-2012) and its assimilation components. Q. J. R. Meteorolog. Soc. 142(695), 738-758, DOI: 10.1002/qj.2673.

Tim N., Zorita E., Hunicke B., 2015. Decadal variability and trends of the Benguela upwelling system as simulated in a high-resolution ocean simulation. Ocean Sci. 11(3), 483-502, DOI: 10.5194/os-11-483-2015.

Titus, M. L., Sheng, J., Greatbatch, R. J., & Folkins, I., 2013. Improving Statistical Downscaling of General Circulation Models. Atmos. Ocean 51(2), 213-225, DOI: 10.1080/07055900.2013.774259.

von Storch H., Reichardt H., 1997. A scenario of storm surge statistics for the German bight at the expected time of doubled atmospheric carbon dioxide concentration. J. Clim. 10(10), 2653-2662, DOI: 10.1175/1520-0442(1997)010<2653:ASOSSS>2.0.CO;2.

von Storch H., Zorita E., Cubasch U., 1993. Downscaling of Global Climate-Change Estimates to Regional Scales - an Application to Iberian Rainfall in Wintertime. J. Clim. 6(6), 1161-1171, DOI: 10.1175/1520-0442(1993)006<1161:DOGCCE>2.0.CO;2.

von Storch H., Zwiers F.W., 1999. Statistical analysis in climate research. Cambridge university press, pp 293-305.

von Storch J.-S., Eden C., Fast I., Haak H., Hernández-Deckers D., Maier-Reimer E., Marotzke J., Stammer D., 2012. An estimate of the Lorenz energy cycle for the world ocean based on the STORM/NCEP simulation. J. Phys. Oceanogr. 42(12), 2185-2205, DOI: 10.1175/JPO-D-12-079.1.

Wang D.X., Shu Y.Q., Xue H.J., Hu J.Y., Chen J., Zhuang W., Zu T.T., Xu J.D., 2014. Relative contributions of local wind and topography to the coastal upwelling intensity in the northern South China Sea. J. Geophys. Res. Oceans 119(4), 2550-2567, DOI: 10.1002/2013JC009172.

Wang D.X., Zhuang W., Xie S.P., Hu J.Y., Shu Y.Q., Wu R.S., 2012. Coastal upwelling in summer 2000 in the northeastern South China Sea. J. Geophys. Res. Oceans 117(C04009), DOI: 10.1029/2011JC007465.

Wang Y., Fang G., Wei Z., Qiao F., Chen H., 2006. Interannual variation of the South China Sea circulation and its relation to El Niño, as seen from a variable grid global ocean model. J. Geophys. Res 111(C11S14), DOI: 10.1029/2005JC003269.

Wei Z.X., Fang G.H., Choi B.H., Fang Y., He Y.J., 2003. Sea surface height and transport stream function of the South China Sea from a variable-grid global ocean circulation model. Sci. China Ser. D. 46(2), 139-148, DOI: 10.3969/j.issn.1674-7313.2003.02.005.

Wyrtki, K,1961 "Physical oceanography of the southeast Asian waters, Scientific results of marine investigations of the South China Sea and the Gulf of Thailand, NAGA Rep. 2." Scripps Inst. of Oceanogr., La Jolla, California. 195p.

Xie S.P., Xie Q., Wang D.X., Liu W.T., 2003. Summer upwelling in the South China Sea and its role in regional climate variations. J. Geophys. Res. Oceans 108(C83261), DOI: 10.1029/2003JC001867.

4. Statistics of travelling eddies in 1950-2010

4.1 Introduction

The goal of this chapter is to improve our understanding of the multidecadal statistical characteristics and the variability in eddy activity by examining a 61-year time model hindcast STORM, which was found to properly reproduce the main features of the SCS circulation (M. Zhang and von Storch, 2017) in Chapter 3. The added value of this endeavor is the provision of a database that allows

- a more robust examination of the distribution and variation in the ocean energy, momentum and biochemical regimes,
- an assessment of the conditions of the regional eddy dynamics by large-scale phenomena, which will allow for the future states of the eddy regime in the SCS to be forecasted or projected.

This chapter examines the *climatology* of travelling SCS eddies, including the annual cycles, interannual variabilities and long-term trends of their number, intensity and size. In doing so, I are able to identify and track eddies and determine the intensities and sizes of the eddies in STORM.

This chapter investigates the statistical features of and variability in the travelling eddies in the SCS on different time scales. It does not directly contribute to improving our knowledge about their dynamics.

To avoid problems due to the calculation of differential and integral operators on discrete fields (Chelton et al., 2011), the new eddy detection and tracking method described in Chapter 2 is used in this chapter. In section 4.2, the STORM simulation is assessed in terms of its ability to reproduce the eddy states in the SCS. Sections 4.3, 4.4 and 4.5 focus on the statistical characteristics and the variabilities on different time scales. In addition, the relationship between the variability and El Niño is briefly discussed. Section 4.6 provides a summary of our work and describes options for constructing empirical downscaling models for the eddy activity in the SCS.

4.2 STORM Validation to detect the eddies

In this section, I compare the STORM simulation results with the eddy characteristics from the AVISO gridded data set based on Chen et al. (2011). Therefore, the same criteria for detecting potential eddies are used as those in Chen et al.'s work. The main results on the long-term statistics of eddies in the SCS uses a different set of parameters (see section 2.2) because it focuses on investigating the statistics of eddies of all sizes, and a limitation on the absolute intensity will cause small eddies to be removed.

To assess whether the STORM simulation can reproduce the eddy activity in the SCS, I derived the minima and maxima in the SSHA fields with intensity >=3 cm and diameter d >=35 km (Chen et al., 2011) from STORM and AVISO during the period 1993-2010. These minima and maxima may be parts of a migrating eddy, but in the AVISO data, they represent observational noise. For an accurate comparison, the 0.1-degree STORM results in this section were interpolated onto the same grids as the 0.25-degree AVISO data.

Figures 4.1a and 4.1b show the frequency of the occurrences of these minima and maxima at all grid points. Both data sets show that the potential eddy centers occur most frequently in the Luzon Strait. The region with high occurrence frequencies extends westward from the Luzon Strait along the continental shelf, past southeast China and to the Vietnam coast. In addition to these regions, several small areas with high occurrence frequencies are scattered in the central and northern parts of the SCS.

It is notable that substantially more potential eddies are identified in the AVISO data than in the STORM simulation. However, errors with magnitudes of 1 cm and greater prevail in the AVISO data set (AVISO, 2015), so it is plausible that given the minimum intensity of 3 cm and a RMS error of 1 cm and more, some of the minima may be artifacts generated by the observational and gridding procedures. These artifacts are assumed to be short-lived and to not travel consistently in space. Therefore, I focus the comparison on the sequences of minima and maxima that form tracks.

It may be worthwhile to examine these cases of short-lived, nontravelling minima and maxima in the AVISO data set, but this would be beyond the framework of this study.

Eddy propagation speeds are similar to the phase speed of long baroclinic Rossby waves (Faghmous et al., 2015) and are expected to be less than 30 cm/s. Thus, an eddy cannot travel farther than 30-40 km in one day. Given the coarse resolution of the AVISO data, I use 40 km as the maximum daily travel distance; however, when deriving the statistics of eddy migration for the STORM results, which have a higher grid resolution, I use 25 km (sections 4.3 to4.5). The maximum daily travel distance of 40 km is different from the 150 km used by Chen et al. (2011) with 7-day interval data (approximately 21.4 km per day). Therefore, for the filtering step, there is no need to use the same filtering criteria as in Chen et al. (2011). Thus, I use the filters in section 2.2. After this connection and filtering process, many potential eddies in the AVISO data disappear, the patterns in the AVISO and STORM data match better, and the differences are weaker (Figures 4.1c and 4.1d).

The general pattern (Figure 4.1b) is consistent with the eddy probability derived from the 7-day interval AVISO data shown in Chen et al. (2011), but their regions with high frequency of occurrence are connected, larger and concentrated. They obtained the eddy probability at each point by determining the time when the grid was covered by a vortex, which is different from my results that only used the time that a grid point is occupied by a minimum or maximum in SSHA. A vortex can cover many grid points, but an eddy center is located at only one grid point.

In addition, it is worth noting, but is often ignored in previous research, that the mesoscale resolution capability of altimeter missions is quite limited. Dufau et al. (2016)

provided global spatial distributions of altimeter error levels for the recent Cryosat-2 and Jason-2 missions and analyzed the minimum dynamic structures that the altimeter would be able to statistically observe. Depending on the changes in the noise error with time, the 1-D mesoscale resolution capability changes temporally and spatially. The noise level of Jason-2 ranges from 1.5 to 2.25 cm RMS when the significant wave height varies from 2 to 7m.

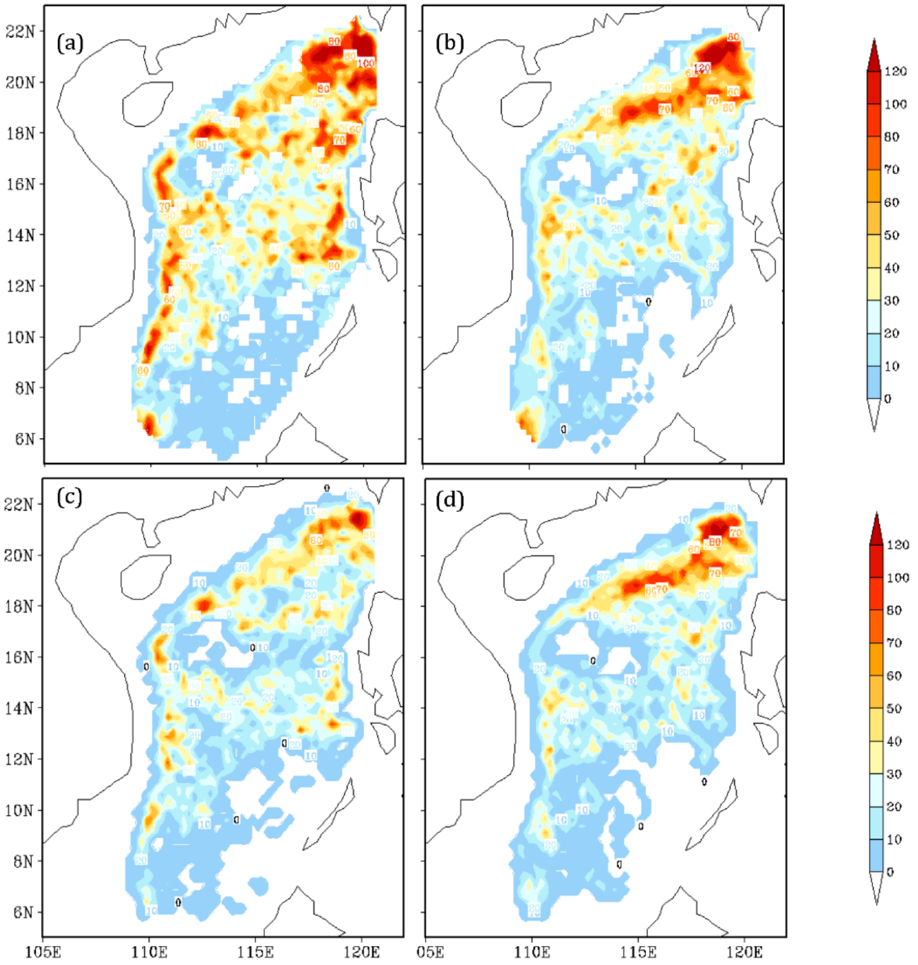

Figure 4. 1 Comparison of the STORM results with the AVISO data. The frequency of eddy centers in each grid box during 1993-2010 from AVISO (a) and coarsened STORM (b); (c) and (d) are the same as (a) and (b) but after eddy connecting and filtering. Note the differences with Figure 4.2, which used the full resolution STORM results.

Amores et al. (2018) analyzed the extent that the gridded altimeter products can characterize ocean eddies. Their results suggested that the gridded altimeter data set underestimated the eddy density and overestimated the amplitudes. The data set can capture less than 16% of the eddies, and the limited spatial resolution of the products is attributed to the underestimation. However, no better observations for deriving eddies and assessing the accuracy of the STORM data are currently available.

4.3 Climatological characteristics

During the period 1950-2010, a total of 62,317 anticyclonic eddy points (maxima along a track) and 115,133 cyclonic eddy points (minima along a track) were detected in the STORM daily data, corresponding to 1709 AE tracks (AEs; 28.0 per year) and 3331 CE tracks (CEs; 54.6 per year).

The index "IN" is defined to measure the relative proportion of CEs to AEs and is given by:

$$IN = \frac{N_{CE} - N_{AE}}{N_{CE} + N_{AE}}$$

where N_{CE} and N_{AE} represent the numbers of CEs and AEs, respectively. The IN index can vary between -1 and 1, with 0 indicating that the same numbers of AEs and CEs were generated. IN=1 (-1) indicates that no AEs (CEs) were generated. The monthly IN has an average value of 0.29 and a skewness of -0.67. The negative skewness indicates that the median is larger than the expectation of 0.29; the number of CEs is more than 1.8 times greater than the number of AEs in most months.

The combined effect of the enhanced spatial and temporal resolutions of the STORM data, together with the relatively moderate sizes and intensity criteria, lead to many more eddies in our results than when using 7-day interval (or daily) and 0.25 degree AVISO data (Chen et al., 2011; Xiu et al., 2010; see Section 4.2). Many fewer AEs are detected than CEs.

This is related to the difference in the eddy size distribution between the two kinds of eddies and will be discussed later in the section on the eddy diameter (ED) distribution.

Figure 4.2 presents the spatial distribution of the frequencies that an eddy center passes each grid box during 1950-2010. Most of the eddy centers occur in the northern SCS. Note the difference with Figure 4.1d, where the analysis was performed with coarsened data to allow for an accurate comparison with the AVISO data. In addition, Figure 4.1d only considers the years 1993-2010.

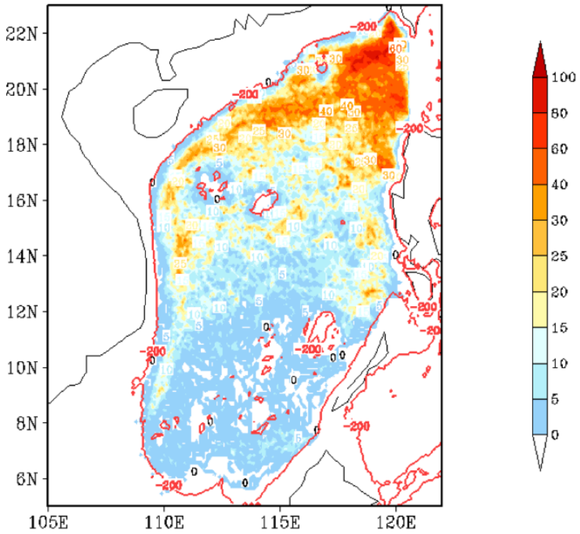

Figure 4. 2 The frequency of occurrence of eddy centers in each grid box during 1950-2010. Note the difference with Figure 4.1, which used coarse resolution STORM results to allow for an accurate comparison with the AVISO data.

The regions with the highest frequencies are located near the Luzon Strait and extend southwestward to the Vietnam coast along the continental slope, which correspond to the strong western boundary currents in the northern SCS (e.g., Zhang and von Storch, 2017). Frontal instability due to the Kuroshio intrusion and wind stress curl are the major factors that generate eddies near the Luzon Strait and offshore of the Vietnam coast. Based on the westward propagation characteristics of the eddies in the northern SCS, the high occurrence frequency along the continental slope might be due to the eddy moving from the Luzon Strait.

The maximum frequency along the Vietnam coast is not as high as that from the AVISO 7-day interval data in Chen et al. (2011). This difference may occur because our algorithm filters stationary eddies, so a stationary pair of an AE and a CE off the Vietnam coast associated with the coastal wind jet (Chu et al., 2017; Lin et al., 2017) is not counted in our analysis.

To describe the distributions of the eddy travel distances and eddy lifespans, probability density functions of the eddy length and lifespan were calculated (Figure 4.3). In this time period, the AEs traveled a maximum of 1941 km with an average travel distance of 292 km, and CEs traveled a maximum of 1988 km with a mean distance of 274 km. The eddy lifespans ranged from 6 days to 240 days for the AEs and from 6 days to 293 days for the CEs with mean lifespans of 36.5 days and 34.6 days, respectively. The distance and lifespan distributions of the AEs and CEs do not differ much, but the ranges of the distances and lifespans of the CEs are wider than those of the AEs.

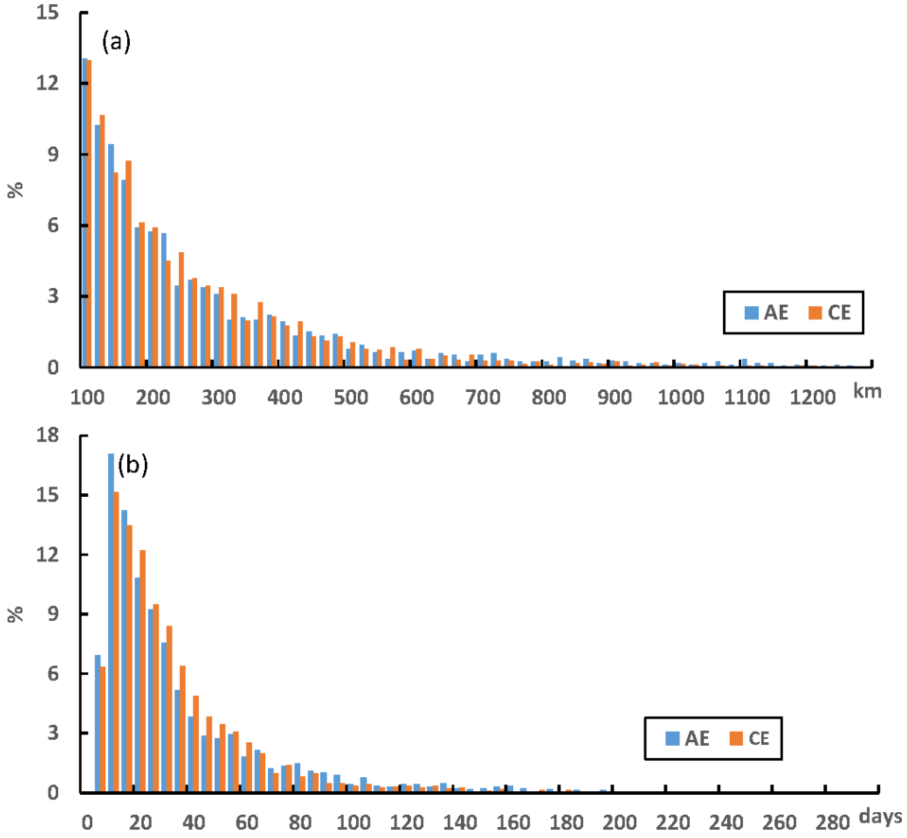

Figure 4. 3 Probability density functions of the eddy travel distance (a) and eddy lifespan distribution (b).

The distributions of the eddy intensities (EIs) and eddy diameters (EDs) of the peak points (i.e., the eddy points with the highest EI along an eddy track) were investigated. The highest intensities range from 0.55 cm to 37.3 cm with maxima of 3-4 cm for the AEs and 2-3 cm for the CEs (Figure 4.4a). Our eddy detection and tracking algorithm removed the eddy tracks in which the highest RI_{max} <6 mm. Many weak eddies with EI <1 cm were deleted; thus, the frequency of 0-1 cm eddies is low. If all of the eddy points are considered (Figure 4.5a), the EI values vary from 0.11 cm to 37.3 cm with mean EIs of 6.2 cm for AEs and 4.9 cm for

CEs. AE points tend to occupy higher percentages of eddies with EI >6 cm than CE points. More than 40% of the AE points and fewer than 30% of the CE points have EI >6 cm.

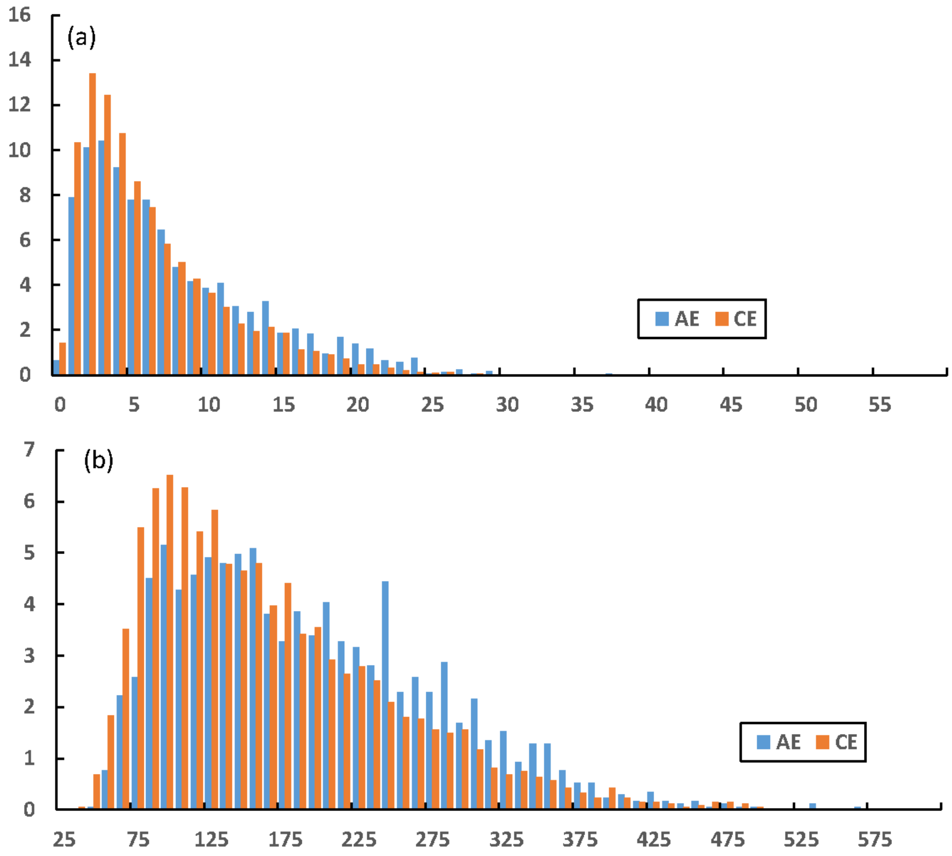

Figure 4. 4 Probability density functions of the eddy intensities of the peak eddy points with an interval of 1 cm (a; starting at 0.0 cm) and of the eddy diameters of the peak eddy points with an interval of 10 km (b; starting at 25 km).

The corresponding diameters at the strongest eddy points range from 43 to 631 km (Figure 4.4b). The most common EDs of the peak eddy points are 95-105 km. No eddy peaks are associated with diameters less than 35 km, which is related to the size limitation of 5 pixels. Many of the peak CE points (more than 41%) and more than 29% of the AEs have EDs less than 135 km. The opposite situation occurs with the peak AEs; 13% more peak AEs than peak CEs have EDs greater than 205 km.

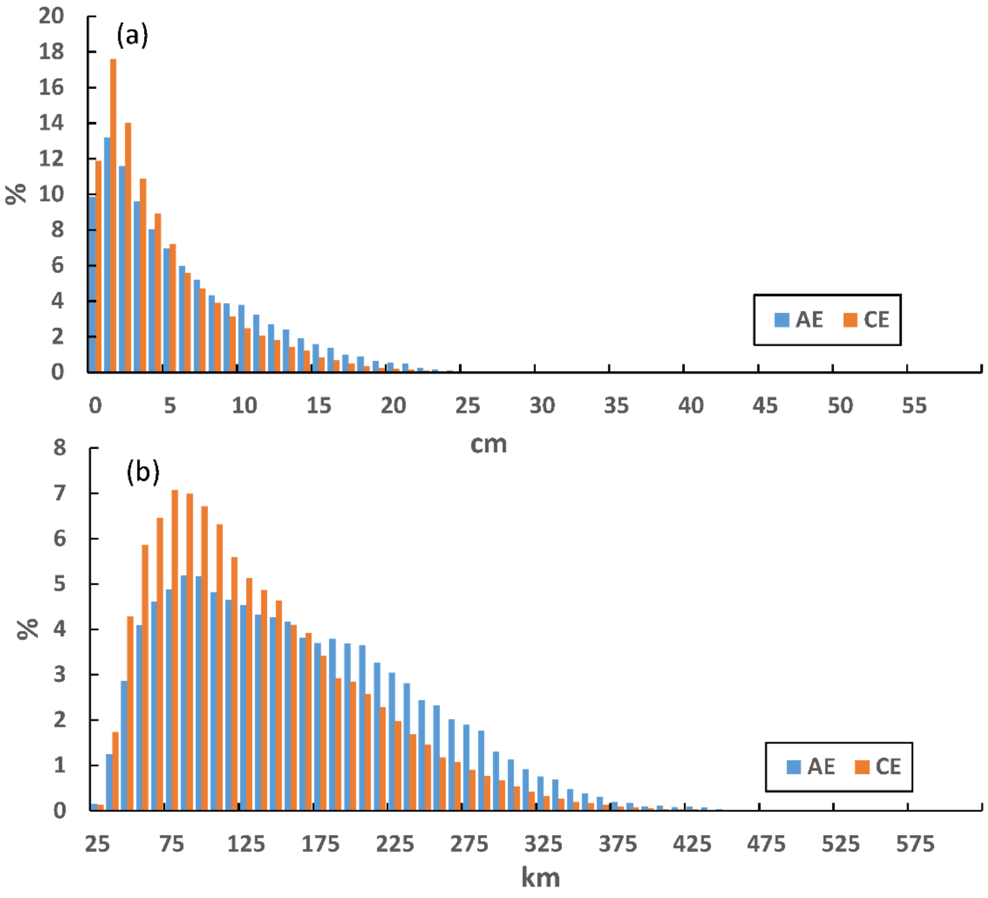

Figure 4. 5 Probability density functions of the eddy intensities of all eddy points with an interval of 1 cm (a; starting at 0.0 cm) and of the eddy diameters of the peak eddy points with an interval of 10 km (b; starting at 25 km).

If all eddy points are considered (Figure 4.5), the diameters vary from 30 km to 572 km for the AEs and from 30 km to 633 km for the CEs. The percentage of large AE eddies is greater than that of the CEs; 41.3% of the AEs have diameters greater than 175 km, whereas only 26.2% of the CEs are more than 175 km in diameter. Many more CEs have small sizes than AEs.

The large difference between the numbers of detected AEs and CEs could be attributed to the larger number of small active CEs. Our algorithm and the STORM simulation keep many more small eddies than in previous studies, and more small eddies are CEs than AEs.

The climatological analysis indicates the presence of more active CEs, with a larger range but smaller mean values of EI and ED, which indicates that a greater percentage of AEs are larger and have higher intensities.

4.4 Dominant spatial patterns

Empirical orthogonal functions (EOFs) are a convenient and commonly used tool to identify dominant spatial patterns of variability. I used this approach to study the annual number of eddies (EN), mean annual intensities (EI) and mean annual diameters (ED) of the anticyclonic eddies and the cyclonic eddies. Our data fields X consist of 61 time “points” and 27,271 spatial “sea points” in the SCS. It is not possible to calculate the eigenvalues of X’X because of the sheer size of the matrix, but the matrix XX’ has the same nonzero eigenvalues (von Storch and Hannoschöck, 1984), and the eigenvectors are related through X. Because XX’ is much smaller than X’X, I solve the eigenproblem of the smaller matrix without encountering numerical problems.

Only the eddy center is considered. The original spatial blocks for the eddy parameters are the same as the STORM SSHA fields (i.e., 0.1-degree cells). In addition, two other data sets are formed by binning these data into larger spatial blocks (i.e., 1-degree and 2-degree cells).

Figures 4.6 –4.11 show the EOF results of the three major eddy properties (ED, EI and EN). AEs and CEs are analyzed separately. In all six figures, (a) is from the eddy property fields at the 0.1-degree cells, and (b) and (c) are from the fields with 1-degree and 2-degree cells, respectively. The 0.1-degree fields do not show robust structures in the first EOF, and the explained variance is very low (approximately 2%-6% in the six analyses). Their eigenvalues have a similar distribution to what would be expected from a white noise analysis using an estimate of the error in estimating eigenvalues following Lawley (1956).

This is a relatively rare case; in most cases, at least the estimated eigenvalue of the first EOF is separated from the other estimated eigenvalues, so only the tail of the eigenvalues, which sometimes begins at the second eigenvalue but usually at higher-index eigenvalues, is consistent with a white eigenvalue spectrum and with arbitrary eigenvectors.

The first EOF is shown in Figure 4.6a. The pattern is quite fragmented; a pattern can hardly be recognized. The next eigenvectors exhibit similar random textures.

However, when the spatial field with the original 0.1-degree resolution is coarsened by binning into 1-degree boxes, the situation improves. The spectrum of eigenvalues is shown in Figure 4.6e as a red curve. The difference between the first two eigenvalues is approximately the same as the estimated error of the first eigenvalue, so the first two eigenvalues are separated, whereas the tail, beginning with the third eigenvalue, is consistent with a white noise spectrum. In addition, as shown in Figure 4.6b, the pattern begins to have a structure. However, the percentages of variance represented by the first two eigenvalues are only 8 and 6 percent, respectively. Thus, in contrast to most EOF analyses, the identified patterns do not describe a relevant part of the overall variability.

Even after coarsening to a 1-degree grid, the variability in the seasonal mean diameters of the cyclonic eddies in the SCS reflects little variation in the large-scale conditions, such as currents or wind systems. Similar results are obtained for the seasonal eddy intensities and numbers of both cyclonic and anticyclonic eddies.

An even stronger coarsening was done to a 2-degree grid. The spectrum, which is shown in blue in Figure 4.6e, is slightly steeper, and the first two EOFs represent approximately 25% of the overall variance. In addition, the third eigenvalue might be slightly more robust.

Interestingly, the principal components (i.e., the time coefficients) of the EOFs derived on the three different grids are positively correlated. The correlation of the very noisy EOFs on the 0.1-degree grid with those on the 1-degree grid is only 0.44, whereas for the 2-degree grid, it is only 0.32. The correlation between the PCs derived on the 1-degree grid and the 2-degree grid is 0.78. Thus, even though the EOFs on the finest grid must be considered mostly useless because of noise contamination, they only slightly represent the signal found on the coarsened grids.

Similar results hold for the EI and EN and the properties of the AEs (Figure 4.7-Figure 4.11). The AE patterns are limited to the central and northern parts of the SCS, reflecting the absence of AEs in the southern SCS. The first EOF of the ED describes a general enlarging or shrinking of eddies, whereas the intensity and number are summarized by dipoles favoring either the southern or northern parts of the Luzon Strait's throughflow.

Thus, in the spirit of empirical downscaling, any identification of spatially disaggregated distributions of eddy parameters can be used to link the eddy variability to large-scale patterns of features, such as regional wind, barotropic stream functions, vertical shear currents or vertical stability. However, this will be addressed in more detail in a subsequent paper. I hypothesize that the internal variability, unprovoked by changes in the large-scale conditions – and thus is "noise" in the spirit of Tang et al. (2019) - is a significant factor for the variations in eddy activity. Of course, for verifying the hypothesis, more analyses are needed.

Because the spatial distributions of the eddy parameters may not have dominant modes, they may not be suitable as predictands. For the analysis presented in Chapter 5, which is related to the linkage between large-scale phenomena and the eddy activity in the SCS, I will use the area-mean properties as predictands instead of the spatial distribution.

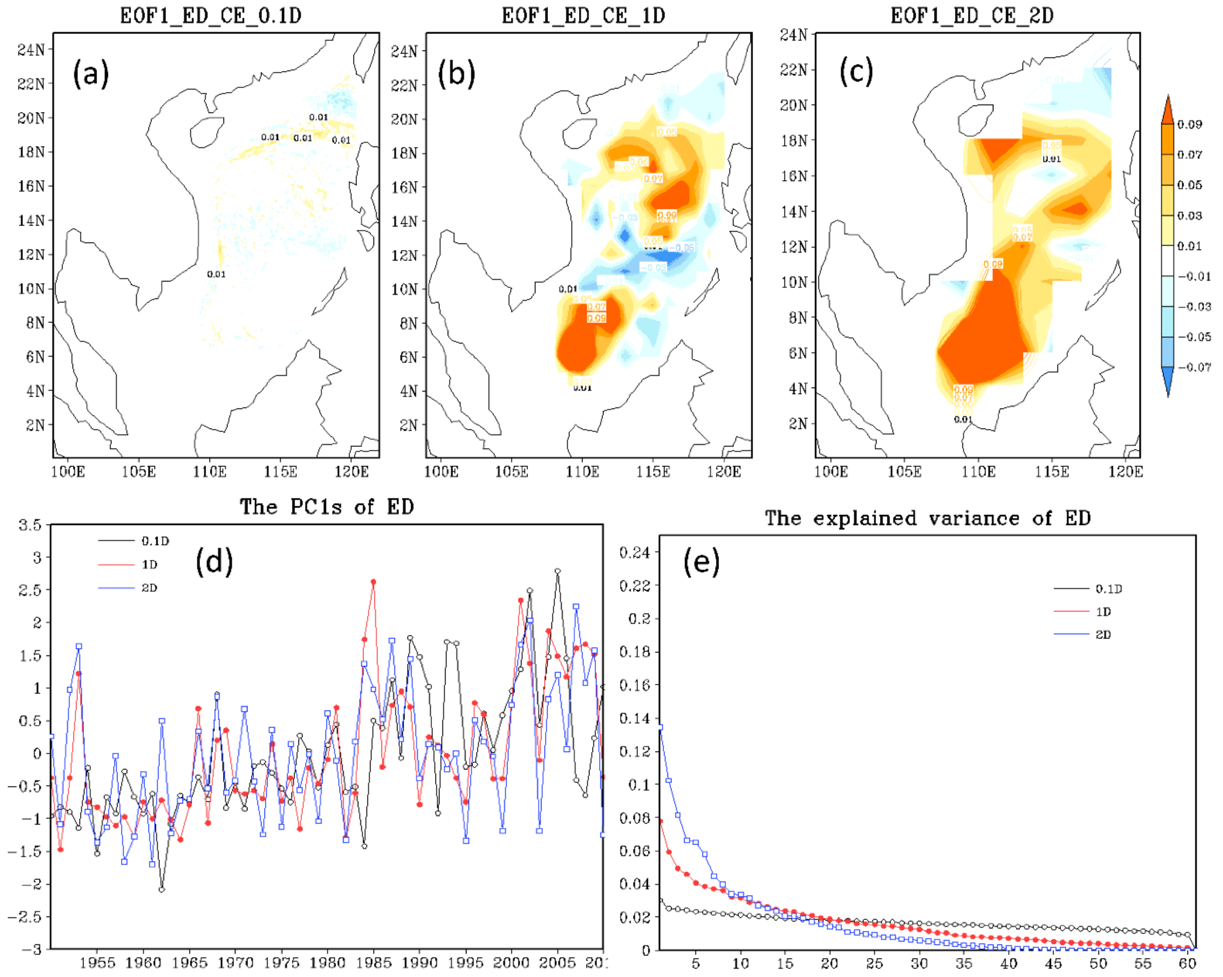

Figure 4. 6 The first EOFs ((a)-(c)), the corresponding PCs (d) and the explained variances of the ED distributions of the CEs. (a) is the first EOF from the original ED distribution fields in the 0.1-degree grid boxes. (b) and (c) are similar to (a) but are from the fields binned into 1-degree and 2-degree grid boxes, respectively.

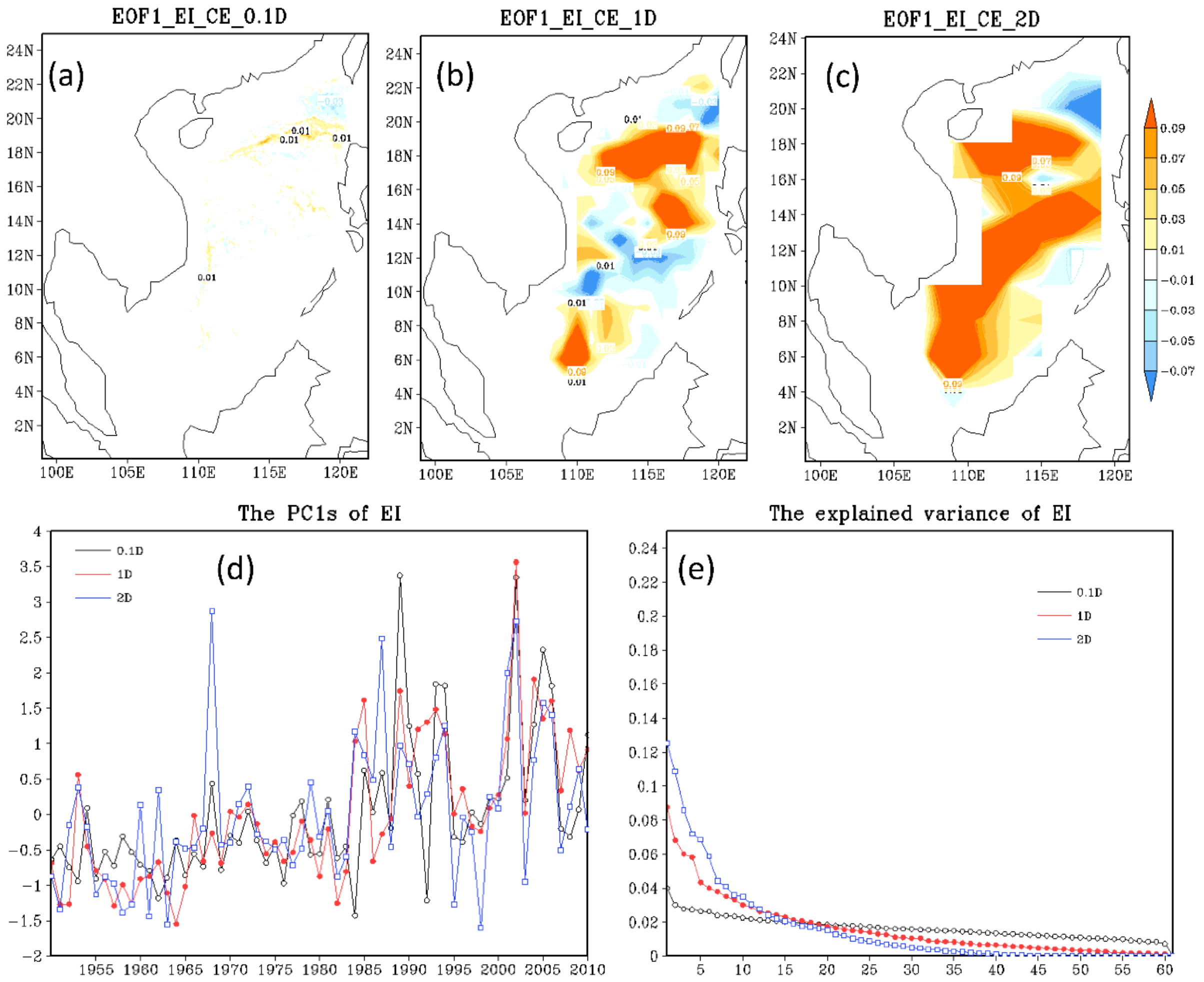

Figure 4. 7 The same with figure 4.6, but for eddy intensity of CEs.

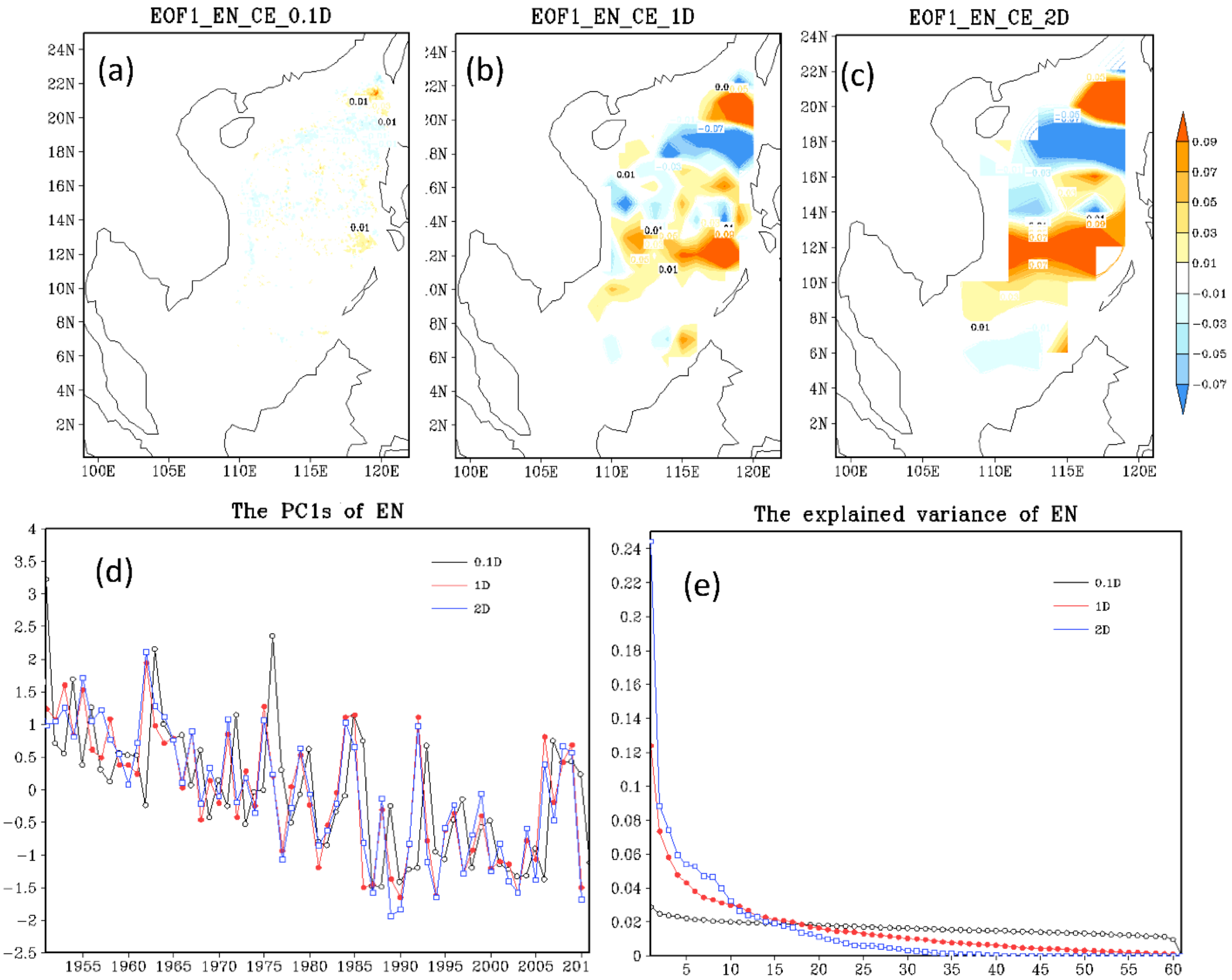

Figure 4. 8 The same with figure 4.6, but for number of CEs.

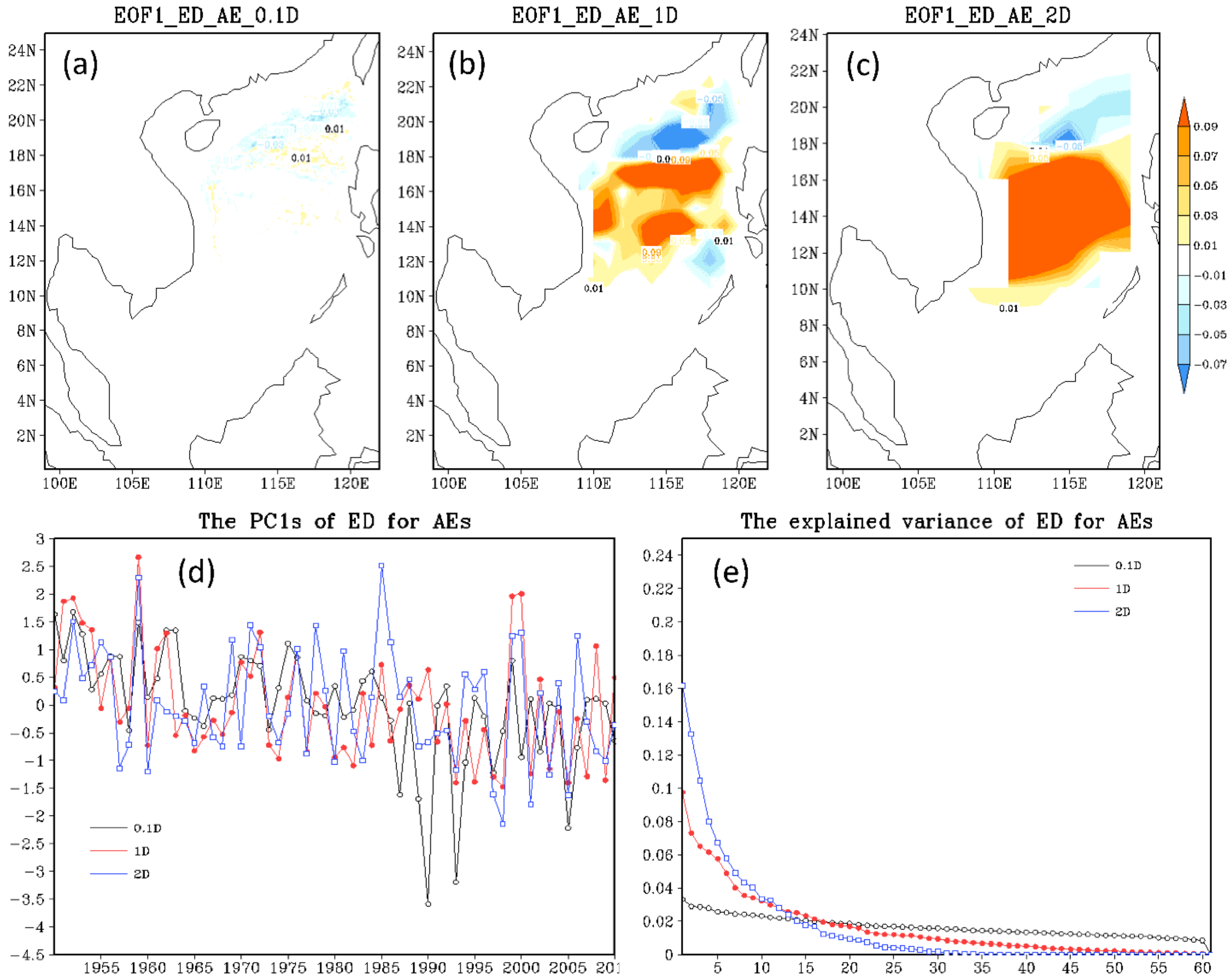

Figure 4. 9 The same with figure 4.6, but for eddy diameter of AEs

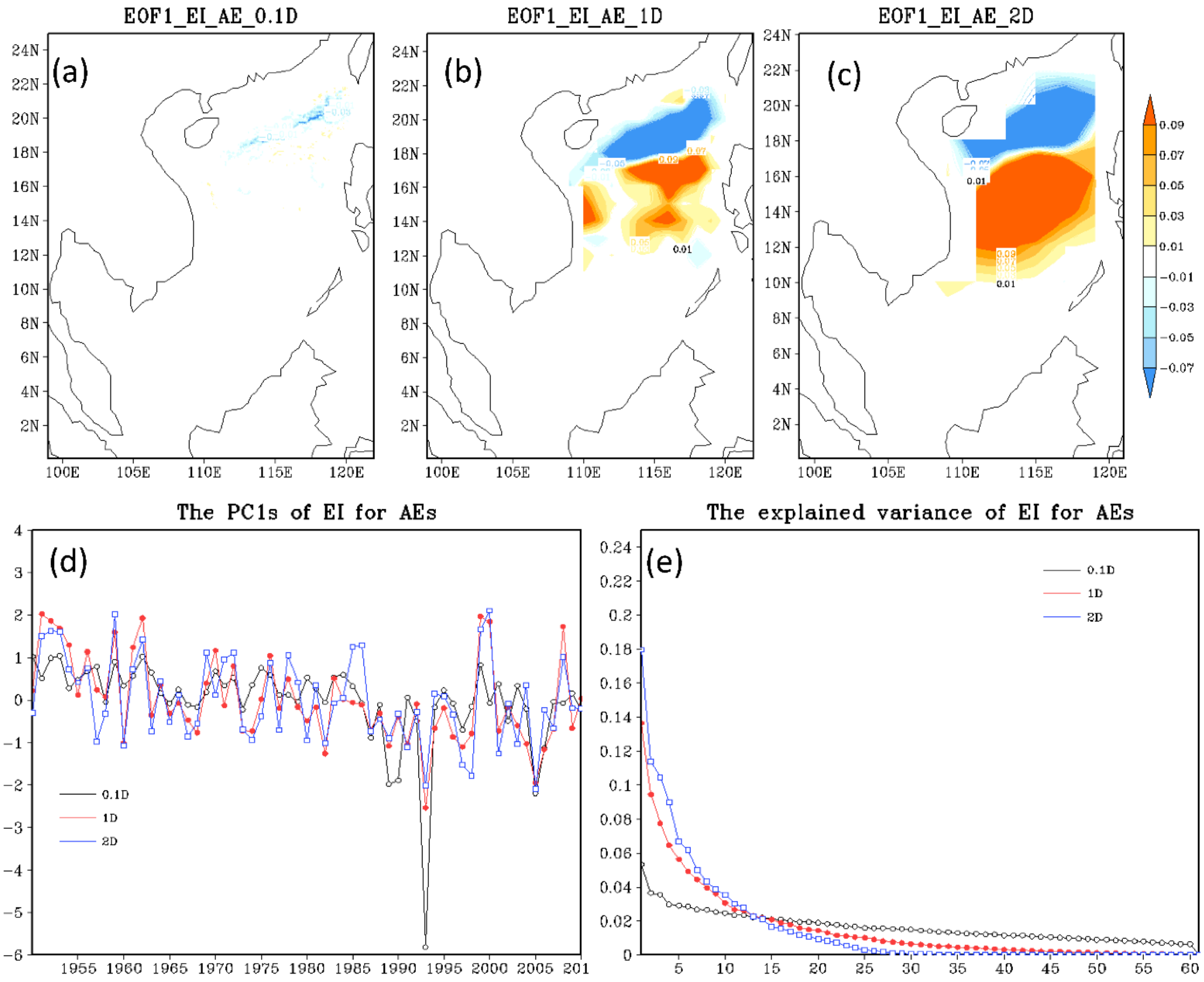

Figure 4. 10 The same with figure 4.9, but for eddy intensity of AEs.

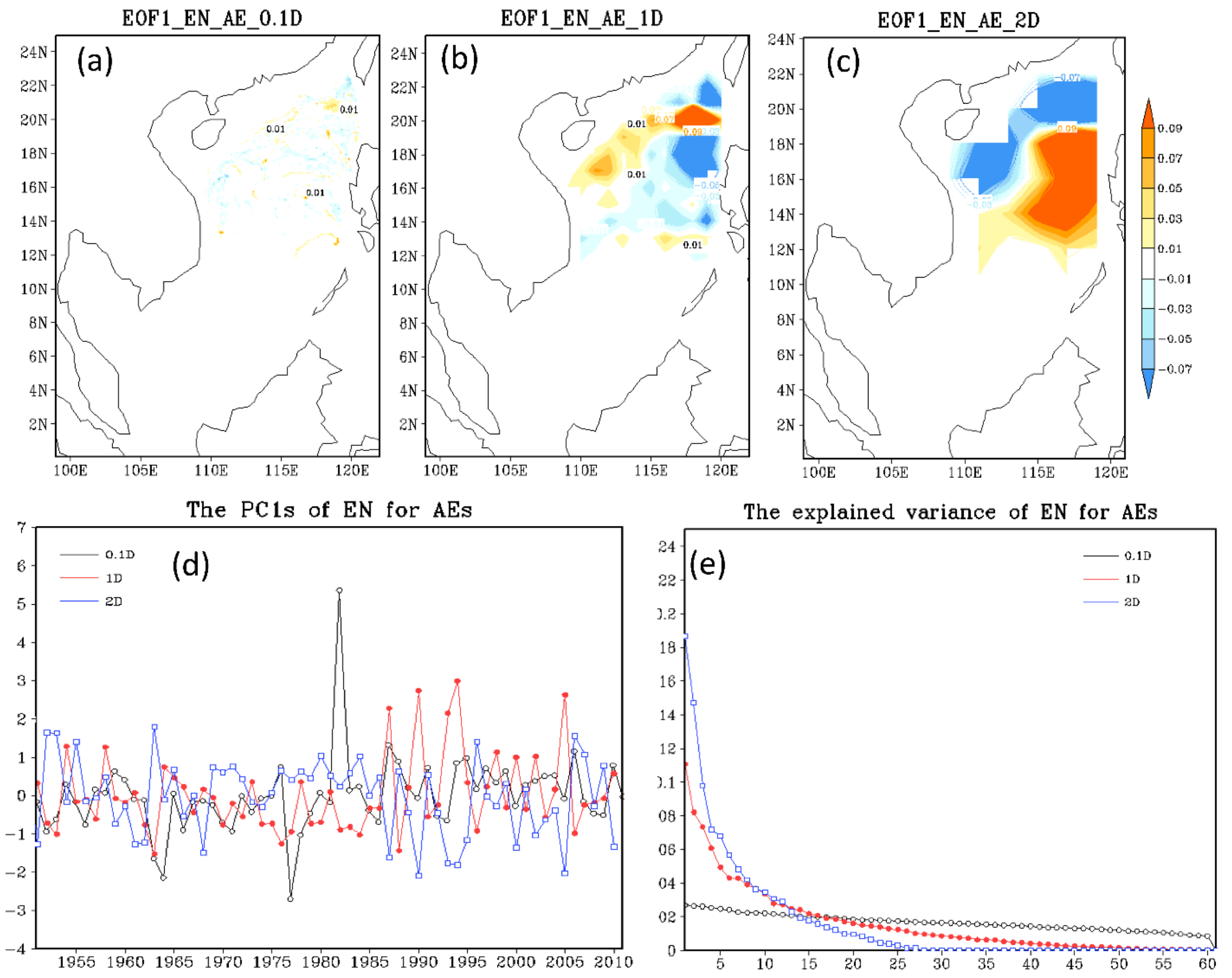

Figure 4. 11 The same with figure 4.9, but for number of AEs.

4.5 Variability of eddy properties

In this section, temporal variability at different time scale of eddy properties is discussed in detail.

4.5.1 Seasonal variability

More CEs are generated than AEs in all the 12 months (Figure 4.12a). The number of eddies generated in each month exhibits a significant seasonal variation. Most CEs are generated in the winter half year, with a peak of 364 eddies in March. More AEs are formed in the spring than in the autumn. The minimum number of eddies generated is only 105 in September.

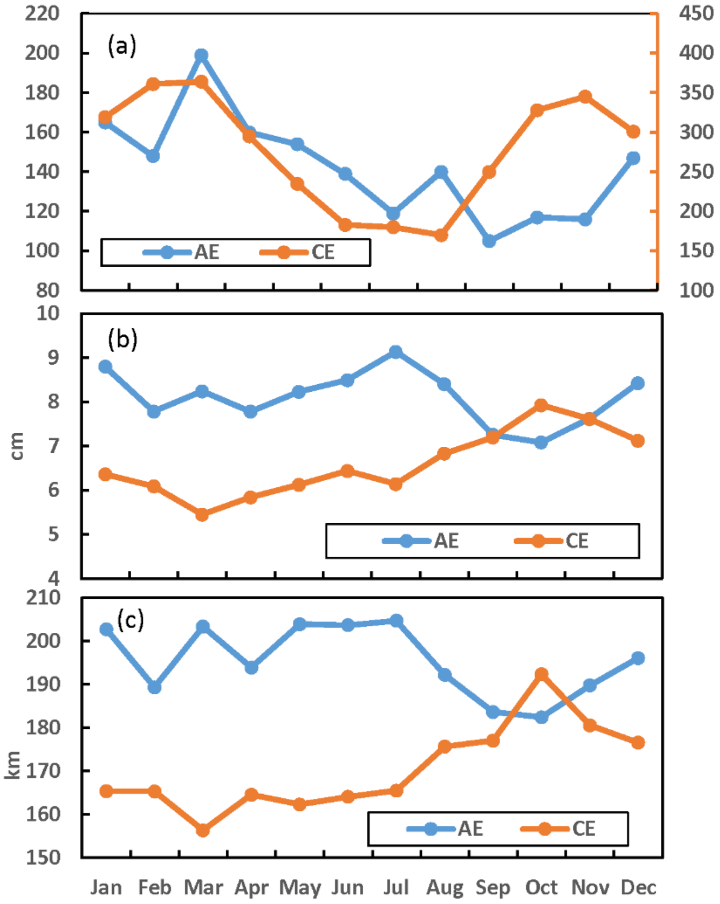

Figure 4. 12 The annual cycle of the multiyear-sum number of eddy tracks (a) and the means of EI (b) and ED (c) of the peak eddy points. The axis on the left is for AEs, and the axis on the right is for CEs.

For all 1709 AEs and 3331 CEs, the EIs and EDs of the peak eddy points are determined. The monthly means of EI and ED (Figure 4.12b, c) exhibit different variations. AEs always have stronger intensities and larger sizes than CEs. In addition, the monthly EI and ED data reveal an annual cycle, peaking in July with EI=9.14 cm and ED=205 km for AEs, while these values peak in October for CEs with EI=7.93 cm and ED=192 km. From July to October, the ED and EI values of peak AEs decline sharply, from the maxima hitting the minima. On the contrary, rapid growth occur in both the ED and EI variability of CEs and increase to the maxima during these four months. In terms of the monthly means of all 62317 AE points and 115133 CE points, an annual cycle is also apparent (Figure 4.13), AEs peak in August, with EI=7.01 cm and ED=174 km. CEs reach peaks in November when EI=5.58 cm and ED=147 km.

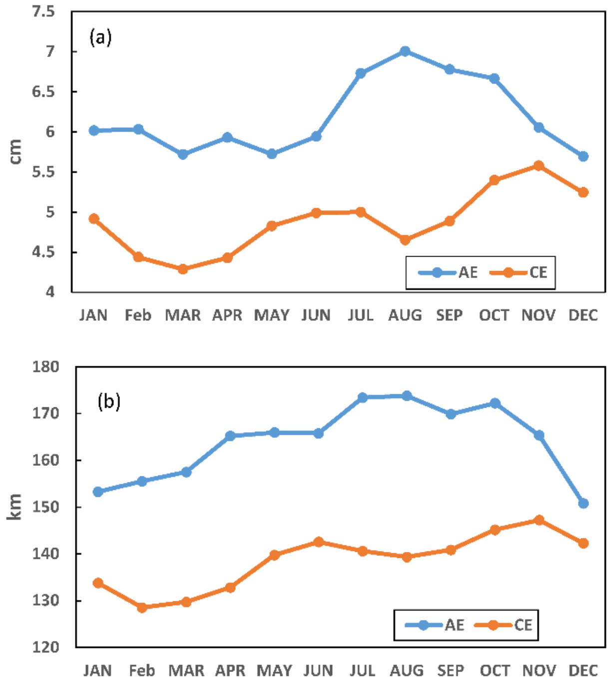

Figure 4. 13 The annual cycle of the means of EI (a) and ED (b) of all eddy points. The axis on the left is for AEs, and the axis on the right is for CEs.

4.5.2 Interannual variability

To assess the long-term variability of the eddy properties, the annual time series of generated eddies, EIs and EDs have been plotted (Figure 4.14). Interannual variability dominates the annual series of eddy number. There is some decadal variability with maxima in the 2000s and 1970s, and minima in the 1980s and 1950s.

To evaluate the influence of the RI threshold set in the eddy detecting algorithm, I conducted a comparative analysis with increased values of RI=6 mm and RI_{max}=10 mm instead of the standard set of RI=3 mm and RI_{max}=6 mm. The result is shown in Figure 7b. The variability of the revised series is similar to the original series, with correlation coefficients of 0.82 and 0.80 for AEs and CEs, respectively. Additionally, both figures present much more CEs than AEs. It can be concluded that the selected threshold has little effect on the variability of the number of eddy tracks.

Xiu et al. (2010) published the annual number of generated eddies derived from AVISO satellite data and their own modeled data during 1993-2007 by using the W-based eddy detection and tracking method. Figure 8c combines our results from STORM and their results to further assess our results. Due to their strict criteria for eddy size, water depth and so on, the number of eddy tracks identified in their study is less than ours. In terms of variability, STORM outperforms Xiu et al.'s simulation when compared with the AVISO satellite data. The correlation coefficient of the annual number of eddies during 1993-2007 between AVISO and STORM is 0.21, which is much higher than the correlation coefficient of 0.03 between AVISO and Xiu et al.'s simulation. This comparison suggests that STORM simulation describes more realistic variability of the travelling eddies in the SCS, which should benefit from the realistic reproduction of the SCS dynamics (Zhang and H. von Storch, 2017).

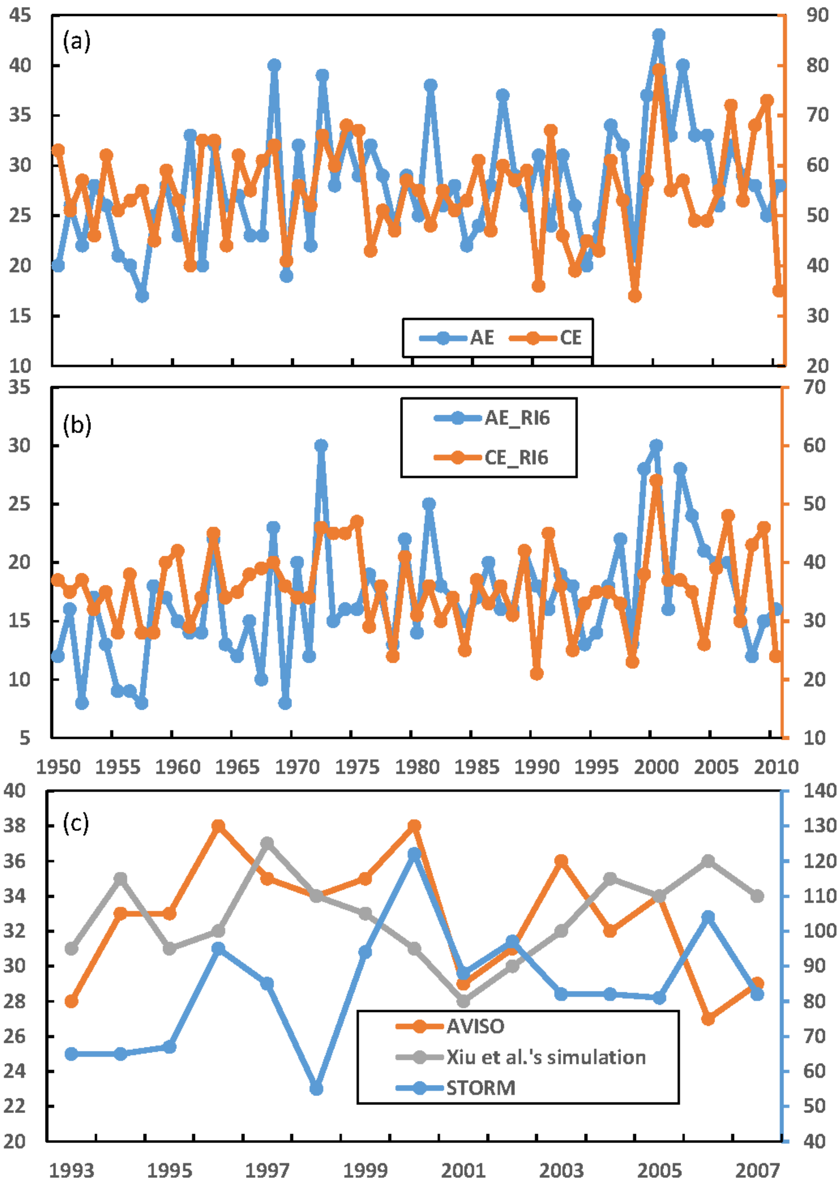

Figure 4. 14 The annual number of eddy tracks. (a): Number found in STORM using the standard setup of RI=3 mm and RI_{max}=6 mm. The axis on the left is for AEs, and that on the right is for CEs. The axis on the left (right) is for AEs (CEs). (b): Same, but with RI=6 mm and RI_{max}=10 mm. The axis on the left (right) is for AEs (CEs). (c): Series according to STORM with a standard set-up, AVISO satellite data (Xiu et al., 2010) and the simulation by Xiu et al. (2010). The axis for the STORM result is on the right.

With regard to the annual mean EI and ED values of the peak eddy points (Figure 4.15), the annual series also presents mostly interannual variability with very little decadal variability and no trends. AEs on average have higher EIs and larger EDs than CEs in each year (except several years), which is consistent with the climatological results. In section 5.1, the skewness analysis and the eddy property distribution reveal much more CEs with small size and low intensity than such AEs exist in the SCS. This feature of the eddies in the SCS may be related to the different generation mechanisms of AEs and CEs.

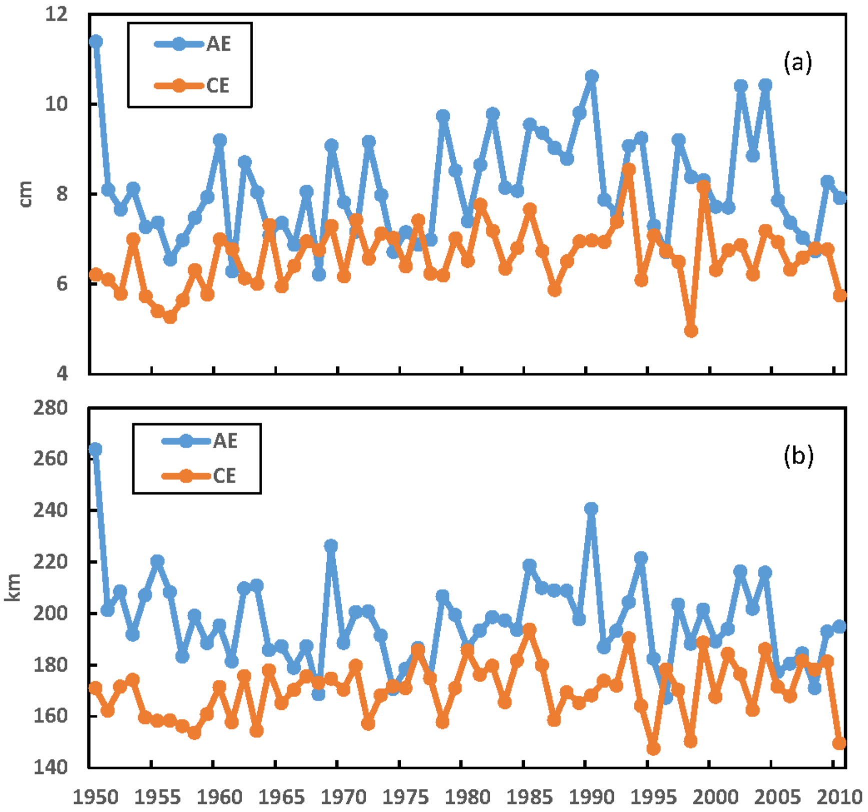

Figure 4. 15 The annual time series of EIs (a) and EDs (b) of peak eddy points.

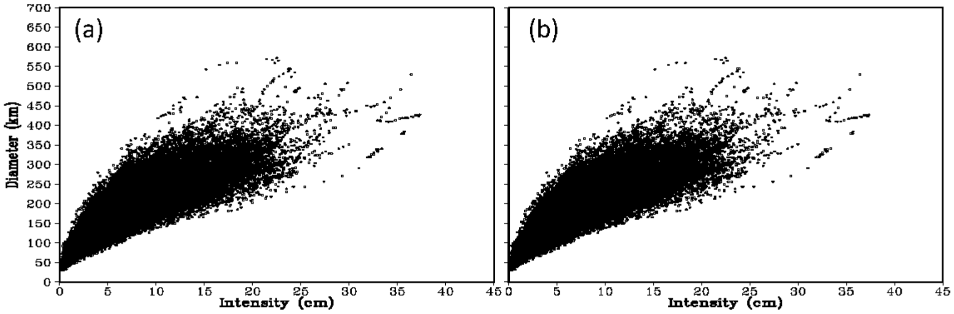

Figure 4. 16 The scatter diagram between eddy diameter and eddy intensity of AEs (a) and CEs (b) derived for all points along all eddy tracks.

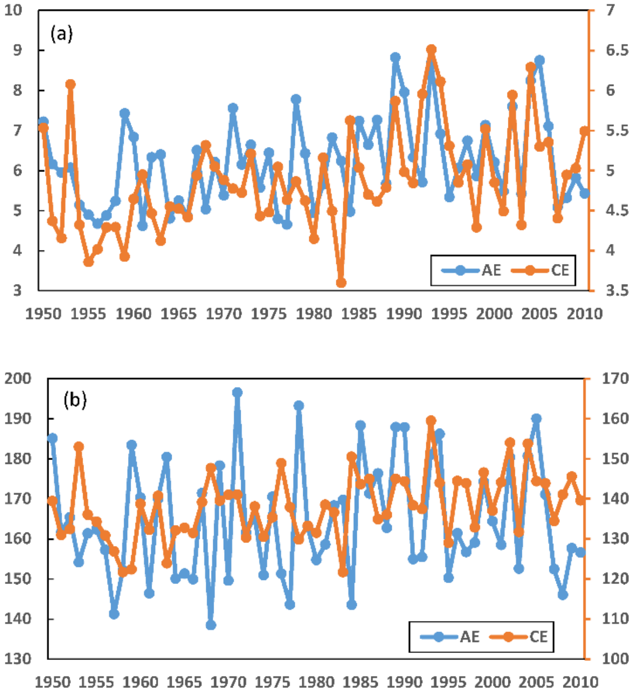

Figure 4. 17 The annual time series of EIs (a) and EDs (b) of all eddy points.

The AEs vary more strongly than the CEs. The annual mean EDs and EIs are strongly correlated, with correlation coefficients of 0.76 and 0.68 for AEs and CEs, respectively. Thus, strong eddies tend to be large, as is illustrated by the scatter diagrams of the two parameters (Figure 4.16). The annual mean EDs and EIs of all eddy points (Figure 4.17) show similar features, with EI-ED correlation coefficients of 0.88 and 0.78 for AEs and CEs, respectively.

El Niño is one of the most important phenomena in the tropical ocean. For the SCS, El Niño is considered significant because of its impact on the wind stress curl over the SCS and the ocean circulation in the SCS (Fang et al., 2006, Y. Wang et al. 2006). In addition, with regard to the annual time series of eddy number and EI when considering all eddy points, a simultaneous drop is observed during the strong El Niño year of 1998.

However, when the El Niño3.4-index (https://www.esrl.noaa.gov/psd/data/climateindices/list/for info) is correlated with the number of generated eddies and the eddy parameters of all eddy points on a monthly basis, I find very small correlations, which seem to be irrelevant – see Table 4.1.

To take into account the effect of serial correlations (Zwiers and von Storch, 1995), I assume that no more than 12 month time difference are needed to have independent sample. Using this “efficient sample size”, none of the links were significant.

It can be concluded that a relevant link to the ENSO dynamics on the tropical Pacific does not exist for the formation of eddies in the SCS.

Table 4. 1. The correlation coefficients between El Niño3.4 index and the eddy properties.

El Niño3.4-index vs	Genesis number (EN)	Intensity (EI)	Diameter (ED)
AEs	0.09	0.09	0.08
CEs	-0.11	-0.04	0.04

4.6 Conclusion

In this work, the long-term variability and statistical features of the travelling eddies in the SCS during the period 1950-2010 were investigated using the high-resolution and multidecadal output from the ocean global model simulation STORM, which was forced by 6-hourly NCEP atmospheric reanalysis. The STORM simulation has an average horizontal resolution of 10 km, which enables it to resolve eddies in the SCS.

To derive the eddy activity from the STORM SSHA data, the M-based eddy detection and tracking method, which makes use of the discrete SSHA fields, was developed. This algorithm avoids the problems from the calculations of differential and integral operators. In addition, eddies are identified as the moving extremes in space and time. Stationary eddies are not considered in this study.

On average, 28.0 AEs and 54.6 CEs per year are found in the STORM data in the SCS based on the criteria and the parameters in the M-based detection and tracking procedure. The tracks include 62,317 points for AEs and 115,133 points for CEs, which means that the average lifespan of the AEs is 36.5 days, and that of the CEs is 34.6 days. More CEs are detected than AEs. The lifespans of the eddies in the SCS range from 6 days to 293 days, and they travel up to 1988 km. The spatial distribution shows that the most common regions for eddy tracks to travel are the Luzon Strait and toward the continental slope to the Vietnam coast. Those eddy points have EI ranges of 0.11 cm to 37.3 cm and ED ranges of 30 km to 633 km, and the strongest eddy points along the eddy tracks have EI ranges of 0.55 cm to 37.3 cm and ED ranges of 43 km to 631 km. For both kinds of eddies, the stronger eddies tend to be larger.

No significant spatial patterns are found with the EOF analysis of the original 0.1° grid. Because the numerical solution is obtained from the eigenanalysis of the smaller (61 x 61) XX' covariance matrix instead of the much larger X'X-matrix, this strong contamination of the spatial covariability by internal small-scale dynamics is not an artifact of solving large numerical problems but is real, which is consistent with the results of Tang et al. (2019). The absence of significant patterns appears to be inconsistent with the hypothesis that the spatial distribution of eddy activity is substantially constrained by large-scale “drivers”, such as large-scale wind or current patterns. Instead, the formation of eddies is more an issue of internal variability and is largely unprovoked by external drivers. However, additional analysis and numerical experimentation are needed to obtain more robust results.

The STORM data suggest that the variability in the eddy properties in the SCS is dominated by seasonal variability. The number of eddies peaks in March, and the fewest eddies occur in September for AEs and in August for CEs. The peaks of the EI and ED of the peak eddy points occur in July for AEs and October for CEs. The interannual variability is strong, whereas the decadal variability is weak, and a long-term trend is not found. The variability in the eddy activity shows weak or no correlation with El Niño. I suggest that further work could analyze the influence of El Niño on the eddy activities in different regions of the SCS in detail because the eddy generation mechanisms differ in different parts of the SCS.

Satellite data (AVISO) of the sea surface height anomalies (SSHA) in the South China Sea are available beginning in 1993 and extend over a limited period. I used these data to determine if the STORM simulation data generate consistent numbers and characteristics of eddies in the SCS. Unfortunately, the accuracy of the local data in the gridded AVISO data set suffers from significant uncertainties on the order of 1 cm and more (Taburet et al., 2018); in addition, the spatial resolution of the AVISO data is less than that of the STORM results. This contributes to the differences between the AVISO and STORM data, but some of the differences may be due to insufficiencies in the model simulations. Unfortunately, I cannot quantify the different contributions. However, given the large uncertainty in the AVISO data, I identify a general consistency between AVISO and STORM. Unfortunately, these inaccuracies have not always been recognized in previous studies, which used only AVISO data to describe cases and statistics of eddies.

One purpose of this analysis was to prepare a data set that was suitable for the statistical downscaling of eddy properties. Future investigations should focus on the links between eddy activity and large-scale phenomena. Such links may allow the eddy activity in the coming decades to be projected.

5. The linkage between the variability of eddy properties and background flow

Chapter 4 presented the mean state and temporal variability in the eddy activity in the SCS during 1950-2010 based on the 0.1-degree STORM simulation. This chapter focuses on determining the extent to which large-scale drivers affect the variability in the eddy activity. If they have a good relationship, these large-scale drivers could be applied to construct the empirical downscaling model for projecting the future states of the eddy activity in the SCS using the coarse output of climate models.

5.1 Introduction

It is well accepted that eddies are induced by the instability of the background flow. The barotropic and baroclinic instabilities lead to the conversion of available potential energy to kinetic energy (Yang et al., 2017), which provides the essential energy for eddies to form and develop. Even though detailed mechanisms about eddy generation in the SCS have been determined, such as the wind stress (Chu et al., 2017), the interaction between strong flow and topography, and the Kuroshio, the background flow is often the link between these factors and the eddy activity.

For instance, Figure 5.1 illustrates how wind affects the eddy distribution through background flows. When the first PC of the surface current is positive, anomalous cyclonic currents occur in the southern SCS and anomalous flows go out through Luzon Strait. These anomalous flows are associated with anomalous southwestly wind. The anomalous wind curl over the southern SCS may results in such kind of anomalous currents. Furthermore, more eddies appear in the middle of the SCS and the western part of the Luzon Strait under these background current flow. The appearance of more eddies near Luzon Strait corresponds to anomalous cyclonic flows in the first EOF pattern of currents, which may transport vorticity to eddies. In the middle SCS, the instability related to the great anomalous horizontal shear of currents may be the reason for the occurrence of more eddies there.

The surface current affects the distribution of the number of eddies, and it is also influenced by wind. Therefore, the surface wind could affect the eddy activity through the background flow.

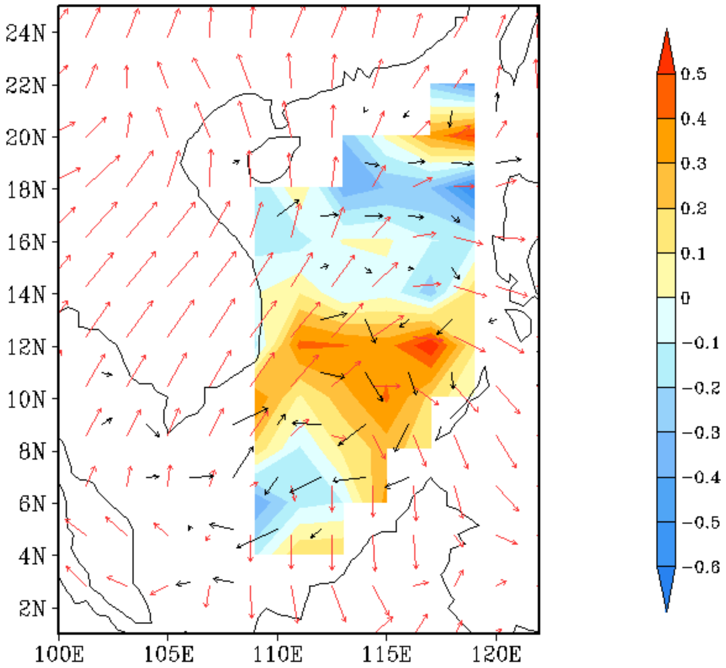

Figure 5. 1 the associated correlation patterns of the PC1 of annual currents with wind (red vectors) and eddy number distribution (shaded); The black vectors show the EOF1 pattern of annual current.

In this chapter, I investigate the extent that the variability in the eddies in the SCS can be predicted by these external large-scale predictors. The barotropic mass stream function from the monthly STORM data is considered to represent the barotropic state and indicate the barotropic instability. Baroclinic instability contains two major components, the current shear and density stratification, which represent the dynamic and thermodynamic components, respectively.

Given that no dominant spatial patterns of the eddy property distributions (see details in section 4.4), I only take the combination of different area-mean eddy properties as predictands to feed the CCA. The vector of the predictands consists of six parameters: the EI of the peak points (I), the ED of the peak points (D), the EN of the peak points (N), the travel distance of the eddy track (L), the eddy lifetime (T) and the percentage of intense eddy points (%I). These six parameters can accurately indicate the states of eddy activity from different perspectives. An intense eddy point is defined as an eddy point with an intensity greater than the 90th percentile of all eddy points.

The analysis presented in Chapter 4 demonstrated that the eddy properties in the SCS have significant seasonal variabilities. Therefore, it is better to separate the properties into different seasons. The intensified eddy points in each summer are counted, and the proportion of those points of all eddy points in each summer is computed as well. Because the units of the parameters are different, all of the parameters are normalized.

In this chapter, I investigate the linkage between the background flows and the eddy parameters during the summer. Sections 5.2 and 5.3 investigate the relationships with the barotropic and baroclinic instabilities, respectively.

5.2 The linkage with barotropic instability

The barotropic mass stream function (BSF) fields correspond to the ocean barotropic states and can reveal barotropic instability. In this section, the monthly BSF fields from the STORM data set are used to derive the relationship between the eddy activity and the barotropic instability in the SCS. The statistical method CCA has been shown to be skillful at analyzing the relationship between two fields, so I choose it as the main method to investigate the linkage between the BSF and the eddy properties and to determine how the eddy properties in the SCS can be affected by the BSF during the summer.

5.2.1 The co-variability of area-mean eddy properties between AEs and CEs

To determine if it is better to take the AEs and CEs together or separately, I investigate the covariability of the eddy vector described above from the AEs and CEs. The intensities of the AEs and CEs are all the absolute values of the SSHA differences between the eddy centers and the outermost contours, so they are all positive. The first 5 EOFs of each vector (the accumulated explained variances are all greater than 98%) are derived as predictands and predictors to feed the CCA. The first pair of CCA patterns (Figure 5.2) of the two vectors in the summer shows that weak, small and less AEs are linked to strong, large and less peak CEs. When there are few intense AEs, there are few intense CEs. In terms of the parameters I and D, AEs and CEs have opposite variabilities; however, for N and %I, they vary in similar ways. Therefore, if I take the two kinds of eddies as a whole, some variability may disappear. For the next analysis, I will treat them separately. An analysis that treats the AEs and CEs as a whole will also be conducted.

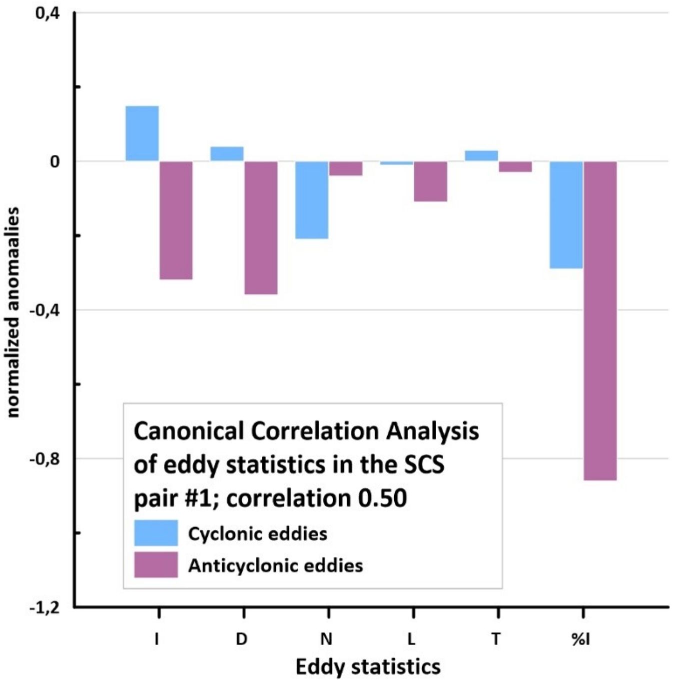

Figure 5. 2 The first pair of CCA patterns based on the AE parameters and CE parameters. (I=EI of the peak points; D=ED of the peak points; N=EN of the peak points; L=travel distance of the eddy track; T= eddy lifetime; %I= percentage of intense eddy points).

5.2.2 The linkage of barotropic mass stream function and eddy properties

Because the linkage is constructed to project the future eddy activity using the large-scale drivers provided by coarse climate models, I interpolate the BSF data onto grids with similar resolutions (i.e., 2 degrees). To avoid small-scale noise, I project the anomalous BSF fields onto its first 10 EOFs and take the reconstructed fields as predictors to feed the CCA. The first 10 EOF modes can explain 90.0% of the total variance of the original anomalies.

Table 5.1 shows the explained variance of each EOF pattern and the corresponding accumulated variance.

In the leading pattern (Figure 5.3), the BSFs on the two sides of 12°N change in opposite ways. An anomalous cyclonic gyre and an anomalous anticyclonic gyre are located to the north and south, respectively. The second EOF pattern also shows opposite variabilities in the northern SCS and southern SCS, but the boundary extends from Vietnam to the Luzon Strait. The intensity of the variability in the southern SCS is much larger than that in the first EOF pattern. The two patterns are associated with the eastward wind jet over the Vietnam coast. In the summer, the southwesterly monsoon is blocked by the mountains in Vietnam, and one branch turns eastward, forming a wind jet. A pair of opposite wind stress curl that is bounded by this jet occurs (Wang et al. 2006; Hein, 2008; Zu et al. 2018). The variability shown in the two EOF patterns may be related to the relative intensity of the opposite wind stress curl.

Table 5. 1 The explain variance and the accumulated variance of the EOFs

	Explained variance	the accumulated expalained variance
EOF1	0.375459	0.375459
EOF2	0.137805	0.513264
EOF3	0.0878622	0.6011262
EOF4	0.0783557	0.6794819
EOF5	0.0694569	0.7489388
EOF6	0.0447055	0.7936443
EOF7	0.0301861	0.8238304

EOF8	0.027891	0.8517214
EOF9	0.0261776	0.877899
EOF10	0.0218905	0.8997895

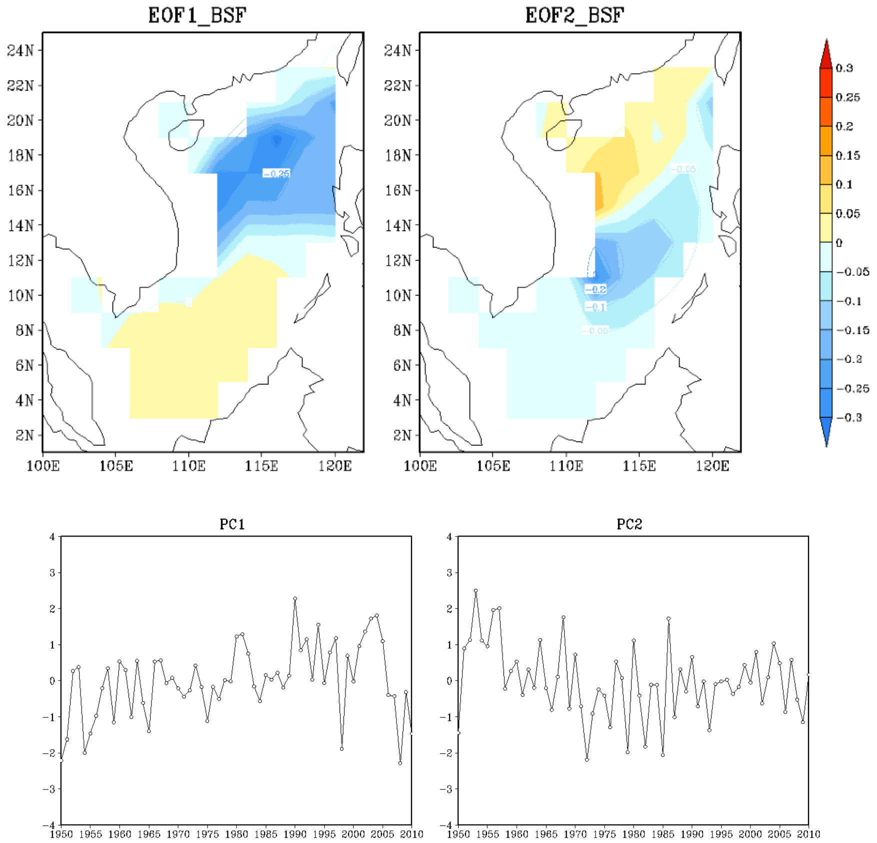

Figure 5. 3 The first two EOFs of barotropic mass stream function (BSF), Unit: 10^{10}kg s-1.

Based on the first 10 EOFs of the anomalous BSF (predictors) and the first 5 EOFs of the normalized parameter vector (predictands), three analyses were performed for the AEs, CEs and their combination.

Figure 5.4 shows the first two pairs of CCA patterns and the corresponding time series of the BSF and AE parameters. The CCA coefficients have correlations of 0.63 and 0.52 for the first two CCA results. In the first CCA patterns, when negative BSF anomalies occur, especially in the Luzon Strait, more AEs with small diameters and short lifetimes appear. The second BSF CCA pattern has a variability with a sandwich structure, with higher variances in the northern SCS. When the BSF in the middle region decreases, more AEs with larger sizes occur, and the proportion of intense eddies increases.

Figure 5.5 shows the CCA result for the CEs. The dominant BSF CCA pattern is similar to the first EOF pattern in Figure 5.3, and the second shows simultaneous and consistent changes for nearly the entire basin. The first two CCA time series of the BSF and CE parameters are highly correlated with correlation coefficients of 0.72 and 0.64, respectively. Interestingly, the first BSF CCA pattern for all eddies (Figure 5.6) exhibits a similar variability to the analysis of the CEs. In addition, when anomalous anticyclonic currents in the northern SCS and anomalous cyclonic currents in the southern SCS form, more eddies with smaller sizes, longer travel distances and longer lifetimes occur in the SCS in both analyses.

The similarity between the two analyses can be attributed to the difference in the numbers of AEs and CEs. In the SCS, many more CEs than AEs are detected in the high-resolution simulation. The variability in the CEs accounts for a greater percentage of the variability in all eddies. The time series of the analysis with all of the eddies shows a high correlation coefficient of 0.71 (Table 5.2) for the first pair of CCA patterns.

To estimate how much of the variability in the eddy parameters can be traced by the BSF, I reconstruct the area-mean eddy parameters according to the CCA results. The results show that the reconstructed eddy parameters can explain approximately 20% of the variance, with 17.4% for the AEs; 21.0% for the CEs and 25.7% for both kinds of eddies (Table 5.2), respectively. Therefore, up to 26% of the eddy variability can be traced by the coarsened BSF.

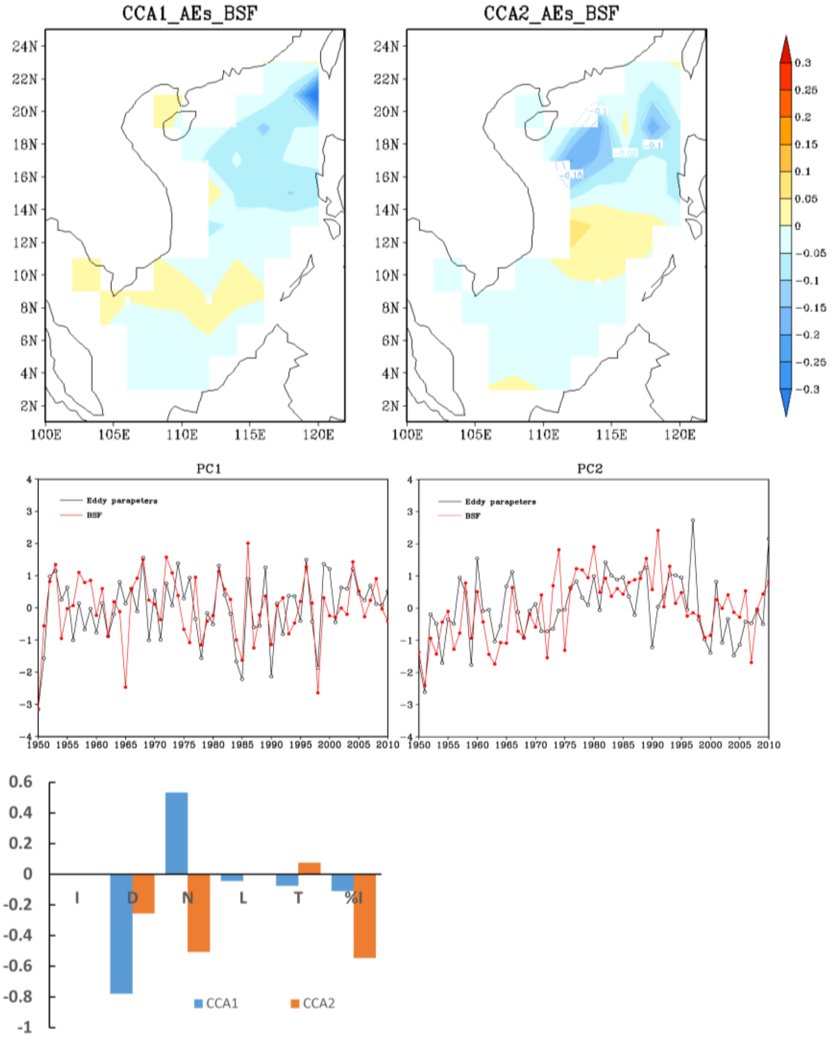

Figure 5. 4 The first two pairs of CCA patterns from the CCA analysis related to the summer BSF and the area-mean AE parameters. The first row shows the first and second CCA patterns of the BSF, and the second row shows the first and second CCA coefficients of the BSF and AE parameters. The bottom row shows the first two CCA patterns of the AE parameters.

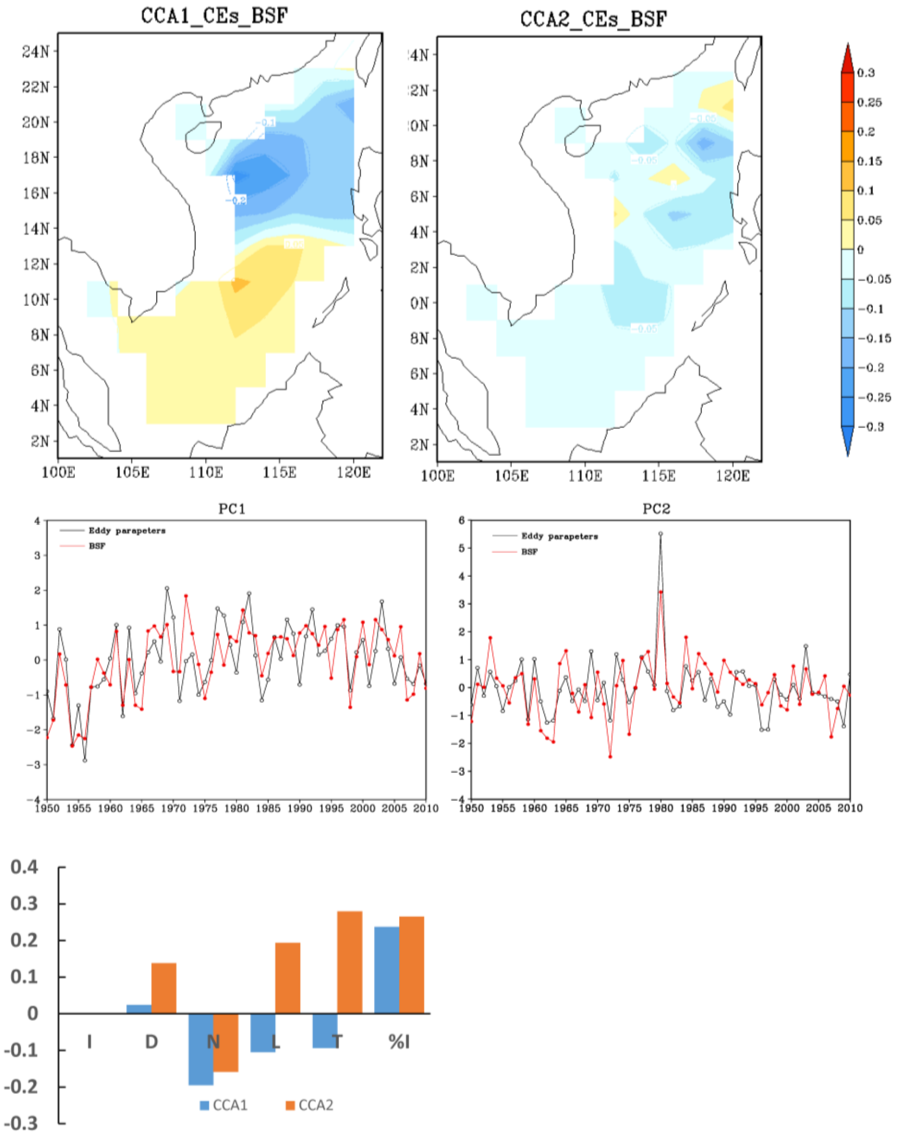

Figure 5. 5 The same with Figure 5.4, but for the analysis with area-mean CE parameters.

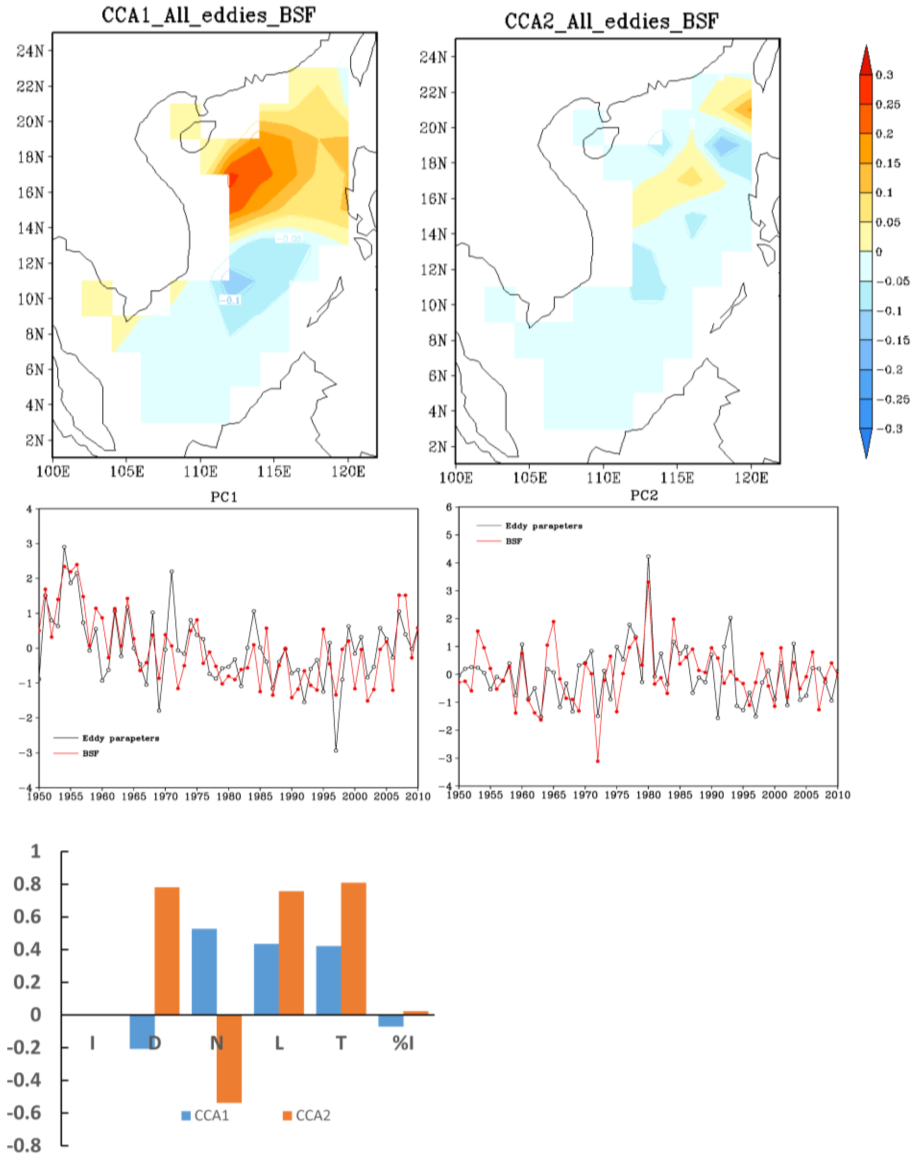

Figure 5. 6 The same with Figure 5.4, but for the analysis with area-mean parameters of both two kind of eddies.

Table 5. 2 The results of the first CCA and the reconstructed variance from the CCA results based on the three analyses. (CCA1_correlation: correlation coefficient of the first CCA; CCA1_Predictands (CCA1_Predictors): variance explained by the first CCA pattern; EX_Var_Reconstructed: total variance explained by the reconstructed predictands).

	CCA1_correlation	CCA1_Predictands	CCA1_Predictors	EX_Var_REconstructed
AEs	0.63	0.34	0.21	17.40%
CEs	0.72	0.43	0.34	21.00%
AEs_CEs	0.71	0.15	0.3	25.70%

5.3 The linkage with baroclinic instability

Baroclinic instability plays an important role in the conversion from potential energy to kinetic energy. The current shear (CS) and potential density gradient are two major components of baroclinic instability, which are related to the dynamic and thermodynamic instability, respectively. STORM has archived monthly ocean velocities and monthly potential density at all 80 layers for the entire period. Here, I use the vertical gradient of the potential density (PDG) to indicate the thermodynamic instability.

In this section, I treat the CS and PDG as predictors to search for their linkage with the eddy parameters. The CCA technique is employed as well. The baroclinic instability caused by the Kuroshio has been shown to be important in the variability in the eddy activity in the northern SCS. The current fields are interpolated onto a coarser grid (2 degrees, which is the same as the grid of the BSF fields).

5.3.1 The linkage of current shear and eddy properties

The difference between the ocean currents at different layers is employed to measure the current shear (CS). I choose 6 typical depths (i.e., the ocean surface, 100 m, 200 m, 500 m, 1000 m and 2000 m) to derive the current shear. Considering the model layer setup and the simulation output, the velocities at 6 m, 100 m, 119 m, 489.5 m, 1008.5 m and 2038.5 m are selected. To determine the two layers in which the CS performs best, I conduct 10 sensitivity tests at depths of 6 m-100 m, 100 m-199 m, 199 m-489.5 m, 6 m-199 m, 100 m-489.5 m, 199 m-1008.5 m, 199 m-2038.5 m, 489.5 m-1008.5 m, 489.5 m-2038.5 m and 1008.5 m-2038.5 m.

Before using the CCA, the first 10 EOFs of the CS are derived; their accumulated explained variances range from 74.1% to 93.5% (Table 5.3). Together with the 3 predictands, there are a total of 30 analyses. I do not show the results of the EOF and CCA patterns and the time series because of the large number of analyses.

For each analysis, to remove small-scale noise, the first 10 EOFs of the predictors and the first 5 EOFs of the predictands are considered in the CCA analysis. Based on the linkages presented by the CCA analysis, I reconstruct the eddy parameter fields using the first five CCA patterns and time series.

The CCA results and the reconstructed results of the 30 analyses are listed in tables 5.4 – 5.6. The correlation coefficients of the first CCA time series between the predictands and the predictors from all of the analyses range from 0.51 to 0.78.

The highest variance explained by the reconstructed predictands (36.4%) occurs in the analysis of the CS at 489.5 m-2038.5 m with the parameters of the CEs. Of all 10 CSs, the CS between 489.5 m and 2038.5 m has a slightly better ability to project the eddy parameters, with the 4th highest reconstructed variance for the AEs, the highest reconstructed variance for the CEs and the 3rd highest reconstructed variance for both types of eddies.

Overall, the current shear in the SCS explains less than 37% of the variability in the area-mean eddy parameters in the summer.

Table 5. 3 The accumulated explained variances of the first 10 EOFs from the 10 CSs

1008.5m-2038.5m	90.1%
100m-199m	75.1%
100m-489.5m	76.7%
199m-1008.5m	80.7%
199m-2038.5m	93.5%
199m-489.5m	74.1%
489.5m-1008.5m	79.6%
489.5m-2038.5m	93.4%
6m-100m	79.9%
6m-199m	78.0%

Table 5. 4 The results of the first CCA and the reconstructed variance from CCA results, according to the ten sets of CSs and the parameters of AEs. (CCA1_correlation: correlation coefficient of the first CCA; CCA1_Predictands (CCA1_Predictors): variance explained by the first CCA pattern; EX_Var_Reconstructed: total variance explained by the reconstructed predictands).

AEs				
	CCA1_correlation	CCA1_Predictands	CCA1_Predictors	EX_V_REconstructed
1008.5m-2038.5m	0.65	0.42	0.1	19.30%
100m-199m	0.7	0.47	0.11	20.80%
100m-489.5m	0.67	0.48	0.13	21.10%

199m-1008.5m	0.52	0.51	0.13	15.60%
199m-2038.5m	0.57	0.46	0.13	16.70%
199m-489.5m	0.55	0.5	0.13	16.60%
489.5m-1008.5m	0.55	0.16	0.12	14.30%
489.5m-2038.5m	0.58	0.35	0.15	16.80%
6m-100m	0.6	0.34	0.11	15.40%
6m-199m	0.6	0.18	0.09	14.60%

Table 5. 5 The same with table 5.4, but for CEs

CEs				
	CCA1_correlation	CCA1_Predictands	CCA1_Predictors	EX_V_REconstructed
1008.5m-2038.5m	0.51	0.57	0.1	16.90%
100m-199m	0.78	0.6	0.13	18.60%
100m-489.5m	0.75	0.56	0.14	16.30%
199m-1008.5m	0.76	0.64	0.15	28.60%
199m-2038.5m	0.75	0.63	0.22	28.00%
199m-489.5m	0.73	0.61	0.13	17.80%

489.5m-1008.5m	0.71	0.68	0.16	31.30%
489.5m-2038.5m	0.71	0.69	0.21	36.40%
6m-100m	0.61	0.63	0.15	20.00%
6m-199m	0.64	0.56	0.2	21.90%

Table 5. 6 The same with table 5.4, but for all eddies.

AEs_CEs				
	CCA1_correlation	CCA1_Predictands	CCA1_Predictors	EX_V_REconstructed
1008.5m-2038.5m	0.56	0.45	0.13	17.80%
100m-199m	0.69	0.15	0.12	16.90%
100m-489.5m	0.7	0.15	0.13	16.10%
199m-1008.5m	0.72	0.23	0.13	28.30%
199m-2038.5m	0.71	0.19	0.21	29.90%
199m-489.5m	0.7	0.17	0.13	18.20%
489.5m-1008.5m	0.72	0.33	0.16	25.00%
489.5m-2038.5m	0.69	0.38	0.21	25.40%
6m-100m	0.67	0.26	0.14	19.30%

6m-199m	0.68	0.11	0.11	17.30%

5.3.2 The linkage of density gradient and eddy properties

This section applies the same analysis method as that in section 5.3.1 for the other component of the baroclinic instability, the vertical gradient of the potential density (PDG). The same ocean layers are used to calculate the difference in the potential density at various depths. Taking the area-mean eddy parameters as predictands, 10 sets of analyses are conducted.

The first 10 EOFs of the PDGs (Table 5.7) are still derived to remove the small-scale noise in the analyses, and the accumulated explained variances range from 94.5% to 99.5%. Tables 5.8 – 5.10 list the CCA results from the 10 sets of analyses. The correlation coefficients of the first CCA time series between the predictands and the predictors from the 30 analyses range from 0.55 to 0.77. No patterns and no time series are presented for the same reason as in section 5.3.1.

Based on the relationship between the eddy parameters and PDGs from the first five CCA modes, I reconstruct the eddy parameters and investigate the extent to which the reconstructed eddy parameters can explain the variability in the predictands (Tables 5.8-5.10), namely, the area-mean eddy parameters. The PDG always has better ability to project the CE activity than the AE activity; more than 30% of the traced variability in the four analyses is related to the CEs, but less than 21% is related to the AEs. Considering the reconstructed eddy parameters and the correlation in the CCA, the PDG between 6 m and 100 m provides the best predictive skill. However, up to 38.6% of the variance in the eddy parameters can be linked to the 2-degree PDG.

Table 5. 7 The accumulated explained variances of the first 10 EOFs from the 10 sets of PDG fields.

1008.5m-2038.5m	99.4%
100m-199m	95.1%
100m-489.5m	95.2%
199m-1008.5m	96.8%
199m-2038.5m	99.5%
199m-489.5m	94.5%
489.5m-1008.5m	96.6%
489.5m-2038.5m	99.5%
6m-100m	96.3%
6m-199m	97.6%

Table 5. 8 The results of the first CCA and the reconstructed variance from the CCA results based on the ten sets of PDGs and the parameters of the AEs. (CCA1_correlation: correlation coefficient of the first CCA; CCA1_Predictands (CCA1_Predictors): variance explained by the first CCA pattern; EX_Var_Reconstructed: total variance explained by the reconstructed predictands).

		AEs		
	CCA_correlation	CCA_Predictands	CCA_Predictors	EX_V_REconstructed
1008.5m-2038.5m	0.55	0.47	0.44	17.00%
100m-199m	0.67	0.47	0.5	17.80%
100m-489.5m	0.76	0.43	0.4	20.60%

199m-1008.5m	0.6	0.22	0.38	16.40%
199m-2038.5m	0.6	0.43	0.42	13.50%
199m-489.5m	0.71	0.23	0.25	15.30%
489.5m-1008.5m	0.59	0.15	0.08	16.90%
489.5m-2038.5m	0.55	0.28	0.21	15.00%
6m-100m	0.77	0.42	0.55	18.40%
6m-199m	0.66	0.38	0.49	18.70%

Table 5. 9 The same with table 5.8, but for CEs

		CEs		
	CCA_correlation	CCA_Predictands	CCA_Predictors	EX_V_REconstructed
1008.5m-2038.5m	0.6	0.68	0.27	24.70%
100m-199m	0.75	0.62	0.55	26.90%
100m-489.5m	0.77	0.64	0.49	30.00%
199m-1008.5m	0.74	0.63	0.14	26.70%

199m-2038.5m	0.75	0.62	0.21	26.20%
199m-489.5m	0.77	0.65	0.14	30.00%
489.5m-1008.5m	0.75	0.7	0.14	38.60%
489.5m-2038.5m	0.65	0.69	0.28	29.90%
6m-100m	0.77	0.65	0.58	32.30%
6m-199m	0.59	0.69	0.22	26.50%

Table 5. 10 The same with table 5.8, but for all eddies

		AEs_CEs		
	CCA_correlation	CCA_Predictands	CCA_Predictors	EX_V_REconstructed
1008.5m-2038.5m	0.61	0.16	0.41	17.50%
100m-199m	0.7	0.21	0.56	19.00%
100m-489.5m	0.76	0.24	0.49	21.40%
199m-1008.5m	0.69	0.19	0.13	21.80%
199m-2038.5m	0.66	0.2	0.2	21.50%

199m-489.5m	0.73	0.24	0.12	23.50%
489.5m-1008.5m	0.68	0.21	0.1	20.70%
489.5m-2038.5m	0.68	0.3	0.31	20.60%
6m-100m	0.71	0.37	0.57	24.10%
6m-199m	0.64	0.4	0.12	25.20%

5.4 Conclusion

In this chapter, I estimate the impacts of the major large-scale factors on the eddy activity in the SCS. The eddy parameter distribution with the 0.1-degree resolution does not have a dominant structure. When the grid is coarsened to 2 degrees, some structure appears; however, the structure may be white noise. Therefore, I use the combination of the area-mean eddy parameters as the predictands to indicate the eddy activity. For the large-scale factors, I select the monthly barotropic stream function (BSF) to represent the ocean barotropic instability and the monthly current shear (CS) and the monthly potential density gradient (PDG) as the dynamic and thermodynamic components, respectively, of the ocean baroclinic instability. The generation and development of oceanic eddies requires sufficient kinetic energy to be converted from the available potential energy, and the ocean instability is the key factor in the conversion.

The canonical correlation analysis (CCA) was used to investigate the links between the ocean instability and the eddy activity. I trace the eddy activity based on the linkages. The results show that up to 40% of the eddy activity variability can be explained by the PDG and CS, and less than 30% of the variability can be explained by the BSF. These three variances cannot be added together. Because of the limited impacts of the large-scale conditions and the absence of a major structure in the eddy property distribution, I hypothesize that the variation in eddy activity is largely controlled by its internal variability and not by the large-scale external forcing. The external drivers have limited impacts on the variability in the eddy activity.

6. Summary and outlooks

This dissertation focuses on the statistics of the travelling eddies in the SCS, the links with large-scale conditions and the potential for empirical downscaling. The activity of oceanic eddies plays important roles in the transport of energy, momentum and mass. The eddies in the SCS have drawn large amounts of attention. However, little research has focused on the long-term statistics of such activities or the projection of future eddy activity. By employing the empirical statistical downscaling model, which is used successfully in meteorology, projections can be made without consuming large amounts of computer time. The statistical downscaling model is constructed by deriving the relationship between the predictors and predictands from past and current observations. The model projects the future state of the predictands by means of coarse predictors from the output of ocean general circulation models (OGCMs). Our work is aimed at investigating the links between the large-scale forcings (predictors) and the travelling eddy activity in the SCS in preparation for the statistical downscaling model.

The main results of our work suggest that the OGCM output is good for studying the statistics of eddies. The distributions of the eddy properties have little spatial organization. The eddy activity reveals significant interannual variability and seasonal differences but little decadal variability, and the variability correlates very weakly with El Niño. Most of the variability is due to internal dynamics, but part of it (on the order of 40%) can be linked to variations in the basin-wide currents.

All studies suffer from insufficient observations with decadal time scales and high resolution. I employ the output of a global eddy-resolved ocean simulation called “STORM”. The STORM simulation used the tripolar version of the MPI-OM ocean model forced by the NCEP1 reanalysis data, and it has a time period of over six decades. It has an average grid space of approximately 10 km and 80 layers in the vertical direction. This setup meets the requirements of our work.

Before using the STORM simulation, I carefully estimate its quality in the SCS by comparing it with the AVISO altimeter observations and the ocean reanalysis data set C-GLORS. AVISO provides only one variable, namely, the sea surface height anomaly (SSHA), but C-GLORS contains numerous variables. Therefore, I first compare STORM with the AVISO and C-GLORS data and find sufficient similarity. I conclude that I may continue the verification of the STORM output by comparing it with the derived C-GLORS data, which include more variables than AVISO.

Overall, STORM shows great similarity with the C-GLORS and AVISO data in representing the SCS dynamics. The seasonal and interannual variabilities in the SSHA described in STORM are similar to those in the AVISO and C-GLORS data. STORM hindcasts the same seasonal and interannual variabilities in the upper circulation with strong western boundary currents and the basin-wide gyre. STORM shows more intensified currents due to its higher resolution. The seasonal change in the sea surface temperature (SST) resolved in STORM is also consistent with the C-GLORS data, and STORM captures a more detailed structure and stronger intensity of the upwelling off the Vietnam coast due to its finer grid.

For further validation, I successfully constructed a statistical downscaling model for the nonseasonal variability in the surface currents in the SCS by means of multiple linear regression and empirical orthogonal function (EOF) analysis. The representation of the dynamic variability and the small-scale phenomena in the SCS by STORM is satisfactory, which demonstrates the suitability of the STORM simulation to derive the eddy activity in the SCS and to construct the empirical statistical downscaling model.

We then take advantage of the STORM simulation to investigate the variability in the travelling eddy activity in the SCS over six decades. To do this, I developed a new eddy detection and tracking algorithm that only relies on the discrete SSHA fields without any differential or integral computations; therefore, it can avoid the inaccuracy caused by such computations. Both the size and shape of the detected eddies are consistent with the SSHA, and the eddy intensity closely matches the SST gradient.

In addition, I conduct a more complete validation of the STORM simulation by comparing it with AVISO data in terms of the distribution of the SCS eddies. AVISO is the most widely used data set for analyzing oceanic eddies. The distributions of the detected potential eddy points from STORM and AVISO are highly similar, with the maximum eddy occurrence frequencies located in the Luzon Strait and along the western boundary. However, the AVISO data show many more eddies than the STORM output. Dufau et al. (2016) pointed out that the mesoscale resolution capability of AVISO is limited. In addition, according to the AVISO handbook (AVISO, 2015), AVISO may contain errors with magnitudes of approximately 1 cm. Therefore, a large number of potential eddy points in the AVISO data may be noise.

After filtering the short-travelled (short-lived) eddies, the distribution patterns from AVISO and STORM are consistent with each other. As expected, the number of eddies remaining in AVISO is greatly reduced. Even fewer eddies are found in the AVISO data than in the STORM results. The underestimation of eddies in AVISO was investigated by Amores et al. (2018), who suggested that this underestimation results from its limited spatial resolution.

A total of 1709 anticyclonic eddy (AE) tracks (28.0 per year) and 3331 cyclonic eddy (CE) tracks (54.6 per year) with travel distances greater than 100 km are detected from the STORM daily SSHA fields during 1950-2010. Their climatological features and the variabilities of the eddy properties at different time scales are investigated. These eddies have a maximum travel distance of 1988 km and lifespans ranging from 6 to 293 days. CEs are much more active than AEs, but AEs with high intensities and large diameters are more common than similar CEs. The multi-year monthly eddy diameter (ED), eddy intensity (EI) and eddy number (EN) have large seasonal differences. Their annual mean ED and EI and the annual accumulated EN exhibit strong interannual variabilities but weak decadal variabilities. These time series have nearly no trends. Furthermore, EI and ED are strongly correlated with each other at seasonal and interannual time scales. The long-term variabilities of the ED, EI and EN are only slightly associated with El Niño. I did not investigate the association in each short time period, during which some correlations may occur, as in Tuo et al. (2018).

Considering the energy source for the eddy activity, the instability of the background flows, which induces the conversion from the available potential energy to kinetic energy, is supposed to play a large role in the variability in the eddy activity in the SCS. I search for the linkages between the eddy activity and the large-scale phenomena by taking the major components of the instability as predictors, including the barotropic instability and the baroclinic instability. The current shear and potential gradient represent the two components of the baroclinic instability, namely, the dynamic instability and thermodynamic instability, respectively.

The EOFs of the annual spatial distributions of the eddy properties (ED, EI and EN) reveal nearly white eigenvalue spectra at the 0.1-degree resolution. Meaningful structures only appear when the distribution is coarsened into a 1-degree or 2-degree grid. Therefore, I do not take the spatial distribution of the predictands but rather use a combination of six area-mean eddy parameters: the EI of the peak points (I), the ED of the peak points (D), the EN of the peak points (N), the travel distance of the eddy track (L), the eddy lifetime (T) and the percentage of intense eddy points (%I). Given the large seasonal differences in the eddy properties, I suggest building linkages between the predictors and the predictands in different seasons. This thesis only conducts an analysis for the summer.

Canonical correlation analysis (CCA) is good for identifying linkages between two fields and for constructing statistical downscaling models. Our work employs CCA to analyze the relationship between the instability of the SCS background flows and the area-mean eddy parameters. The parameters are reconstructed based on the CCA results. To apply the results to the coarse output of a general circulation model (GCM), I interpolate the predictors into a 2-degree grid.

The barotropic mass stream function (BSF) is used to indicate the barotropic instability. It can explain up to 26% of the eddy variability in the summer. I analyzed the impacts of the current shear (CS) and the vertical gradient of the potential density (PDG) between different water depths with 10 sets of analyses. The CS between 489.5 m and 2038.5 m has the best predictive skill in the ten sets, with 36.4% of the CE variability explained by the reconstructed predictands. The PDG between 6 m and 100 m performs a little better than the other nine sets, with traced variances of 20.6% for the AEs and 38.6% for the CEs. Both PDGs for all 10 sets of analyses and the BSF have better predictive skill for the CE activity. The CSs in most of the analyses also exhibit better reconstructed fields for the CEs than for the AEs.

The impact of the large-scale background flows is limited. This result, together with the white noise in the spatial distributions of the eddy properties and the weak correlation with ENSO, indicates the major impact of internal variability (as opposed to variability provoked by large-scale drivers). I suggest that to a large extent, the variability in eddy activity may be controlled by its internal variability. The eddy activity shows substantial stochastic features.

I point out that this work is not sufficiently comprehensive to prove the randomness of the eddy activity. Additional large-scale drivers need to be investigated, such as different large-scale measurements of the instability of the background flows. Our work investigates the influence of the background flows on the eddy activities. This knowledge could contribute to the ecosystem and the energy distribution and conversion in ocean.

In addition, using the STORM simulation, additional research on the long-term statistics of small-scale ocean phenomena could be conducted.

Acknowledgments

I thank the Chinese Scholarship Council (No.201406330048) for funding my four-year studying in Germany at the Helmholtz–Zentrum Geesthacht (HZG). I also very appreciate the finance support from the HZG for my extended studying period.

I would like to express my deepest gratitude to my supervisor Prof. Hans von Storch. He offered me the opportunity to study in the HZG, and has guided me to explore the science. I really appreciate his patience, encouragement and knowledge, which help me to overcome the problems during my PhD work. I'm very grateful to Dr. Delei Li. He gave me great help for programming and scientific writing.

My appreciation goes to my panel chair, Prof. Corinna Schrum. She has helped me with helpful suggestions and the extended finance support. Dr. Katja Woth and Dr. Xing Yi have helped me a lot for getting used to the working environment. I am grateful to Dr. Eduardo Zorita for offering his CCA codes and to Dr. Frauke Feser for improving the abstract in German.

I also thank the German Climate Computing Center (DKRZ) for providing the High Performace Computing systems Mistral and their helpful suggestions. I appreciate AVISO for the altimeter observations, CCMC for the C-GLORS reanalysis data and NGDC for The ETOPO1 data.

My special thanks go to Dr. Jin-song von Storch. She and her group members produced the STORM simulation, which is the foundation of my work. She has helped me a lot with the knowledge of the STORM simulation.

Thanks a lot to my colleagues and friends at HZG. They have enriched my foreign life.

Great thanks to my family and my boyfriend for their moral support.

Reference

Amante, C., 2009: ETOPO1 1 arc-minute global relief model: procedures, data sources and analysis. *http://www. ngdc. noaa. gov/mgg/global/global. html*.

Amores, A., G. Jordà, T. Arsouze, and J. Le Sommer, 2018: Up to What Extent Can We Characterize Ocean Eddies Using Present-Day Gridded Altimetric Products? *J. Geophys. Res. Oceans*, **123,** 7220-7236.

AVISO, 1996: AVISO user handbook: Merged TOPEX/POSEIDON products. AVI-NT-02-101-CN 3.

——, 2015: SSALTO/DUACS user handbook:(M) SLA and (M) ADT near-real time and delayed time products. *Reference: CLS-DOS-NT-06-034***,** 74.

Busuioc, A., R. Tomozeiu, and C. Cacciamani, 2008: Statistical downscaling model based on canonical correlation analysis for winter extreme precipitation events in the Emilia-Romagna region. *International Journal of Climatology: A Journal of the Royal Meteorological Society*, **28,** 449-464.

Chaigneau, A., A. Gizolme, and C. Grados, 2008: Mesoscale eddies off Peru in altimeter records: Identification algorithms and eddy spatio-temporal patterns. *Prog. Oceanogr.*, **79,** 106-119.

Chelton, D. B., M. G. Schlax, and R. M. Samelson, 2011: Global observations of nonlinear mesoscale eddies. *Prog. Oceanogr.*, **91,** 167-216.

Chen, F., and H. von Storch, 2013: Trends and variability of North Pacific polar lows. *Advances in Meteorology*, **2013**.

Chen, G., Y. Hou, and X. Chu, 2011: Mesoscale eddies in the South China Sea: Mean properties, spatiotemporal variability, and impact on thermohaline structure. *J. Geophys. Res. Oceans*, **116**.

Chen, G., J. Gan, Q. Xie, X. Chu, D. Wang, and Y. Hou, 2012: Eddy heat and salt transports in the South China Sea and their seasonal modulations. *J. Geophys. Res. Oceans*, **117**.

Chu, X., C. Dong, and Y. Qi, 2017: The influence of ENSO on an oceanic eddy pair in the South China Sea. *J. Geophys. Res. Oceans*, **122,** 1643-1652.

Chu, X., H. Xue, Y. Qi, G. Chen, Q. Mao, D. Wang, and F. Chai, 2014: An exceptional anticyclonic eddy in the South China Sea in 2010. *J. Geophys. Res. Oceans*, **119,** 881-897.

Dee, D. P., and Coauthors, 2011: The ERA-Interim reanalysis: Configuration and performance of the data assimilation system. *Q. J. Roy. Meteorol. Soc.*, **137,** 553-597.

Dufau, C., M. Orsztynowicz, G. Dibarboure, R. Morrow, and P. Y. Le Traon, 2016: Mesoscale resolution capability of altimetry: Present and future. *J. Geophys. Res. Oceans*, **121,** 4910-4927.

Evadzi, P. I. K., 2017: Regional sea-level at the retreating coast of Ghana under a changing climate, Hamburg University.

Faghmous, J. H., I. Frenger, Y. Yao, R. Warmka, A. Lindell, and V. Kumar, 2015: A daily global mesoscale ocean eddy dataset from satellite altimetry. *Scientific data*, **2**.

Fang, G., H. Chen, Z. Wei, Y. Wang, X. Wang, and C. Li, 2006: Trends and interannual variability of the South China Sea surface winds, surface height, and surface temperature in the recent decade. *J. Geophys. Res. Oceans*, **111**.

Feng, B., H. Liu, P. Lin, and Q. Wang, 2017: Meso-scale eddy in the South China Sea simulated by an eddy-resolving ocean model. *Acta Ocean. Sin.*, **36,** 9-25.

Ferrari, R., and C. Wunsch, 2009: Ocean circulation kinetic energy: Reservoirs, sources, and sinks. *Annual Review of Fluid Mechanics*, **41**.

Geng, W., Q. Xie, G. Chen, T. Zu, and D. Wang, 2016: Numerical study on the eddy–mean flow interaction between a cyclonic eddy and Kuroshio. *J. Oceanogr.*, **72,** 727-745.

Geng, W., Q. Xie, G. Chen, Q. Liu, and D. Wang, 2017: A three-dimensional modeling study on eddy-mean flow interaction between a Gaussian-type anticyclonic eddy and Kuroshio. *J. Oceanogr.***,** 1-15.

Gyalistras, D., H. von Storch, A. Fischlin, and M. Beniston, 1994: Linking GCM-simulated climatic changes to ecosystem models: case studies of statistical downscaling in the Alps. *Climate Research***,** 167-189.

Hallberg, R., 2013: Using a resolution function to regulate parameterizations of oceanic mesoscale eddy effects. *Ocean Modelling*, **72,** 92-103.

He, Q., H. Zhan, S. Cai, Y. He, G. Huang, and W. Zhan, 2018: A New Assessment of Mesoscale Eddies in the South China Sea: Surface Features, Three-Dimensional Structures, and Thermohaline Transports. *J. Geophys. Res. Oceans*, **123,** 4906-4929.

Hein, H., 2008: Vietnam Upwelling-Analysis of the upwelling and related processes in the coastal area off South Vietnam.

Hotelling, H., 1936: Relations between two sets of variates. *Biometrika*, **28,** 321-377.

Itoh, S., and I. Yasuda, 2010: Water mass structure of warm and cold anticyclonic eddies in the western boundary region of the subarctic North Pacific. *J. Phys. Oceanogr.*, **40,** 2624-2642.

Jungclaus, J., and Coauthors, 2006: Ocean circulation and tropical variability in the coupled model ECHAM5/MPI-OM. *J. Clim.*, **19,** 3952-3972.

Kalnay, E., and Coauthors, 1996: The NCEP/NCAR 40-year reanalysis project. *Bull. Am. Meteorol. Soc.*, **77,** 437-471.

Lawley, D., 1956: Tests of significance for the latent roots of covariance and correlation matrices. *Biometrika*, **43,** 128-136.

Lee, T. N., J. A. Yoder, and L. P. Atkinson, 1991: Gulf Stream frontal eddy influence on productivity of the southeast US continental shelf. *J. Geophys. Res. Oceans*, **96,** 22191-22205.

Li, D., H. von Storch, B. Yin, Z. Xu, J. Qi, W. Wei, and D. Guo, 2018: Low-level jets over the Bohai Sea and Yellow Sea: climatology, variability and the relationship with regional atmospheric circulations. *J. Geophys. Res. Atmos.*

Li, J., R. Zhang, and B. Jin, 2011: Eddy characteristics in the northern South China Sea as inferred from Lagrangian drifter data. *Ocean Science*, **7,** 661.

Li, J., Z. Jing, S. Jiang, D. Wang, and T. Yan, 2015: An observed cyclonic eddy associated with boundary current in the northwestern South China Sea. *Aquatic ecosystem health & management*, **18,** 454-461.

Lin, H., J. Hu, Z. Liu, I. M. Belkin, Z. Sun, and J. Zhu, 2017: A peculiar lens-shaped structure observed in the South China Sea. *Scientific Reports*, **7,** 478.

Lorenz, E. N., 1956: Empirical orthogonal functions and statistical weather prediction.

Madec, G., and M. Imbard, 1996: A global ocean mesh to overcome the North Pole singularity. *Clim. Dyn.*, **12,** 381-388.

Madec, G., P. Delecluse, M. Imbard, and C. Levy, 1998: Ocean general circulation model reference manual. *LODYC, Paris*, **91**.

Mahadevan, A., 2014: Ocean science: Eddy effects on biogeochemistry. *Nature*, **506,** 168.

Nan, F., H. Xue, and F. Yu, 2015: Kuroshio intrusion into the South China Sea: A review. *Prog. Oceanogr.*, **137,** 314-333.

Nan, F., H. Xue, P. Xiu, F. Chai, M. Shi, and P. Guo, 2011: Oceanic eddy formation and propagation southwest of Taiwan. *J. Geophys. Res. Oceans*, **116**.

Nencioli, F., C. Dong, T. Dickey, L. Washburn, and J. C. McWilliams, 2010: A vector geometry–based eddy detection algorithm and its application to a high-resolution numerical model product and high-frequency radar surface velocities in the Southern California Bight. *Journal of Atmospheric and Oceanic Technology*, **27,** 564-579.

Pearson, K., 1902: LIII. On lines and planes of closest fit to systems of points in space. *The London, Edinburgh, and Dublin Philosophical Magazine and Journal of Science*, **2,** 559-572.

Pohlmann, T., 1987: A three dimensional circulation model of the South China Sea. *Elsevier oceanography series*, Elsevier, 245-268.

Skourkeas, A., F. Kolyva-Machera, and P. Maheras, 2013: Improved statistical downscaling models based on canonical correlation analysis, for generating temperature scenarios over Greece. *Environmental and ecological statistics*, **20,** 445-465.

Storto, A., and S. Masina, 2014: Validation of the CMCC Global Ocean Eddy-Permitting Reanalysis (C-GLORS). *Centro Euro-Mediterraneo sui Cambiamenti Climatici, Bologna, Italy*.

Storto, A., S. Masina, and A. Navarra, 2016: Evaluation of the CMCC eddy-permitting global ocean physical reanalysis system (C-GLORS, 1982–2012) and its assimilation components. *Q. J. Roy. Meteorol. Soc.*, **142,** 738-758.

Sun, Z., Z. Zhang, W. Zhao, and J. Tian, 2016: Interannual modulation of eddy kinetic energy in the northeastern South China Sea as revealed by an eddy-resolving OGCM. *J. Geophys. Res. Oceans*, **121,** 3190-3201.

Taburet, G., and S.-T. team, 2018: Sea Level TAC-DUACS products.

Tang, S., H. von Storch, X. Chen, and M. Zhang, 2019: "Noise" in climatologically driven ocean models with different grid resolution. *Oceanologia*.

Tim, N., E. Zorita, and B. Hünicke, 2015: Decadal variability and trends of the Benguela upwelling system as simulated in a high-resolution ocean simulation. *Ocean Science*, **11,** 483.

Tuo, P., J.-Y. Yu, and J. Hu, 2018: The changing influences of ENSO and the Pacific Meridional Mode on mesoscale eddies in the South China Sea. *J. Clim.*

von Storch, H., 1992: Inconsistencies at the interface of climate impact studies and global climate research. *Meteorol. Z.***,** 72-80.

von Storch, H., and F. W. Zwiers, 1999: *Statistical analysis in climate research.* Cambridge Univ. Press, 32-36 pp.

von Storch, H. a. G. H., 1984: Comment on "Empirical orthogonal function analysis of wind vectors over the tropical Pacific region." *Bull. Am. Met. Soc.* , **65,** 162.

von Storch, J.-S., H. Haak, E. Hertwig, and I. Fast, 2016: Vertical heat and salt fluxes due to resolved and parameterized meso-scale Eddies. *Ocean Modelling*, **108,** 1-19.

von Storch, J.-S., and Coauthors, 2012: An estimate of the Lorenz energy cycle for the world ocean based on the STORM/NCEP simulation. *J. Phys. Oceanogr.*, **42,** 2185-2205.

Wang, D., H. Xu, J. Lin, and J. Hu, 2008: Anticyclonic eddies in the northeastern South China Sea during winter 2003/2004. *J. Oceanogr.*, **64,** 925-935.

Wang, G., J. Su, and P. C. Chu, 2003: Mesoscale eddies in the South China Sea observed with altimeter data. *Geophys. Res. Lett.*, **30**.

Wang, G., D. Chen, and J. Su, 2006a: Generation and life cycle of the dipole in the South China Sea summer circulation. *J. Geophys. Res. Oceans*, **111**.

Wang, Q., L. Zeng, W. Zhou, Q. Xie, S. Cai, J. Yao, and D. Wang, 2015: Mesoscale eddies cases study at Xisha waters in the South China Sea in 2009/2010. *J. Geophys. Res. Oceans*, **120,** 517-532.

Wang, Y., G. Fang, Z. Wei, F. Qiao, and H. Chen, 2006b: Interannual variation of the South China Sea circulation and its relation to El Niño, as seen from a variable grid global ocean model. *J. Geophys. Res. Oceans*, **111**.

Xiu, P., F. Chai, L. Shi, H. Xue, and Y. Chao, 2010: A census of eddy activities in the South China Sea during 1993–2007. *J. Geophys. Res. Oceans*, **115**.

Yang, Y., X. San Liang, B. Qiu, and S. Chen, 2017: On the decadal variability of the eddy kinetic energy in the Kuroshio Extension. *J. Phys. Oceanogr.*, **47,** 1169-1187.

Yi, X., B. Hünicke, N. Tim, and E. Zorita, 2017: The relationship between Arabian Sea upwelling and Indian Monsoon revisited in a high resolution ocean simulation. *Clim. Dyn.***,** 1-13.

Yuan, D., W. Han, and D. Hu, 2007: Anti-cyclonic eddies northwest of Luzon in summer–fall observed by satellite altimeters. *Geophys. Res. Lett.*, **34**.

Zhan, P., A. C. Subramanian, F. Yao, and I. Hoteit, 2014: Eddies in the Red Sea: A statistical and dynamical study. *J. Geophys. Res. Oceans*, **119,** 3909-3925.

Zhang, M., and H. von Storch, 2017: Toward downscaling oceanic hydrodynamics–suitability of a high-resolution OGCM for describing regional ocean variability in the South China Sea. *Oceanologia*, **59,** 166-176.

Zhang, M., H. von Storch, and D. Li, 2017: The effect of different criteria on tracking eddy in the South China Sea. *Research Activities in Atmospheric and Oceanic Modelling (WGNE Blue Book)***,** 2.25.

Zhang, Z., W. Wang, and B. Qiu, 2014: Oceanic mass transport by mesoscale eddies. *Science*, **345,** 322-324.

Zhang, Z., J. Tian, B. Qiu, W. Zhao, P. Chang, D. Wu, and X. Wan, 2016: Observed 3D structure, generation, and dissipation of oceanic mesoscale eddies in the South China Sea. *Scientific reports*, **6,** 24349.

Zu, T., D. Wang, C. Yan, I. Belkin, W. Zhuang, and J. Chen, 2013: Evolution of an anticyclonic eddy southwest of Taiwan. *Ocean Dyn.*, **63,** 519-531.

Zu, T., H. Xue, D. Wang, B. Geng, L. Zeng, Q. Liu, J. Chen and Y. He, 2018: Interannual variation of the South China Sea circulation during winter: intensified in the southern basin. *Clim. Dyn.***,** 1-17.

Zwiers, F. W., and H. von Storch, 1995: Taking serial correlation into account in tests of the mean. *J. Clim.*, **8,** 336-351.

List of Figures

List of Tables

List of Publications

Zhang, M., and H. von Storch, 2017: Toward downscaling oceanic hydrodynamics–suitability of a high-resolution OGCM for describing regional ocean variability in the South China Sea. *Oceanologia*, **59,** 166-176.

Zhang, M., H. von Storch, and D. Li, 2017: The effect of different criteria on tracking eddy in the South China Sea. *Research Activities in Atmospheric and Oceanic Modelling (WGNE Blue Book)***,** 2.25.

Zhang M. and H. von Storch, 2018: Distribution features of travelling eddies in the South China Sea, *WGNE Blue Book.*

Tang, S., H. von Storch, X. Chen, and M. Zhang, 2019: "Noise" in climatologically driven ocean models with different grid resolution. *Oceanologia*.

Zhang M., H. von Storch, X. Chen, D. Wang and D. Li, Statistics of travelling eddy variability in the South China Sea, 1950-2010. (in preparation)

Abbreviations

AVISO	Archiving, Validation and Interpretation of Satellite Data in Oceanography
BSF	Barotropic Mass Stream Function
CCA	Canonical Correlation Analysis
CS	Current Shear
C-GLORS	CMCC Global Ocean Research System
CMCC	Euro-Mediterranean Center for Climate Change
EOF	Empirical Orthogonal Function
NCAR	National Center for Atmospheric Research
NCEP	National Center for Environmental Prediction
PC	Principal Component
PDG	Potential Density Gradient
SSHA	Sea Surface Height Anomaly
SST	Sea Surface Temperature

Eidesstattliche Versicherung

Declaration on oath

Hiermit versichere ich an Eides statt, dass ich die vorliegende Dissertation mit dem Titel: „The statistics of travelling eddy variability in the South China Sea and its external forcing“ selbstständig verfasst und keine anderen als die angegebenen Hilfsmittel – insbesondere keine im Quellenverzeichnis nicht benannten Internet-Quellen – benutzt habe. Alle Stellen, die wörtlich oder sinngemäß aus Veröffentlichungen entnommen wurden, sind als solche kenntlich gemacht. Ich versichere weiterhin, dass ich die Dissertation oder Teile davon vorher weder im In- noch im Ausland in einem anderen Prüfungsverfahren eingereicht habe und die eingereichte schriftliche Fassung der auf dem elektronischen Speichermedium entspricht

Hamburg, den *city and date*

Unterschrift *signature*